Characterization of High-Temperature Ceramics for Nuclear Fuels Applications

A Dissertation Presented for the

Doctor of Philosophy

Degree

The University of Tennessee, Knoxville

Jacob A. Minnette

December 2025

DEDICATION

This project is in dedication to my mentor and earliest inspiration, Carolyn Sue McGregor-Peachee.

ACKNOWLEDGEMENTS

The research presented in this dissertation was performed in collaboration with Christina Trautmann, Ina Schubert, Igor Ivanov, Matthew Kurley, David Sprouster, Daniel Olds, Changyong Park, Joerg Neuefeind, Andrew Nelson, Xiaofeng Guo, Elizabeth Sooby, William Cureton, and Eric O'Quinn. I would like to thank my advisor and key contributor to the included projects, Maik Lang, without which these projects could not have been facilitated. To my committee members, Maik Lang, Steve Zinkle, Andy Nelson, and Xiaofeng Guo, I wish to express gratitude for additional research guidance and support. This project was supported by numerous colleagues including, Igor Gussev, Alexandre Solomon, John Hirtz, Cale Overstreet, Zach Chaney, Evan Williams, Julian Valdez, William Vance, William Reed, Kenneth Sanders, Eric Kadel, Jeffrey Brockway, William Gardner, Katherine Parker-Repsher, and Jackson Cagle. To my mother, Ronda, and sisters Nichole, Hannah, Rebekah, and Leah, I express absolute gratitude, I would have never made it to this position without your support. I would be remiss to not thank my loyal companion, my dog Sylvie, who has supported me throughout my graduate school adventures. Thank you to all who have stood by me in my journey and to those I have yet to meet.

This research was primarily funded by the Chicago DOE Alliance Center (CDAC) in cooperative agreement with the U.S. Department of Energy, National Nuclear Security Administration (Award number: DE-NA0004153). Additional funding and support was provided by the Department of Energy Office of Nuclear Energy's Nuclear Energy University Program under US-DOE contract DE-NE0008895. Much of the work conducted in these studies was performed at DOE National Laboratory user facilities including the High Pressure Collaborative Access Team at Argonne National Laboratory, Nanoscale Ordered Materials Diffractometer at Oak Ridge National Laboratory, and the Pair Distribution Function/X-ray Powder Diffractometry

Section at Brookhaven National Laboratory. Additional work was conducted in collaboration with the Nuclear Fuel Development Section at Oak Ridge National Laboratory. Irradiation work, conducted for these studies, was performed at GSI Helmholtzzentrum für Schwerionenforschung FAIR phase 0 in Darmstadt Germany and DC-60 Heavy Ion Cyclotron located at the Interdisciplinary Scientific Research Complex in Astana Kazakhstan.

ABSTRACT

Ultra-high-temperature ceramic compounds (UHTCs) are a broad class of ceramics that include transition and actinide metal carbides, nitrides, and borides. The physical properties of these materials, such as their elevated melting temperature and enhanced thermal conductivity, enable remarkable resilience against modification in extreme environments. As such, these materials are being implemented in advanced aerospace and energy technologies where they will be exposed to these extremes during operating conditions. Specifically, within the nuclear energy sector, UHTCs such as uranium carbides and nitrides will be used in environments consisting of extreme mixed radiation fields (*e.g.*, fission fragments & neutrons), elevated temperatures (T > 2000K), corrosive conditions, and evolving chemical composition. This work describes the synthesis of both transition (*e.g.*, ZrC) and actinide metal carbides/nitrides (*e.g.*, UC/UN) and the accumulation of structural and chemical modifications under far-from-equilibrium conditions.

Proposed within this research project is the use of advanced experimental characterization approaches including high-resolution synchrotron X-ray diffraction, spallation neutron total scattering, and Raman spectroscopy. Utilizing leading edge Sol-Gel synthesis approaches enabled detailed assessment of structural and chemical characteristics with low impurity contamination, enabling thorough investigations into ion beam induced sample modifications. Despite their structural similarities, the performance of all UHTCs studied under energetic heavy ion irradiation differs greatly. For instance, the unit cell expansion of ZrC follows an unexpected, two-stage profile up to the maximum fluence studied 5×10^{13} cm^{-2}. In contrast, UC and UN behave in a different manner when studied under identical irradiation conditions. UC follows a standard one-stage swelling trend with clear saturation $dA/A_{0,sat}$ = 15.2 ± 0.1 %, whereas UN does not demonstrate any indication of swelling saturation to the maximum fluence studied 8×10^{13} cm^{-2}.

This result carries significant impact in nuclear fuel-form materials research and demonstrates the effect of the inherently complex nature of transition metal and actinide carbides under extreme conditions. Detailed structural studies of the UC and UN samples under both ambient and far-from equilibrium conditions elucidate how the SHI induced defects may lead to defect accumulation/clustering, phase segregation, and chemical modifications (*e.g.*, oxidation).

TABLE OF CONTENTS

CHAPTER 1: INTRODUCTION…… 1

1.1 Overview…….. 1

1.2 Characteristics of Transition Metal Carbides……...3

1.3 Uranium Carbide and Nitride Chemical and Structural Characteristics……..8

1.4 Nuclear Fuel Materials Under Extreme Conditions……... 11

CHAPTER 2: METHODS AND APPROACH…… 15

2.1 Sample Preparation……... 16

2.1.1. Production of transition metal carbides and uranium carbonitrides through internal gelation techniques…… 16

2.1.2. Sample preparation for ion beam irradiations……21

2.2 Irradiation with Swift Heavy Ions……23

2.3 Advanced Characterization Methods……...25

2.3.1 Synchrotron X-ray Scattering Experiments…….....25

2.3.2. Neutron Total Scattering Experiments…… 31

2.3.3. Raman Spectroscopy…… 32

2.3.4. Scanning Electron Microscopy & Energy Dispersive Spectroscopy…….33

2.3.5. Data Analysis from X-ray and Neutron Scattering Experiments……. 33

2.3.6. Thermogravimetric Analysis and Differential Scanning Calorimetry……. 36

CHAPTER 3: MULTI-SCALE CHARACTERIZATION OF URANIUM CARBIDE AND NITRIDE…….. 37

3.1 ABSTRACT……38

3.2 INTRODUCTION……39

3.3 RESULTS……41

3.3.1 Scanning electron microscopy……41

3.3.2 Diffraction pattern analysis……44

3.3.3 Pair distribution function analysis……50

3.4.3 Thermogravimetric analysis and differential scanning calorimetry……55

3.5 DISCUSSION……59

3.6 CONCLUSIONS……66

CHAPTER 4: RADIATION RESPONSE OF TRANSITION METAL CARBIDES TO SHI IRRADIATION……67

4.1 ABSTRACT……68

4.2 INTRODUCTION……69

4.3 RESULTS……74

4.3.1 Microcrystalline samples……74

4.3.2 Nanocrystalline samples……80

4.3.3 Results across different material compositions and beam conditions……83

4.4 DISCUSSION……85

4.5 CONCLUSIONS……90

CHAPTER 5: RESPONSE OF URANIUM CARBONITRIDES AND OXIDE TO HIGHLY IONIZING RADIATION……92

5.1 ABSTRACT……93

5.2 INTRODUCTION……94

5.3 RESULTS……97

5.3.1 Scanning electron microscopy and energy dispersion spectroscopy……..97

5.3.2 XRD and Rietveld analysis……...100

5.3.3 Raman spectroscopy……110

5.5 DISCUSSION……...112

5.6 CONCLUSIONS……..115

CHAPTER 6: CONCLUSIONS……...117

BIBLIOGRAPHY……..119

VITA……140

LIST OF TABLES

Table 1. Summary of ZrC and CeO2 sample types used within this irradiation study. 18

Table 2. Summary of input synthesis parameters for uranium bearing samples as utilized within projects 1 & 3. 20

Table 3. UC Rietveld data, results given for both XRD and neutron diffraction with related errors. * Indicates that these results were selected from bank 5, optimized for highest resolution at high scattering angles. 47

Table 4. UN Rietveld data, results given for both XRD and neutron diffraction with related errors. * Indicates that these results were selected from bank 5, optimized for highest resolution at high scattering angles. 48

Table 5. Tabulated neutron PDF results for uranium carbide and uranium nitride, fitted window from 1 to 10 Å (R-space). 52

Table 6: Oxidation energetics for relevant uranium carbide and uranium nitride crystallographic phases 63

Table 7. Tabulated results for comparison of different SHI irradiations of TMCs from this study and Williams, et al. [42]. 84

LIST OF FIGURES

Figure 1. Schematic of TRISO particle for (A) pellet compact (from [1]), and (B) pebble compact (from [2]). 2

Figure 2. Simplified phase diagram of ZrC as a function of carbon content and temperature (reproduced figure from [10]). 5

Figure 3. Schematic of vacancy ordering in zirconium carbide (Zr_8C_7 phase). Red circle highlights the vacant carbon lattice site. 7

Figure 4. (A) Uranium carbide phase diagram, re-constructed from results compiled within [18]. With the X-axis defined as the stoichiometric ratio of carbon to uranium atoms and the Y-axis being the quench temperature. Red zone indicates the targeted synthesis region for this study. (B) and (C) depict schematics of the primary expected phases from synthesis, UC and UC_2. 9

Figure 5. (A) Uranium nitride phase diagram, re-constructed from results compiled within [19], [20]. With the X-axis defined as the stoichiometric ratio of nitrogen to uranium atoms and the Y-axis being the quench temperature. Red zone indicates the targeted synthesis region for this study. (B) and (C) depict schematics of the primary expected phases from synthesis, UC and U_2N3. .. 10

Figure 6. (A) schematic of ion track formed from SHI. (B), (C), (D) demonstration of ion track overlap corresponding to linear, sub-linear, and saturation stages of direct-impact model, eqn. 2. Not drawn to scale. 14

Figure 7. Agate mortar and pestle used for sample grinding alongside sample sieve. 22

Figure 8. SRIM calculated ion energy loss as a function of depth into (A) ZrC and (B) UC for Xe 198 MeV ions. Mean stopping power shown with red dashed lines [41]. 24

Figure 9. Effective sensitivities for relevant elemental species for UC_xN_{1-x} system for X-rays, and neutron elastic scattering..... 26

Figure 10. Schematic of transmission mode μXRD at HPCAT (not drawn to scale). Similar beam and detector geometry at NSLSii. 28

Figure 11. Simplified schematic of loaded fuel kernels within Kapton for X-ray diffraction measurements. 29

Figure 12. Custom manufactured double-encapsulation sample holder. (A) picture of master test assembly, 1×6 array for aluminum frames affixed with BKL-4 compatible mount. Outer Kapton layer glued onto frame with PLA bracket bolted overtop. (B) Schematic of individual aluminum from with Kapton window affixed with PLA bumper (mirrored on reverse side). 30

Figure 13. Simplified schematic of a representative total scattering data output. Sharp peaks labeled in green correspond to Bragg peaks (contributions from the long-range or average structure). Diffuse scattering is represented by peak widening at the bottom ~20 % of the Bragg peak and contains information relevant to the local (atomic) structure, shown labeled in red..... 35

Figure 14. (A) Uranium carbide spheroids shown at 65x magnification with selected spheroids shown at enhanced magnification in (B) & (C). 42

Figure 15. (A) Uranium nitride spheroids shown at 30x magnification with selected spheroid shown at enhanced magnification in (C). (B) Demonstrates inhomogeneities within sphere size and shape. 43

Figure 16. As shown black curve indicating fitted uranium carbide, blue curve fitted uranium nitride, grey markers indicated measurement data, red curve indicates difference curve between fitted and observed data. Selected (hkl) indices provided for primary phase, red asterisks indicate minority phase(s). (A) uranium carbide & (C) uranium nitride XRD results from NSLSii measurements, inset shown to highlight high Q range for UN XRD. (B) uranium carbide & (D) uranium nitride neutron diffraction results from SNS measurements. 45

Figure 17. As shown black curve (A) indicating fitted uranium carbide, blue curve (B) fitted uranium nitride, grey markers indicated measurement data, red curve indicates difference curve between fitted and observed data for neutron PDF results from SNS measurements. Yellow box indicates unfitted C-C dimer (correlated distance of 1.2 Å). 51

Figure 18. Box-car refinement results for uranium nitride rock-salt phase showing unit cell parameter (left axis) and fit quality (right axis) with respect to sliding real-space R value. 54

Figure 19. TGA (black curve) and DSC (red curve) thermodynamic results for the uranium carbide sample. Corresponding Y-axes have matching color schemes. 57

Figure 20. TGA (black curve) and DSC (red curve) thermodynamic results for the uranium nitride sample. Corresponding Y-axes have matching color schemes. 58

Figure 21. Unit cell correlation plot reproduced from [65], [66], [75], [83], [91], [92], [93], [94], [95], [96], with results of unit cell parameter and fraction of nitrogen lattice sites occupied by N-atoms of the rock-salt uranium nitride. Correlated quadratic with results of unit cell parameter and fraction of nitrogen lattice sites occupied by N-atoms of the rock-salt uranium nitride. Correlated quadratic expression (red dashed line) shown on figure. A linear regression in accordance with Vegard's law is shown (grey dashed line). 64

Figure 22. (a) Fluorite UO_2 and (b) rocksalt UC atomic arrangements. Uranium atoms are displayed as green spheres in both figures, oxygen as red, and carbon as black. Respectively isostructural to the two materials used in this study: (a) CeO_2 and (b) ZrC. 71

Figure 23. (a) Stacked synchrotron XRD patterns of microcrystalline PVD1 ZrC (400–1200 nm grain size) with normalized intensity, pristine and irradiated with 946 MeV Au ions of increasing fluence (given in ions cm−2). (b) enlarged view of (111) diffraction peak, to display peak shift (dashed black vertical line) and broadening (red horizontal arrows). 75

Figure 24. Unit-cell expansion determined by Rietveld refinement of XRD patterns as a function of ion fluence for microcrystalline ZrC and CeO2. (a) Different ZrC samples were irradiated during two beamtimes under the same conditions with 946 MeV Au ions (blue PVPVD1, magenta SG1, black SG2; see table for sample labeling). The inset highlights unit-cell expansion in the direct-impact regime (fluences up to ~1.0×10^{13} ions cm^{-2}). (b) CeO_2 unit-cell expansion compared with ZrC from (a). The error bars represent uncertainties from Rietveld refinements. The dashed lines suggest trends to guide the eye). 77

Figure 25. Microstrain accumulation for (a) microcrystalline ZrC, red line is a suggested guide to the eye, and (b) microcrystalline CeO2 both synthesized via the PVD method as a function of increasing ion fluence, the blue line shows Poisson fit of direct impact trend, as determined by Williamson-Hall plots. (c) Coherent domain size as determined with Williamson-Hall analysis for PVD1 ZrC. Error bars represent uncertainties from Williamson-Hall analysis..... 79

Figure 26. Stacked XRD patterns of nanocrystalline ZrC (20 nm grain size, PVD2) before and after irradiation with 946 MeV Au ions of increasing fluence (given in ions cm−2), with normalized intensity. The vertical dashed lines indicate ZrO2 (tetragonal) peak locations. 81

Figure 27. Evolution of a unit-cell parameter in nanocrystalline ZrC as a function of ion fluence, determined by Rietveld refinement of XRD patterns. The red dashed line, produced from linear regression of average value of unit-cell parameter, serves to guide the eye. The error bars represent uncertainties from Rietveld refinements. The red star indicates unirradiated sample with a unit-cell parameter value of 4.68 ± 0.01 Å. 82

Figure 28. SEM of pristine UC (A), and irradiated ($\Phi = 6 \times 10^{13}$ cm^{-2}) collected at 750 times magnification (scale bar depicted on images). Corresponding EDS is shown for uranium, carbon,

and oxygen. Figures B, C, & D (respectively) for pristine (A) and F, G, & H (respectively) for irradiated (E). 98

Figure 29. SEM of pristine UN (A), and irradiated ($\Phi = 4 \times 10^{13}$ cm^{-2}) collected at 750 times magnification (scale bar depicted on images). Corresponding EDS is shown for uranium, carbon, and oxygen. Figures (B), (C), & (D) for pristine (A) and (F), (G), & (H) for irradiated..... 99

Figure 30. XRD diffraction plots: (A) UC, (C) UN, (E) UO_2. Plots (B), (D), and (F) depict a zoomed version of (111) reflection for highlighted fluence points, corresponding to UC, UN, and UO_2, respectively. Dashed lines indicate reflections for the following phases: rock-salt (shown in grey), UC_2 (shown in green), U_2N_3 (shown in purple) and UO_2 (shown in red). 101

Figure 31. Relative unit cell swelling with respect to ion fluence of the UC (monocarbide, rock-salt) phase shown in black, with reference UO_2 swelling shown in red. Error bars indicate sample and refinement errors. Poisson trendline shown in respective colors. 103

Figure 32. (A) Primary (UC), and (B) secondary phases (UC_2 & UO_2) in uranium carbide irradiated samples. Presented in black, red, and blue respectively. Error bars indicate sample and refinement errors. 105

Figure 33. Relative unit cell swelling with respect to ion fluence of the UN (mononitride, rock-salt) phase. Error bars represent uncertainties from refinement. 106

Figure 34. Refined phase fractions within UN sample, black represents the dominant mononitride phase, red is fluorite UO_2, and blue is U_2N_3. Representative error bars are shown. 108

Figure 35. Microstrain with respect to fluence: A) UC (monocarbide, rock-salt phase), and B) UN (mononitride, rock-salt phase) samples. Error bars indicate sample and data analysis error. 109

Figure 36. Collected Raman spectra for, (A) UC, (B) UN, and (C) UO_2 samples. Black dashed lines indicate Raman active modes associated with carbon; red dashed lines indicate Raman active modes associated with UO_2. 111

CHAPTER 1: INTRODUCTION

Portions of this chapter were previously published in the Journal of Applied Physics by Jacob A. Minnette, Evan Williams, William F. Cureton, Alexandre Solomon, Eric O'Quinn, Matthew Kurley, Rodney D. Hunt, Changyong Park, Ina Schubert, Christina Trautmann, and Maik Lang. For these works, J.A.M., E.W., W.F.C., M.K., R.D.H., and M.L. conceived experiments; J.A.M., E.W., W.F.C., A.S., E.O., C.P., I.S., C.T. and M.L. prepared relevant samples and performed formal analysis; J.A.M. drafted the manuscript with input from all co-authors.

The content of this chapter serves as a broad overview of literature from existing research for this project. Materials relevant for TRISO particles, are detailed as well as synthesis pathways, relevant extreme environments and previous work studying these materials following such extremes.

1.1 Overview

This project serves to investigate the structural and chemical characteristics of nuclear fuel materials. Specifically, investigations were conducted with candidate materials for TRI-structural ISOtropic (TRISO) fuel, schematic shown in figure 1. Characterization efforts include X-ray and neutron total scattering, electron microscopy, thermogravimetric analysis and differential scanning calorimetry, and Raman spectroscopy. Evaluations of material homogeneity, both structural and chemical, as well as the evolution of defects formed from synthesis and from exposure to extremes are all considered as a part of these efforts. Literature is leveraged to produce a more detailed insight into defect pathways and to draw comparisons of the effects of SHIs relative to other forms of radiation, thereby addressing critical knowledge gaps.

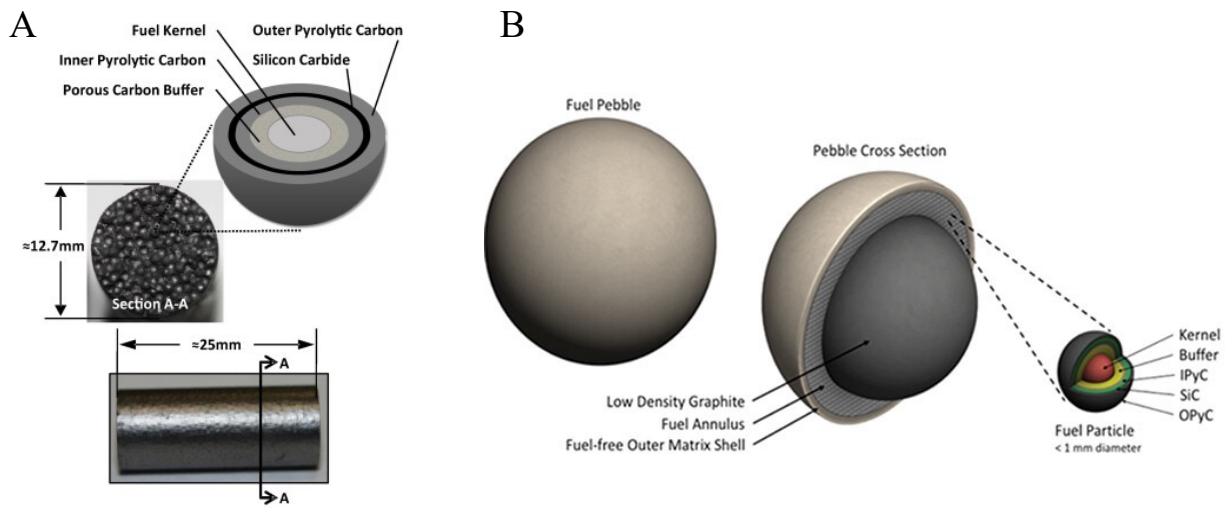

Figure 1. Schematic of TRISO particle for (A) pellet compact (from [1]), and (B) pebble compact (from [2]).

Present-day commercial nuclear reactors almost universally utilize uranium dioxide (UO_2) sintered cylindrical pellets to produce energy [3]. After more than 70 years of power generation, the nuclear energy industry has grown to demand increasingly more and more from reactor fuels. Examples of this increased demand include the ever-present push for increasing fuel "burn-up" – a metric of the percentage of uranium expended to fission – as well as increasing fuel center-line temperatures as close as possible to the melting temperature of UO_2 [3], [4]. Proposed generation IV nuclear reactors will demand even more from their fuel all while enhancing the safety in operating the power plant. This leads to the requirement of new, more robust, fuel-form materials such as ultra-high temperature ceramics (UHTCs) [4].

UHTCs consist of transition and actinide metal carbides, nitrides, and borides that exhibit excellent mechanical and thermodynamic properties at elevated temperatures. High material strength, thermal conductivity, and resistance to chemical corrosion extremes are all attributes expressed in UHTCs [5]. Such characteristics are highly desirable in a nuclear fuel environment where fuel temperatures in proposed high-temperature gas-cooled reactors (HGTRs) reach as high as 2000 K [4], [6]. For the purposes of this study we restrict our evaluation to transition metal carbides (*e.g.*, ZrC) and actinide metal carbides and nitrides (*e.g.*, UC_xN_{1-x}) both are proposed for use in TRISO [1].

1.2 Characteristics of Transition Metal Carbides

Transition metal carbides (TMCs) consist of metal elements in groups 3-12 of the periodic table that are covalently bound to carbon atoms. Typically, this arrangement consists of the carbon atom occupying an interstitial position within the metal sublattice without producing considerable structural distortions, *e.g.*, dumbbell pairs. For this reason, these materials are sometimes referred to as "interstitial compounds" [7], [8]. The incorporation of carbon does impact the structure of

the compound, *e.g.*, zirconium, a hexagonally close packed material that transitions to face-centered cubic with sufficient carbon. Likewise, the incorporation of carbon as an interstitial alters the physical properties of the materials including increasing fracture toughness, and thermal conductivity [9].

There exists many open questions pertaining to the performance of TMCs in a nuclear reactor environment that remain unanswered. Specifically, detailed structural assessment into the impact of chemical stoichiometry, defect accumulation, and potential oxygen exposure all of which evolve during reactor operation is critically lacking. TMCs are typically berthollide compounds, meaning they maintain a single crystallographic phase across a wide range of stoichiometries (*e.g.*, 1 metal atom: 1 non-metal atom) [7]. In TMCs this typically manifests as a deficit of carbon. In ZrC (as with other TMCs) this results in a complex phase diagram, figure 2, as a function of both temperature and carbon content for ZrC [27].

The impact of chemical stoichiometry on all binary metal carbide and nitride samples is a major area of intrigue for structural assessment. TMCs can retain their coherent structure with a wide range of stoichiometries. This variance in stoichiometry while remaining phase pure is known as the homogeneity interval [7]. Work first conducted by Hagg, conveyed how carbon, and other similar low-Z elements, can be incorporated into metallic structures without significant structural modifications [7]. Further studies refute this claim as many body-centered cubic (bcc) structured metals take on a face-centered cubic (fcc) when bonded to carbon or nitrogen [7], [8]. A simple empirical rule, equation 1, set by Hagg exists that allows for TMCs to form nonstoichiometric compounds [8].

$$0.41 < \frac{R_X}{R_M} < 0.59 \quad (1)$$

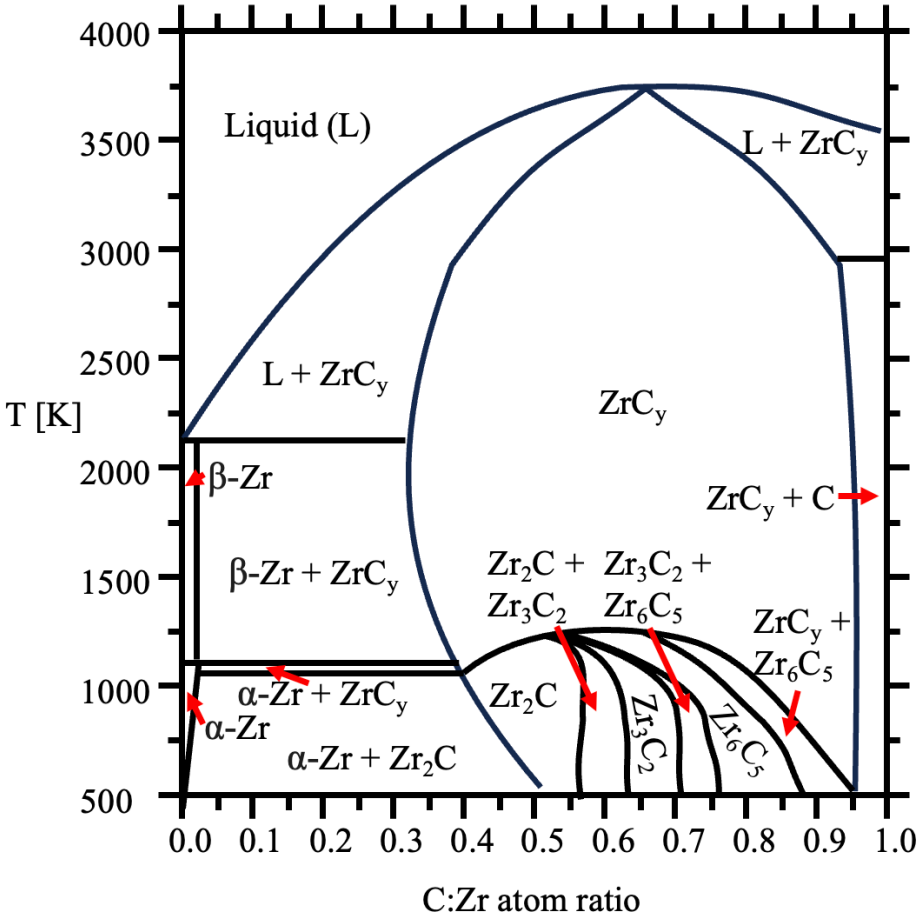

Figure 2. Simplified phase diagram of ZrC as a function of carbon content and temperature (reproduced figure from *[10]*).

Here, R_X is the atomic radii of the non-metal atom (*e.g.*, carbon $R_X = 0.0772$ nm), R_M is the atomic radii of the metal atom (*e.g.*, zirconium $R_M = 0.1597$) [11]. Within the defined interval we find the known non-stoichiometric compounds. The geometric voids left in the metallic sublattice can then be filled with small nonmetallic atoms (carbon) which then add strain to the lattice system modifying crystallographic symmetry and contributing to swelling. Vacancies are required to produce the necessary structural relaxations [7]. Variability in the concentration and ordering of these vacancies has only been studied in limited cases, mostly with transmission electron microscopy (TEM) [12], [13], [14]. Vacant and occupied non-metal sublattice sites can readily be substituted which results in the potential for metastable disordering [7]. The occupancy of the non-metal sites impacts lattice geometry. Vacancies can form ordered superstructures, example depicted in *figure 3*, but variable non-metal atom species can also lead to strain, symmetry reductions, and swelling/contraction. Within the ZrC_xN_{1-x} system, we can see this in full effect, as 'x' is decreased the corresponding unit cell parameter is also reduced [15].

Synthesis pathways can be used to tailor specifically desired phases or stoichiometries dependent on the use case requirements and the quantities of material needed. These techniques include chemical vapor deposition (CVD), magnetron sputtering, arc heat melting, and carbothermic reduction (CTR). Detailed information on the material production/sourcing can be found in *Chapter 2*. For purposes of leveraging TMCs as a surrogate material, *i.e.*, nonradioactive isostructural equivalent to uranium carbide, we utilized CTR. This technique most similarly follows industrial standards for TRISO kernel production [16]. CTR has the added benefit of being able to carefully adjust precursor reagent material ratios to select specific stoichiometric ratios, Zr:C [16]. Differing synthesis recipes also contribute to variance in final material composition

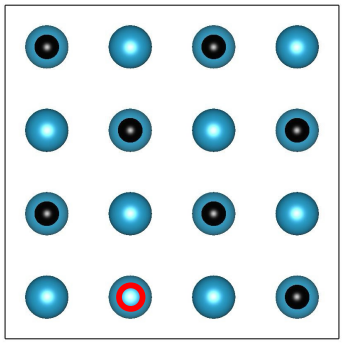

Figure 3. Schematic of vacancy ordering in zirconium carbide (Zr_8C_7 phase). Red circle highlights the vacant carbon lattice site.

(stoichiometry, chemical impurities), and initial defects (vacancy fraction). These factors must be considered when evaluating radiation response mechanisms.

1.3 Uranium Carbide and Nitride Chemical and Structural Characteristics

Uranium carbonitride, UC_xN_{1-x}, materials behave in a similar manner as TMCs, but still possess a few critical distinctions. The first being the polyvalency of uranium, with oxidation states of +3, +4, +5, and +6, all being readily accessible [17]. Additionally, with the particularly large octahedral FCC sites (V ~1.5-1.6 Å), such as in the uranium carbide system, enable multiple non-metal atoms to be accommodated [7]. The phase diagrams depict the high levels of sensitivity of the UC and UN to both stoichiometry and temperature [18], [19], [20].

As can be seen from the phase diagrams, both the UC and UN systems possess a rather narrow homogeneity interval. With both systems readily forming hyperstoichiometric impurity phases that precipitate out from solution. Despite this, the FCC UC and UN phases may still be stabilized as hypostoichiometric. Oxygen solubility is yet another critical variable to track as dissolved and trapped oxygen can readily react with UC_xN_{1-x} materials. This means that within the UC phase system one may expect uranium atoms to be bond to carbon, oxygen, or a vacancy (V) within the octahedral FCC site. UN is similar, with notably high solubility for carbon in octahedral sites allowing for C, N, O, and V atom species all to be present [21], [22], [23], [24]. The composition of the non-uranium components plays a significant factor on the structural characteristics of the material, most obviously demonstrated through dilations/contractions of the unit cell parameter.

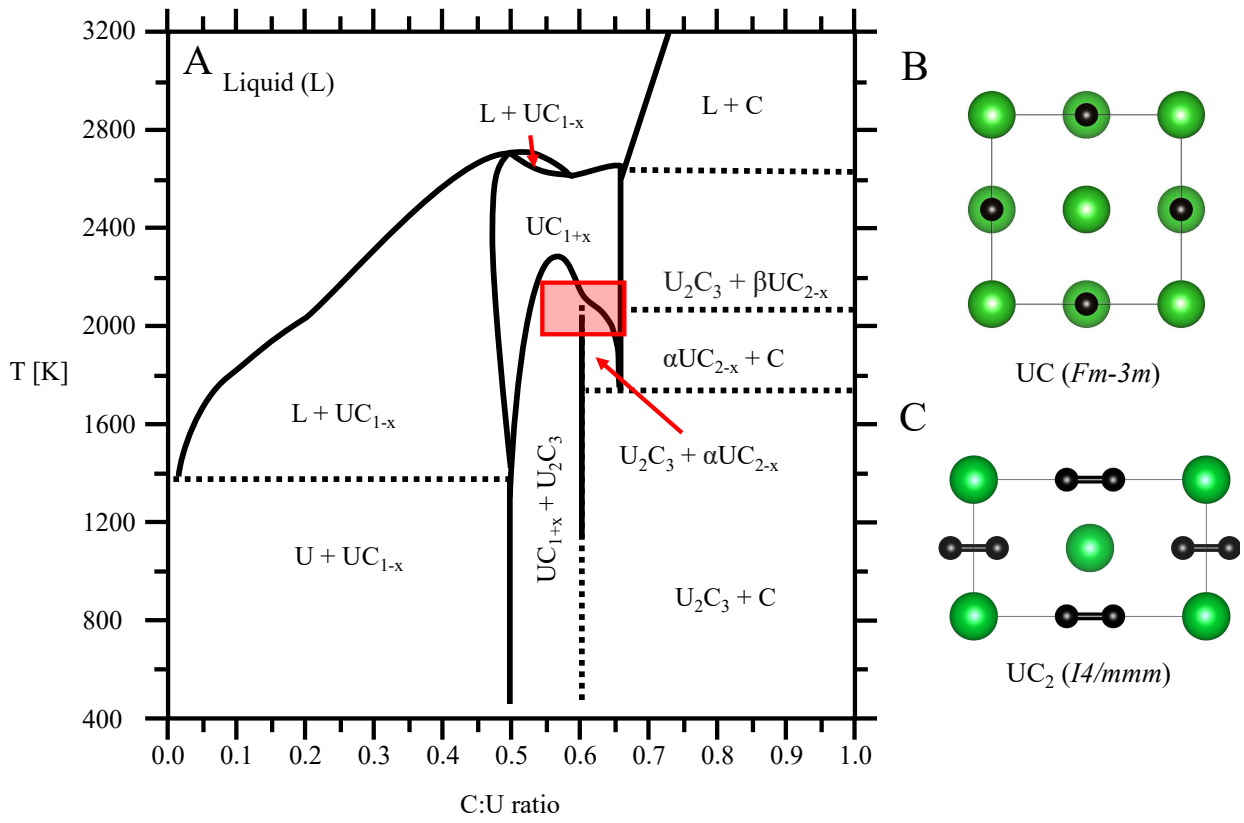

Figure 4. (A) Uranium carbide phase diagram, re-constructed from results compiled within [18]. With the X-axis defined as the stoichiometric ratio of carbon to uranium atoms and the Y-axis being the quench temperature. Red zone indicates the targeted synthesis region for this study. (B) and (C) depict schematics of the primary expected phases from synthesis, UC and UC_2.

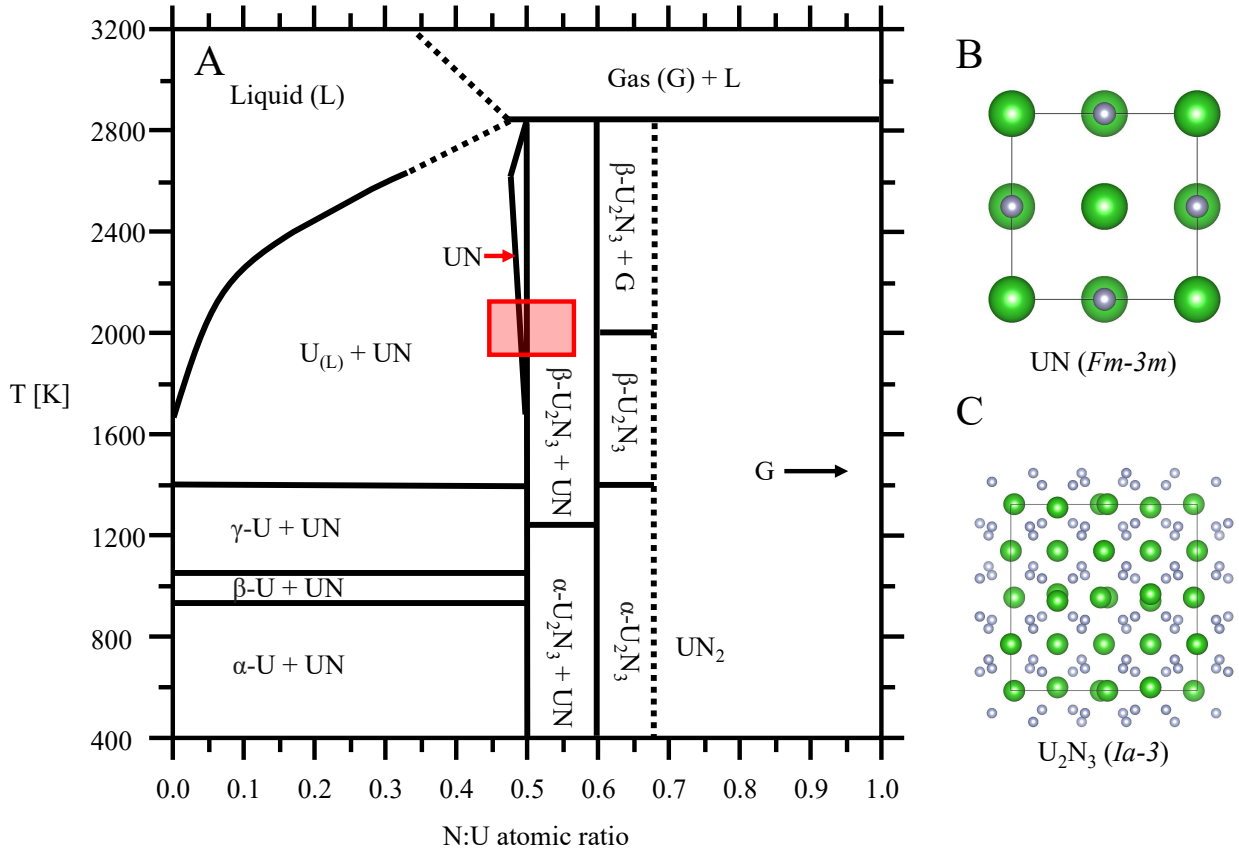

Figure 5. (A) Uranium nitride phase diagram, re-constructed from results compiled within [19], [20]. With the X-axis defined as the stoichiometric ratio of nitrogen to uranium atoms and the Y-axis being the quench temperature. Red zone indicates the targeted synthesis region for this study. (B) and (C) depict schematics of the primary expected phases from synthesis, UC and U_2N3.

1.4 Nuclear Fuel Materials Under Extreme Conditions

Nuclear fuels must maintain structural and thermodynamic integrity in the face of the extremes present in nuclear reactors. In addition to the elevated temperatures, fuel undergoes burn-up which is a complex phenomenon where three simultaneous processes occur that have a dynamic impact on fuel performance [3]. Uranium consumption, radiation release, and creation of fission daughters, all of which modify the chemistry and structure of the fuel compound. The extreme mixed radiation fields consisting of fission fragments, neutrons, and secondary decay particles (*e.g.*, alphas, and betas) all contribute to structure defects (*e.g.*, Frenkel pairs) [6]. Chemical modifications, from both fission daughters and uranium consumption, have a strong interplay with the radiation response complicating the assessment of nuclear fuels. UO_2 is well studied in both reactor environments and individual radiation component simulated environments. With existing studies investigating UHTC materials not being nearly as thorough.

The majority of the radiation energy and dose, as measured by displacements per atom, imparted within nuclear fuel originate from fission fragments. These highly energetic (~70-100 MeV) ions behave much differently than their low-energy counterparts [3]. Previous studies have been conducted on fission fragment damage contributions to reactor fuel form materials, with most of the existing literature focused on UO_2 [17], [25], [26], [27], [28], [29], [30], [31], [32]. Low-energy ions interact primarily through ballistic collisions (nuclear energy loss) wherein Coulombic interactions between the incident ion and target materials nucleus results in the displacement of the atom from its lattice site [33], [34]. Subsequent stages result in the displaced atom recombining in a vacated lattice site or forming an interstitial/vacancy (Frenkel pair) [6]. As the incident ion energy increases interactions become increasingly dominated by electronic energy loss where the ion interacts with the electron cloud surrounding the target materials' atoms [6], [35].

In order to more thoroughly understand the impact of fission fragments on reactor fuel considerations must be made to ascertain the impact of energetic heavy ions (*e.g.*, fission fragments immediately following fission event) on the fuel form materials. Experimentally, irradiating materials with fission fragments alone is impractical due to their very limited penetration depth in uranium bearing materials and difficultly isolating ions [36]. Instead in the work from Cureton, *et al*. so-called *swift heavy ions* (SHI) are utilized as an analog [17]. SHIs are defined as energetic heavy ions with mass greater than that of ^{12}C and kinetic energy of greater than 1 MeV/nucleon [35]. The interaction mechanism between SHIs and the target material differs greatly from that of low-energy ions. Rather than being dominated by displacive (ballistic/nuclear) interactions, SHIs instead interact almost entirely with the surrounding electrons [6], [35], [37]. In many ceramics these interactions, characterized by rapid and intensive heating along the ion trajectory before an equally rapid quench [38], result cylindrically confined zone of material surrounding the ion. Inside the track, a wide range of ion- and material-dependent modifications have been observed ranging from simple point defects to complete amorphization [35], [38], [39], [40], [41], [42]. It is only at the end of the ion range that nuclear energy loss begins to dominate [38]. Ion track formation is a rapid process taking place on femto- to picosecond timescales that culminates in the dissipation of energy from the electrons and to the lattice atoms through electron-phonon coupling [35]. SHIs have been used previously in geological dating and in simulating damage within nuclear waste forms [37], [38]. With TMCs, and UC_xN_{1-x} sufficiently high enough ion energies are required in order to fully penetrate the material [43]. As such, very large ion accelerators are utilized with beam energies exceeding (within one order of magnitude) the maximum energy produced from a fission event [35].

In many materials, swelling from SHI irradiation have been shown to follow a direct-impact model [17], [44], [45], [46]. Within the direct-impact model, defects first are shown to accumulate linearly within individual tracks, before the tracks begin to overlap resulting in a sub-linear trend, and finally the entire sample is covered in tracks resulting in a steady-state condition where defects are produced and annealed at equal rates. This track overlap effect is related both to the ion fluence (ϕ) and a cross-section term (σ), which is directly related to the cross-sectional area of the impinging ion track. In the case of lattice swelling the evolution of the lattice parameter (a) can be described as a function of σ and ϕ using a Poisson equation (eq. 2):

$$\frac{\Delta a}{a_0} = \frac{a(\phi) - a_0}{a_0} = \frac{a_{sat} - a_0}{a_0}\left(1 - e^{-\sigma\phi}\right) \quad (2)$$

Prior studies have shown that similar actinide materials follow this same Poisson trend, in *Cureton et al*., we see both ThO_2 and, to a lesser extent, nanocrystalline UO_2 lattice swelling follows the trend described with eq. (2). While no prior SHI irradiation studies have been conducted on UC_xN_{1-x}, similar studies have found that isostructural surrogate materials zirconium carbide (ZrC) and hafnium carbide (HfC) follow an altogether distinct trend [41], [42]. Both ZrC and HfC exhibit a two-stage swelling mechanism wherein, the first stage is governed by a Poisson trend (eq. 1) before an extended saturation that yields to a continued linear swelling regime. A set of proposed theories discussing the origin of this more complex behavior is discussed in *Minnette et al*, where it is suggested that the intrinsically hypostoichiometric nature of the transition metal carbide compounds may be the primary driver [41].

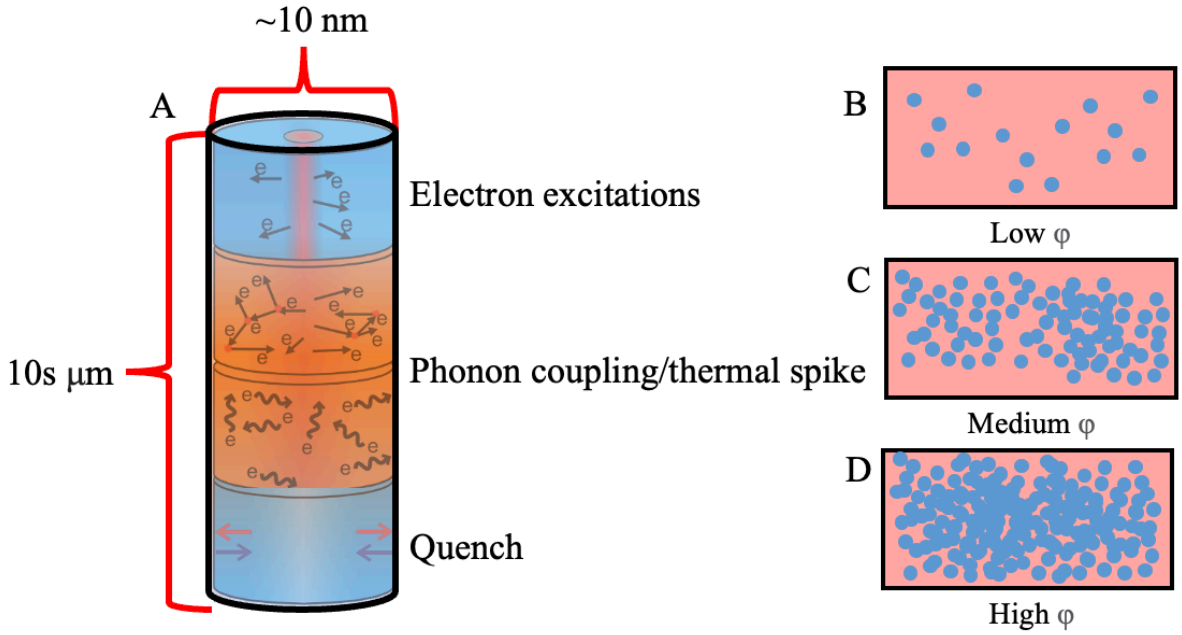

Figure 6. (A) schematic of ion track formed from SHI. (B), (C), (D) demonstration of ion track overlap corresponding to linear, sub-linear, and saturation stages of direct-impact model, eqn. 2. Not drawn to scale.

CHAPTER 2: METHODS AND APPROACH

Portions of this chapter were previously published in the Journal of Applied Physics by Jacob A. Minnette, Evan Williams, William F. Cureton, Alexandre Solomon, Eric O'Quinn, Matthew Kurley, Rodney D. Hunt, Changyong Park, Ina Schubert, Christina Trautmann, and Maik Lang. For these works, J.A.M., E.W., W.F.C., M.K., R.D.H., and M.L. conceived experiments; J.A.M., E.W., W.F.C., A.S., E.O., C.P., I.S., C.T. and M.L. prepared relevant samples and performed formal analysis; J.A.M. drafted the manuscript with input from all co-authors.

In an effort to address the established knowledge gaps, as detailed in the previous section, a series of targeted experimental and computational approaches were developed. These projects were primarily conducted at large user facilities, with all procedures and techniques described in detail below.

2.1 Sample Preparation

2.1.1. Production of transition metal carbides and uranium carbonitrides through internal gelation techniques

The production of surrogate carbides utilized within this study was limited to two primary techniques. Plasma vapor deposition (PVD) produced material from stock vendors, and laboratory produced sol-gel materials (internal gelation based technique). Stock powders were sourced from U.S. Research Nanomaterials with 99.9% metal atom purity in one of two grain sizes. A '*micro*' grained sample (denoted as PVD1 within the *chapter 4*) with a mean reported grain size of 400-1200 nm and a '*nano*' grained sample (denoted as PVD2 within the *chapter 4*) with a mean reported grain size of 20 nm. Two sets of spherical sol-gel ZrC samples (SG1 and SG2 within the *chapter 4*) were prepared at Oak Ridge National Laboratory (ORNL), a detailed description of this process is specified in prior work from Huston *et al*. and Hunt *et al*. [16], [47]. The mean grain size of the sol-gel produced ZrC was determined to be 40-320 nm [16]. Both sets of sol-gel samples were

produced with a precursor molar ratio (C:ZrO_2) ratio of 3.0 following eqn. 3. For the study of surrogate carbides (ZrC) we establish a benchmark comparison to a well-studied oxide surrogate, CeO_2 [17], [41]. The CeO_2 sample utilized within this study was purchased from Alfa Aesar at 99.99% cation purity with a reported mean grain size of 600 ± 200 nm, as calculated from Williamson-Hall analysis [41], [48]. All surrogate materials specified here were included within the studies conducted as a part of *chapter 4*. Table 1 provides a summary of the samples that were utilized in this study.

For the actinide carbides/nitrides all samples were produced *via* the internal gelation pathway at ORNL. Precursor transition metal and uranium oxides spheres can be mixed with variable ratios of carbon black (elementally pure amorphous carbon) to form colloidal spheres in the form of acid-depleted uranyl nitrate (ADUN) [49]. Variable ratios of carbon to metal oxide molecules (C:M) were calculated beforehand in order to synthesize specific stoichiometries of the final compound. This was done in accordance with the following equations for ZrC (the primary transition metal carbide evaluated in this study) and UC_xN_{1-x} [16], [50].

$$ZrO_2 + 3C \rightarrow ZrC + 2CO_{(g)} \quad (3)$$

$$UO_3 + C \rightarrow UO_2 + \frac{1}{2}C + \frac{1}{2}CO_{2,(g)} \quad (4)$$

$$UO_2 + (3-2y)C \rightarrow UO_yC_{1-y} + (2-y)CO_{(g)} \quad (5)$$

$$UC + N_{2,(g)} \rightarrow UC_xN_{1-x} \quad (6)$$

The process of converting the individual precursor components, UO_3 and C for instance, into the final carbide/nitride form, UC_xN_{1-x} as described in equations (3) through (6), is known as carbothermic reduction (CTR).

Table 1. Summary of ZrC and CeO2 sample types used within this irradiation study.

Chemical Composition	**Sample Name**	**Synthesis Technique**	**Grain Size [nm]**	**Cation Purity**	**Produced**	**Ref.**
ZrC	PVD1	Vapor Deposition	400-1200	99.9%	U.S. Nanomaterials	[16]
	PVD2	Vapor Deposition	20	99.9%		
	SG1	Sol-gel	40-320	99%	ORNL	[16], [47]
	SG2	Sol-gel	40-320	99%		
CeO_2	Micro-CeO_2	Vapor Deposition	400-800	99.99%	Alfa Aesar	[17], [40], [51]
	Nano-CeO_2	Vapor Deposition	20	99%	UTK	[17], [40]

This process is conducted under an inert, reducing atmosphere (*e.g.*, argon) or, in the case of nitride production, N_2 [19], [88], [89]. This extra nitridation process (*eqn. (6)*) is known as carbothermic reduction plus nitridation (CTR-N). To produce a nominally stoichiometric (*i.e.*, carbon:metal atomic ratio = 1) a precursor ratio of ~3:1 carbon-to-metal oxide is required. The diameter of the UC_xN_{1-x} spheroids are, however, much larger than the surrogate counterparts (~3x) as determined by SEM [16]. The synthesis pathway was also designed to closely follow the procedure utilized for the kernel production within TRISO. Precursor UO_3 was produced following the procedure specified by Hunt *et al*. [52]. Raven carbon black (amorphous elemental carbon) was then combined with the spheroids in various ratios, see table 2 for specifications. For the uranium carbide sample (denoted as UC in *chapters 3* and *5*), a C:U ratio of 3.5 was utilized. The designed goal here was to produce hyperstoichiometric UC_2 rather than have residual, unconverted oxide/oxycarbide impurities. The CTR process follows eqn. (4) and (5) and was conducted under an inert, reducing atmosphere of 96 % argon with 4 % hydrogen (H_2) gas. For the uranium nitride sample (denoted as UN in the *preliminary results* section), a C:U ratio of 2.8 was utilized. CTR process occurred under a N_2 atmosphere rather Ar + H_2 in order to promote the nitridation process (CTR-N) as specified in eqn. (6). A subsequent argon gas purge was conducted for the UN sample to minimize potential oxidation through ambient atmosphere exposure. The 2.8 C:U precursor ratio utilized with the UN sample creates a hypostoichiometric compound that results in a variety of nonstoichiometric impurity, and carbide phases, a detailed description of the findings are specified in the *chapter 3*. The heating rates across all synthesis runs was kept constant at 10 ºC/min. As a benchmark for comparison, a UO_2 sample was additionally prepared through an internal gelation pathway. The sample precursor gelatinous spheroids of UO_3 were reduced under a similar atmosphere as that of the UC sample until a nominal stoichiometry of UO_2 was achieved.

Table 2. Summary of input synthesis parameters for uranium bearing samples as utilized within projects 1 & 3.

Sample	**C:UO_3 Molar Ratio**	**Hold Temperature [°C]**	**Gas Profile**
UC	3.5	1800	Ar
UN	2.9	1800	N_2 + Ar purge
UO_2	n/a	1800	Ar

2.1.2. Sample preparation for ion beam irradiations

In order to ensure uniform sample irradiations all materials utilized in this study were prepared according to guidance specified in previous studies [44]. Here, powderized samples were mechanically pressed into thin strips of foils. For the surrogate materials (ZrC) evaluated within this study 12.5 and 25 μm thick light-tight molybdenum (99.9 % purity) foils sourced from GoodFellow. Actinide materials were similarly prepared, however, instead of molybdenum foils, a 10 μm thick light-tight 304 austenitic stainless steel foil was utilized, also sourced from GoodFellow. The difference between the two foils was dependent on ion penetration depth within the sample (described in *subsection 2.2*). Pressed samples were uniaxially pressed with a force of 3-4 tons across a die with a diameter of 2 cm.

Prior to pressing, the actinide samples had to be pre-ground in order to reduce grain size as determined by SEM and Williamson-Hall analysis (described in *subsection 2.3.4 and 2.3.5*). In order to ensure homogenous irradiation and minimize texture effects in powder diffraction techniques (described in *subsection 2.3.1*) grain sizes must ideally be within 10-2000 nm [44], [53]. For the surrogate materials (both sol-gel and PVD synthesized) this grain size constraint was already met and confirmed through prior studies [16]. Grinding was conducted within an inert, atmosphere controlled glovebox through collaboration at the University of Texas at San Antonio. Grinding was conducted in a four-step process. The first step consisted of utilizing an agate mortar and pestle, grinding the spheroids (one sample at a time) for 10 minutes. Powder was then passed through an aluminum sieve with a mesh size of 38 um (Figure 7). Residual powder that did not pass through the sieve was reground for another period of 10 minutes and passed through the sieve again.



Figure 7. Agate mortar and pestle used for sample grinding alongside sample sieve.

Steps 3 and 4 consist of SEM and post-processing conducted with ImageJ to determine mean grain size and confirm if the constraint of a maximum 2 um grain size was met (described in *subsection 2.3.4*) [54]. Subsequent grinding was conducted as needed. The equipment was thoroughly cleaned between all samples to prevent contamination. Samples were sealed within the glove box and sent back to UTK to minimize the potential for ambient oxidation. All other procedural details for sample preparation follow the detailed specifications in Lang *et al*. [44].

2.2 Irradiation with Swift Heavy Ions

SHI irradiations were conducted at two different facilities. For the majority of the work to be conducted on surrogate carbides, detailed in *chapter 4*, the M-branch (M3 beamline) at the GSI-Helmholtz center was utilized. Irradiations of ZrC were conducted here with 946-MeV $^{197}Au^{28+}$ ions with various fluence points ranging from unirradiated to a maximum fluence of 6×10^{13} [ions/cm^{-2}]. Irradiations were conducted at room temperature and *in vacuo* (nominal pressure of ~10^{-3}-10^{-5} mTorr). A defocused ion beam was utilized with a size of ~1×1.5 cm^2 at an average sustained beam flux of 2×10^9 cm^{-2}s^{-1}. Irradiations of ZrC samples were conducted across multiple beamtimes with identical conditions maintained between various irradiation experiments. The rest of the surrogate carbides and uranium-bearing carbide samples were irradiated in 10 μm thick strips at the DC-60 accelerator complex within the Kazakhstan Institute of Nuclear Physics (INP). 198-MeV $^{32}Xe^{20+}$ ions at an average flux of 2×10^9 cm^{-2}s^{-1} across a similar 1×1.5 cm^2 area. 12 fluence steps ranging for unirradiated to 8×10^{13} cm^{-2}s^{-1} were selected with the guidance from the results in *Chapter 4*. The range of the ions for both irradiations will be calculated beforehand using the SRIM utility, which demonstrated complete penetration with 1-2 orders of magnitude more electronic energy loss relative to nuclear energy loss, see figure 8 [43].

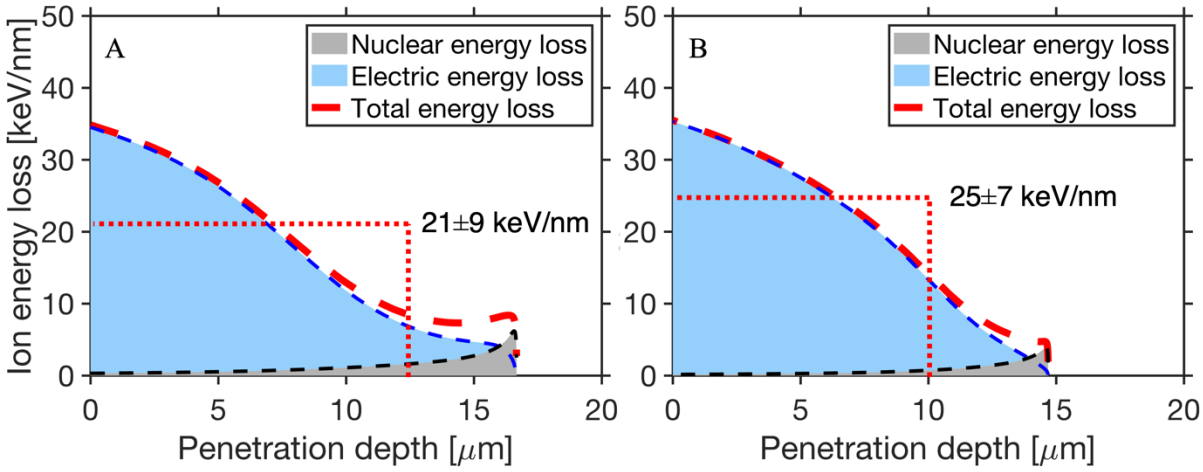

Figure 8. SRIM calculated ion energy loss as a function of depth into (A) ZrC and (B) UC for Xe 198 MeV ions. Mean stopping power shown with red dashed lines [41].

2.3 Advanced Characterization Methods

Central to this project is work focused on advanced experimental characterization methods of UHTCs. To achieve this goal, we focus on multi-scale, high resolution, high throughput techniques. Specifically, for crystal structure measurements we employed synchrotron XRD measurements, both for microdiffraction (used to characterize SHI irradiated samples) and bulk powder diffraction (used to characterize "*as-synthesized*" samples). Complementary to XRD is neutron total scattering which amplifies the scattering intensity of the lighter non-metal atoms, see figure 9. Multiple length scales, from sub-nanometer atomic bonding to bulk SEM measurements were utilized. The set of techniques described in the following subsections detail the comprehensive analytical strategy to ascertain all structural, chemical, and thermodynamic based material parameters.

2.3.1 Synchrotron X-ray Scattering Experiments

X-ray scattering experiments were conducted at two separate facilities depending on the material. For bulk characterization of the *as-synthesized* material (UC_xN_{1-x}), described in greater detail in *chapter 3*, total scattering experiments were conducted at the National Synchrotron Light Source (NSLS-II) at Brookhaven National Laboratory. For microdiffraction characterization of SHI irradiated material, ZrC as described in *chapter 4* and UC_xN_{1-x} as described in *chapter 5*, X-ray diffraction data was collected at the Advanced Photon Source at Argonne National Laboratory. Both procedures utilize transmission mode X-ray diffraction, figure 10.

Experiments involving *as synthesized* (non-irradiated uranium fuel kernels) were conducted at the X-ray Powder Diffraction (XPD, 28-ID-1) beamline with a monoenergetic X-ray beam of 75 keV ($\lambda = 0.1665$ Å) focused and collimated to a beamspot area of 0.6 mm × 0.2 mm.

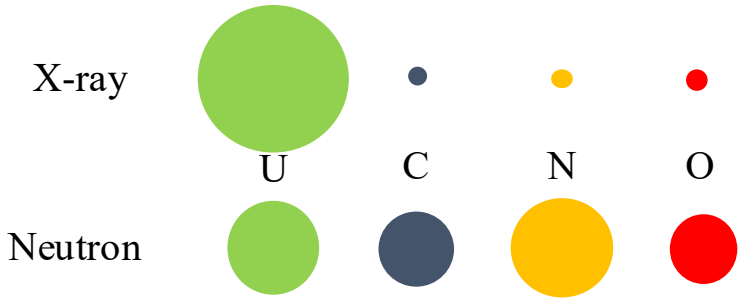

Figure 9. Effective sensitivities for relevant elemental species for UC_xN_{1-x} system for X-rays, and neutron elastic scattering.

Uranium-bearing samples were loaded into thin-walled Kapton tubes (0.0395 mm internal diameter) which were then loaded into larger diameter Kapton tubes (0.0578 mm) to double encapsulate the sample (figure 11). After preparation, foam stoppers were installed into either end of the 30 mm Kapton tubes. Both ends of the inner tube were then sealed with epoxy before being nested within the larger tube, which was likewise sealed with epoxy. The schematic shown in figure 11, details the process utilized for this study. Similar studies for ZrC were conducted in Kapton tubes without double-encapsulation, *i.e.*, powder loaded directly into 0.0395 mm internal diameter tubes [16]. Before being capped with foam stoppers on either end. During exposure, the beam was rastered from top-to-bottom of the Kapton tube with 7 total measurements being taken over the length of the Kapton tube during a total measurement time of 60 seconds per sample. A Pilatus3 CdTe 1M 2D plate detector, mounted onto an adjustable rack, was used to measure scattered photons at variable sample-detector distances. This enables collection of diffraction data with high-resolution and low angular coverage (~1000 mm), ideal for conventional diffraction pattern analysis, as well as diffraction data with high angular coverage (~270 mm), ideal for the production of high-fidelity pair distribution functions. Calibration measurements were collected with LaB6, ZnO, ZnO_2, Ni, and a blank Kapton tube entirely filled with foam stoppers which was used to correct for the amorphous sample containment signal contribution. This process was completed for both the single tube and nested tube (radioactive containment version) configurations. In the XRD sampling geometry the detector was mounted 1 meter from the sample magazine. This enables a full range of angles to help probe relevant crystallographic planes out to ~10 $Å^{-1}$. For the PDF geometry the sample-to-detector was much shorter, this distance was chosen to optimize for low-scattering angle contribution, used to probe short-range bonding within the materials.

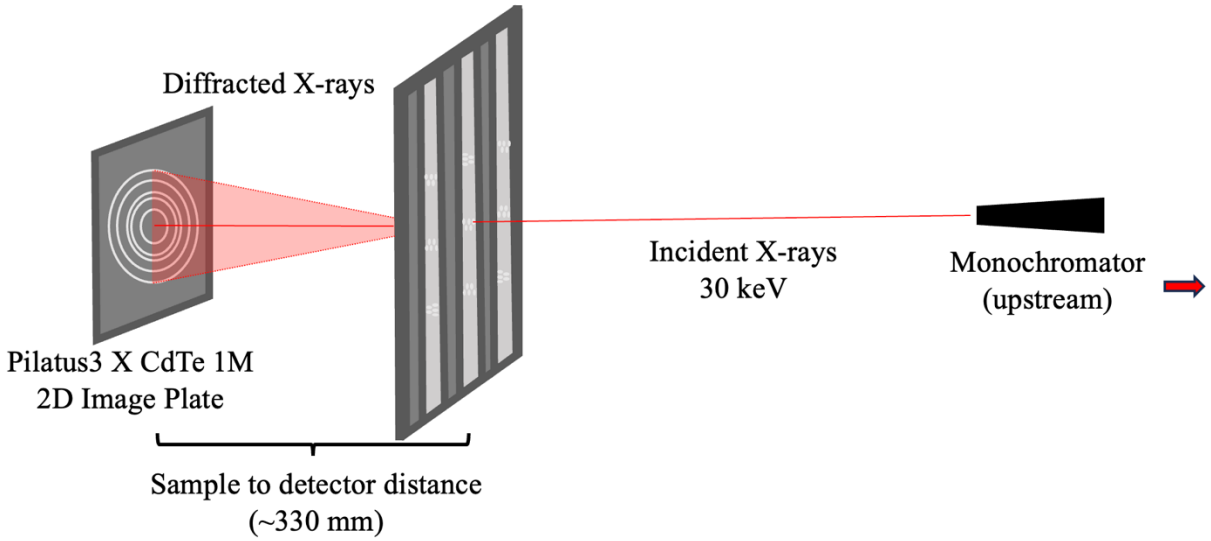

Figure 10. Schematic of transmission mode μXRD at HPCAT (not drawn to scale). Similar beam and detector geometry at NSLSii.

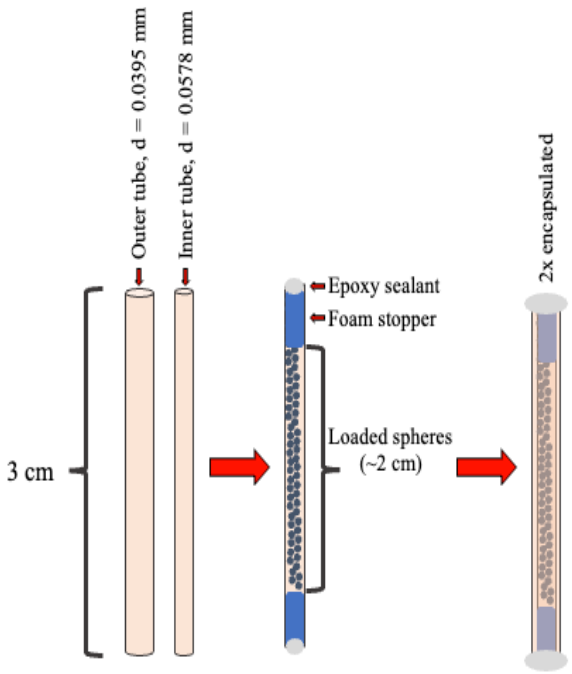

Figure 11. Simplified schematic of loaded fuel kernels within Kapton for X-ray diffraction measurements.

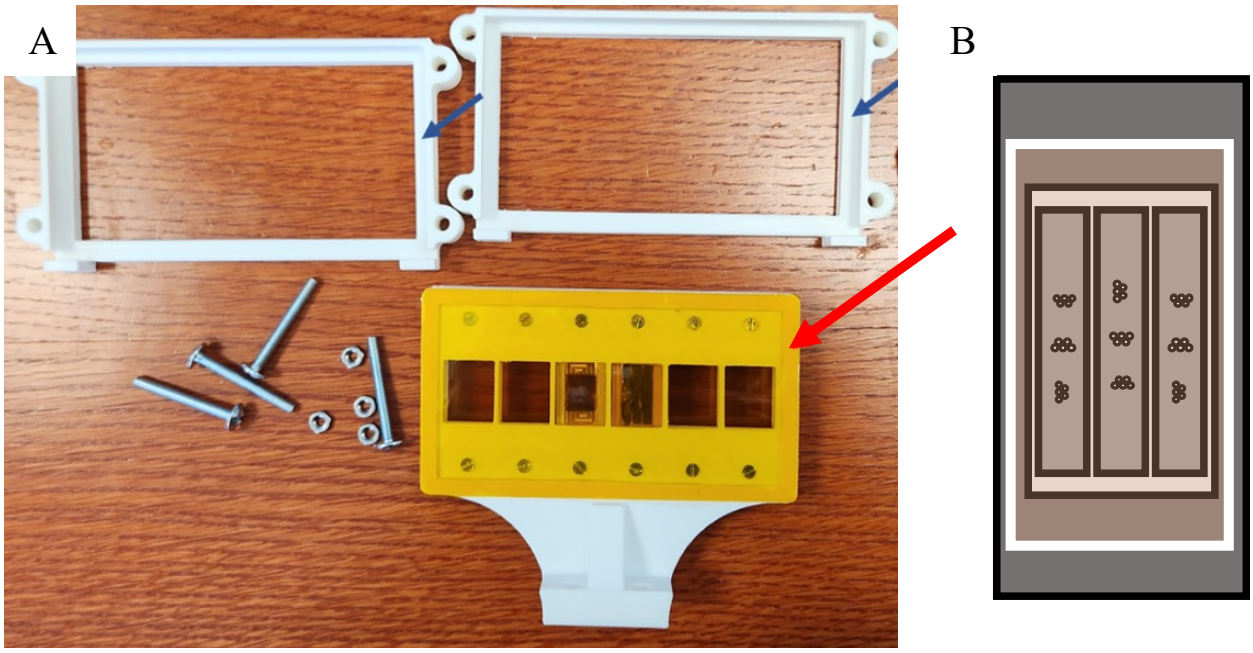

Figure 12. Custom manufactured double-encapsulation sample holder. (A) picture of master test assembly, 1×6 array for aluminum frames affixed with BKL-4 compatible mount. Outer Kapton layer glued onto frame with PLA bracket bolted overtop. (B) Schematic of individual aluminum from with Kapton window affixed with PLA bumper (mirrored on reverse side).

X-ray diffraction analysis of all irradiated sample specimens were performed at the Advanced Photon Source at Argonne National Laboratory at the 16-BM-D beamline endstation. Due to facility safety restrictions all uranium-bearing samples (UC, UN, & UO_2) had to be contained with a double-encapsulated sample holder. To accommodate this, a PLA 3D-printed sample holder was designed and produced to fit to a BKL-4 standard sample mount, shown in figure 12. Otherwise, samples were measured directly on aluminum holder mounts as described in Lang, *et al* [44]. This holder maintained compliance with facility safety standards, eliminating any detectable dose beyond the containment. 30 keV photons were produced following a Si (111) double-crystal monochromator with an approximately constant photon flux of 5×10^8 photons cm^{-2}. The beamspot was collimated down to 5x5 μm^2 area to help isolate diffraction contributions from the stainless steel strips. The produced Debye-Scherrer rings were collected in transmission geometry using a Pilatus3 X CdTe 1M 2D image plate detector, more details about this end station can be found here [55]. A National Institute of Standards and Technology (NIST) compressed powder CeO_2 sample was used to calibrate the instrument and validate the prior beam characteristics. Prior to each individual XRD measurement, samples were aligned in the X, Y, and θ_Z directions to ensure a centered, orthogonal sample to the incident X-ray beam. Three minute exposures were performed with a XY raster across 50 μm. Additional XRD measurements were taken of empty sample holes to account for background signal contributions from the steel foil and Kapton plastic containment system.

2.3.2. Neutron Total Scattering Experiments

Neutron total scattering measurements were conducted using the Nanoscale Ordered MAterials Diffractometer (NOMAD) instrument [56] of the Spallation Neutron Source (SNS) at ORNL. The NOMAD beamline is particularly well suited for this project [57] as it provides rapid

high quality pair distribution function data on a variety of materials through its world-class flux and wide detector coverage of reciprocal space, Q:

$$Q = \frac{4\pi \sin\theta}{\lambda} \tag{7}$$

where θ is the neutron scattering angle and λ is the neutron wavelength. Approximately 200 mg of UC and UN samples were loaded into 3 mm diameter quartz capillaries to a height of ~2 cm and exposed to the neutron beam for 1 hour. Instrument calibration was conducted across all six time-of-flight (TOF) detector banks using both diamond and silicon powders. Calibration measurements were taken with empty, and diamond filled quartz capillary tubes for necessary background corrections and a vanadium rod for normalization to the neutron spectrum [56].

2.3.3. Raman Spectroscopy

Confocal micro-Raman spectra were collected at room temperature utilizing a Horiba Scientific LabRAM HR Evolution spectrometer. Uranium bearing samples were isolated in an aluminum containment chamber with a clear glass viewing window to both minimize contamination and laser-induced oxidation risk. For UC and UN samples a 532 nm wavelength was found to produce the most optimal signal resolution and was operated at 1.6 mW. For UO_2 Raman modes were maximized with a 785 nm wavelength laser operated at 1.8 mW. All signal collections were taken over 60 seconds with 2 accumulation cycles per measurement. Where possible, multiple measurements were taken per sample per fluence. A 20x long-working distance Olympus objective was utilized to record the spectra with an 1800 g/mm holographic grating. The spectra were collected over a range of 100-1800 cm^{-1}. Liquid nitrogen was used with a cooled charged coupled (CCD) detector to maximize signal resolution.

2.3.4. Scanning Electron Microscopy & Energy Dispersive Spectroscopy

SEM was collected following XRD characterization. Both a pristine and heavily irradiated pellet was selected for both UC and UN samples. These samples were removed from their respective strips and placed onto a conductive piece of graphite tape (used to prevent charge build-up within the sample). A FLEXSEM1000 SEM was used to analyze the samples with all preparation work being conducted under an inert atmosphere (in a manner similar to the grinding procedure described prior) before being loaded into the SEM. This was done in an effort to minimize environmental contamination. Images were collected using the secondary electron detector with a preset voltage of 15.0 kV. Subsequent EDS was performed to help diagnose chemical variance across the sample.

SEM data was processed using ImageJ, an image processing software developed by the National Institutes of Health [54]. In this process the image scale was calibrated for each micrograph according to the outputted scale bar from the SEM. Two parameters were measured in the micrographs: spheroid diameter, and surface grain size. Surface grains were measured from visible topographic undulations, with the reported grains being measured across their longest dimensions (Ferret diameter) [58]. Grains near the periphery of the visible spheroids were excluded due to aberrations introduced from the spheroids' curvature.

2.3.5. Data Analysis from X-ray and Neutron Scattering Experiments

All collected XRD data were be processed and reduced from a 2D image of diffraction rings to a 1D diffraction pattern using Dioptas, an open-access software distributed by Argonne National Laboratory [14]. Rietveld refinements for both XRD and neutron diffraction were performed using GSAS-II [59]. Sample properties such as the global scale factor, unit cell parameters, atomic displacement parameters, stoichiometry, microstrain, and phase fractions were

refined. Williamson-Hall analysis was performed on all XRD datasets to ascertain strain and particle domain size of all present phases using the following relations [48]:

$$\beta_{sample} = (\beta_{obs}^2 - \beta_{ins}^2)^{1/2} \tag{8}$$

$$\beta_{sample} \cos(\theta) = 4\varepsilon \sin(\theta) + \frac{K\lambda}{d} \tag{9}$$

Where β, is the peak broadening (FWHM) term defined from the observed measurement, sample, and instrument (detector, source, etc.). ε, represents the heterogenous microstrain of the sample, and θ, is the half scattering angle of the diffracted X-rays. K is a shape adjustment factor, typically taken to be 0.9, λ, is the wavelength of the X-rays, and d is the material's coherent domain size.

Neutron total scattering data (S(Q)) contains both the long-range structure (resolved from Bragg peaks) and information about local atomic correlations present in the diffuse scattering, see figure 12. The structure of these local atomic correlations are extracted by analyzing the neutron pair distribution function (PDF). The PDF, G(r), is calculated through a Fourier transformation of the reciprocal-space data with a Q_{min} of 0.2 Å^{-1} and an optimized Q_{max} of 35 Å^{-1}.

$$G(r) = \frac{2}{\pi} \int_{Q_{min}}^{Q_{max}} Q[S(Q) - 1] \sin(Qr)\, dQ \tag{10}$$

The PDFs were refined using small box modelling in PDFgui [60]. This method produces analogous results to a conventional Rietveld refinement of the long-range structure. Global scale, phase concentrations, unit cell parameter, static atomic site displacements, atomic site occupancy, and atomic displacement parameters (thermal contributions) were determined. The refinements were performed over a range of 1-9 Å, to highlight the local (sub-nanometer) structure. Additional sliding '*box-car*' refinements were conducted with varying *r*-values while maintaining the same window size of 8 Å. Each successive box-car refinement window was adjusted +5 Å.

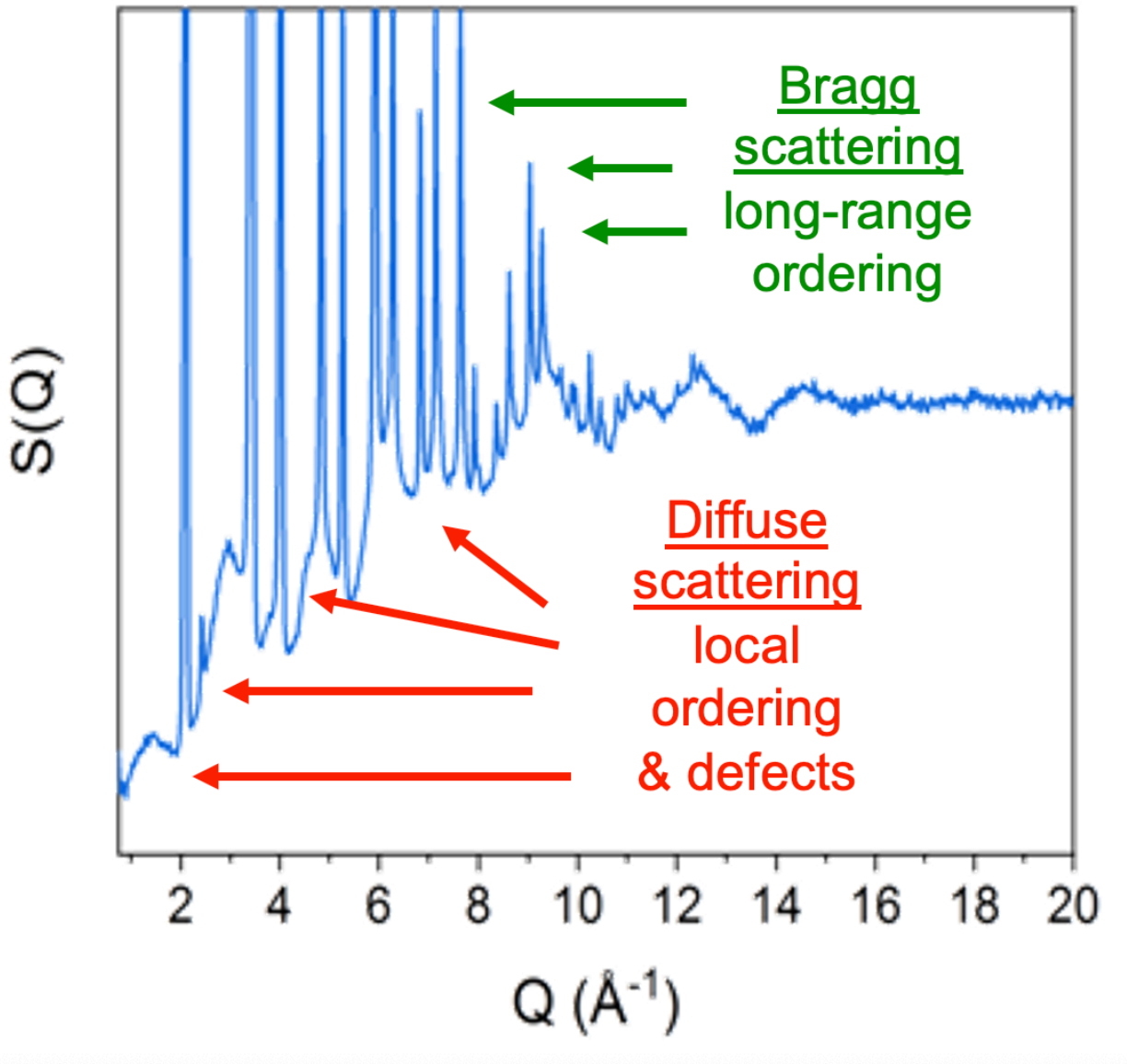

Figure 13. Simplified schematic of a representative total scattering data output. Sharp peaks labeled in green correspond to Bragg peaks (contributions from the long-range or average structure). Diffuse scattering is represented by peak widening at the bottom ~20 % of the Bragg peak and contains information relevant to the local (atomic) structure, shown labeled in red.

PDFgui refinements of the ZnO and Ni X-ray calibration measurement is utilized to establish a beamtime relevant Q_{damp} (0.040946 $Å^{-1}$) and Q_{broad} (0.03162 $Å^{-1}$) value [61]. For neutron PDF, beam and detector stability allow for consistent values of Q_{damp} and Q_{broad} to be utilized that are defined in previous instrument measurements [56].

2.3.6. Thermogravimetric Analysis and Differential Scanning Calorimetry

Thermogravimetric Analysis (TGA) and differential scanning calorimetry (DSC) were used in tandem to help inform the initial starting chemical components for UC, UN, and UO_2. To accomplish this, TGA assesses mass changes of the samples when exposed to a simulated atmosphere consisting of 80 Vol. % N_2 and 20 Vol. % O_2. DSC works in a similar manner but instead measures heat flow, for these experiments TGA and DSC were completed simultaneously using a Setaram SETSYS Evolution differential scanning calorimeter. Data collection was conducted with a S-type DSC plate rod. For all experiments the initial sample mass was near constant (~10 mg), material was loaded into an alumina (Al_2O_3) crucible and placed on the instrument stage. The sample was heated from room temperature to 1000 °C at a rate of 10 °C/min. Heat flow interference from the Al_2O_3 was accounted for through base line subtraction of a blank run. These experiments also offer insight into the oxidation behavior and kinetics used to better inform impacts from irradiation preparation or the irradiation itself.

CHAPTER 3: MULTI-SCALE CHARACTERIZATION OF URANIUM CARBIDE AND NITRIDE

The following chapter presents a comprehensive framework for multi-lengthscale (angstrom to micrometer) characterization of uranium carbide and nitride, both of which are candidate materials for TRISO fuel kernels. Understanding the structural morphology of these materials under industrial standard synthesis processes is essential to determine what impacts ion irradiation (and other relevant extreme conditions) have on kernel materials. To accomplish this objective the following questions must be addressed:

1. What is the phase composition of the samples as produced following the carbothermic reduction procedure?
2. What variance is observed when comparing X-ray scattering data to neutron scattering data?
3. What can be observed with advanced characterization that traditional characterization may otherwise miss?

3.1 ABSTRACT

Advanced nuclear fuel compounds, uranium carbide and uranium nitride were synthesized *via* an internal gelation (sol-gel) procedure, and the resulting ceramics were analyzed in detail by advanced characterization techniques. Uranium carbide and nitride were produced in a standardized manner employed to produce TRISO particles, prior to pyrolytic carbon coatings. Characterization was based on synchrotron X-ray and spallation neutron total scattering, which enable comprehensive and multi-scale structural assessment of the actinide ceramics with sensitivity to all atomic constituents. The synthesis resulted in microspheres in both compounds with a narrow size distribution of about 0.8 mm diameter and a grain size on the order of a few μm. The uranium carbide spheres contained 80% UC and 20% UC_2 without any other detectable

impurity phases. UN consisted of 96% rocksalt and 4% (α - *Ia*-3) uranium sesquinitride (U_2N_3). The high-resolution diffraction data revealed that rocksalt structured UN is comprised by two distinct carbon-impurity rich rocksalt UN phases. Scanning electron microscopy confirmed that samples were homogenous throughout the entire microsphere with no detectable phase separated regions. Local structural characterization complemented long-range diffraction data, providing insight into the atomic bonding environment of the primary rocksalt phases and impurity phases. High temperature calorimetry analysis corroborated the structural data and revealed a two-stage oxidation reaction for both samples, offering an indirect confirmation of binary phase system as resolved from X-ray and neutron scattering analysis. This study shows how complementary state-of-the-art characterization can infer subtle structural information on advanced nuclear fuel forms, which will be important to optimize synthesis of these materials and provide key experimental data for modeling of the behavior of complex carbide/nitride materials.

3.2 INTRODUCTION

Uranium carbide and uranium nitride are two candidate materials for usage within accident tolerant fuel (ATF) [62]. Next generation (gen-IV) reactor concepts require elevated heat generation to optimize for reactor efficiency and to increase safety tolerance in reactor operation [4]. ATF concepts, prominently TRIstructural ISOtropic (TRISO) coated particle fuels, are an attractive option that take advantage of a spherical design consisting of concentrically layered composite coatings, all with high thermal conductivity [1], [62], [63]. At the center of a TRISO particle is the fuel kernel, which contains the uranium-bearing material, and additional layers of carbon and SiC complete the particle. TRISO particles are then suspended in a matrix of graphite that is contained either in the form of a large “pebble” or cylindrical pellet [1], [2]. This is in contrast to previous generation reactor designs (gen-II and -III), which almost exclusively use

sintered monolithic UO_2 pellets [3]. Although comparatively complex, ATF concepts are desired for industry power generation given their ability for usage in high-temperature gas-cooled reactors (*e.g.*, XE-100) and their experimentally demonstrated high fission product retention [64].

Uranium carbide and nitride may be produced through a number of different synthesis pathways, including chemical vapor deposition, arc melting, magnetron sputtering, and wet chemistry methods [65], [66], [67], [68], [69], [70], [71], [72]. While many of these techniques offer advantages pertaining to chemical or structural (phase) purity, they lack the ability to produce high throughput spherical particles needed for TRISO kernel production. The most prevalent for TRISO kernel production is solution gelation (sol-gel) [73]. Here, gelatinous precursor material UO_3 is drop-wise distributed into a solution, or "broth", to form colloidal spheroids [52], [73]. These spheroids are then mixed with a carbon source (*e.g.*, carbon black) for further processing. Carbothermic reduction (CTR) follows, where at high temperatures, within an inert reducing atmosphere, the precursors undergo a transformation into the final carbide and nitride chemical forms [65], [73]. The synthesis of uranium carbide and nitride kernels *via* sol-gel techniques has three key variables: stoichiometric ratios of precursors, CTR hold temperature, and atmospheric conditions. Understanding how these parameters affect the final fuel material in terms of chemical composition, phase purity, and structural properties is still incomplete; however, the quality of the initial kernel material greatly impact the safe performance of the nuclear fuel. The phase diagrams of uranium carbide and nitride demonstrate the complexity of these systems [18], [19], [20], and demonstrate how minor deviations in stoichiometry can greatly affect the resulting phases (Figures 4 & 5).

Laboratory-based X-ray diffraction (XRD) and electron microscopy are two primary characterization techniques for nuclear materials [65], [73], [74]. While these techniques are

readily accessible, they have limitations in resolution, as well as, in their sensitivity to lighter atomic constituents. In general, they provide only information on the long-range structure of a material but, lack insight into short-range ordering effects [57]. In this study, complementary scattering experiments with synchrotron X-rays and spallation neutrons were employed to gain detailed insight into the structure of UC and UN compounds synthesized *via* a sol-gel process. Rietveld refinement of X-ray and neutron diffraction data provided insight into the long-range structure of both materials, while neutron pair distribution function (PDF) analysis gave additional information on the local atomic arrangement. The combined use of X-ray and neutron scattering at large user facilities provides sensitivity to all atomic species (uranium with X-rays, nitrogen, carbon, and oxygen with neutrons). This information was complemented by additional characterization using electron microscopy, Raman spectroscopy, and calorimetric techniques.

3.3 RESULTS

The following section summarizes the experimental findings, as well as the results from the processed data as collected. All data were collected, processed, and refined using the techniques described previously in *chapter 2*.

3.3.1 Scanning electron microscopy

SEM micrographs confirm that the utilized sol-gel synthesis approach yields high-quality microspheres of UC and UN (Figures 14 and 15). Based on measurements of 34 UC spheres, the average diameter and standard deviation is 170 ± 30 μm, with a mean grain size (defined from the surface level undulations) of 6 ± 2 μm. The UC spheres are regular in shape with a relatively narrow diameter distribution. In contrast, there was a slightly larger number of UN spheres with a more irregular, non-ideal spherical shape.

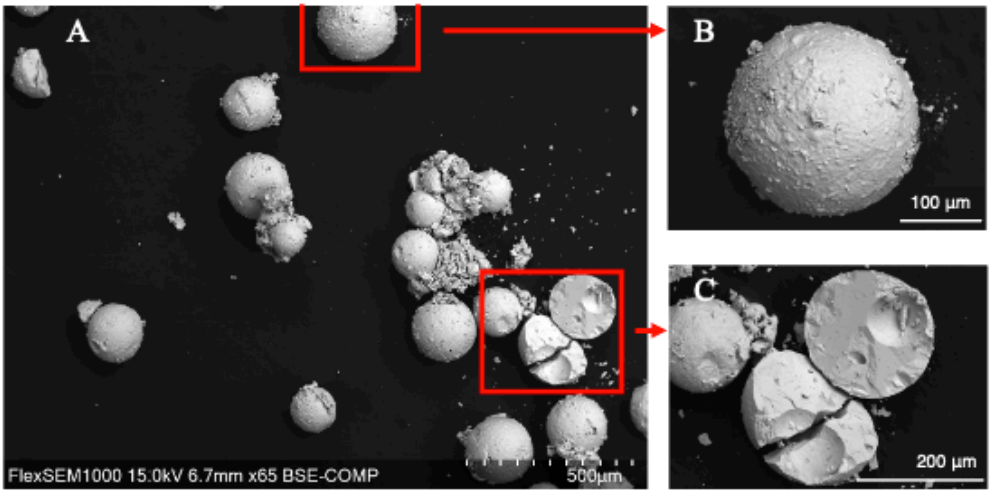

Figure 14. (A) Uranium carbide spheroids shown at 65x magnification with selected spheroids shown at enhanced magnification in (B) & (C).

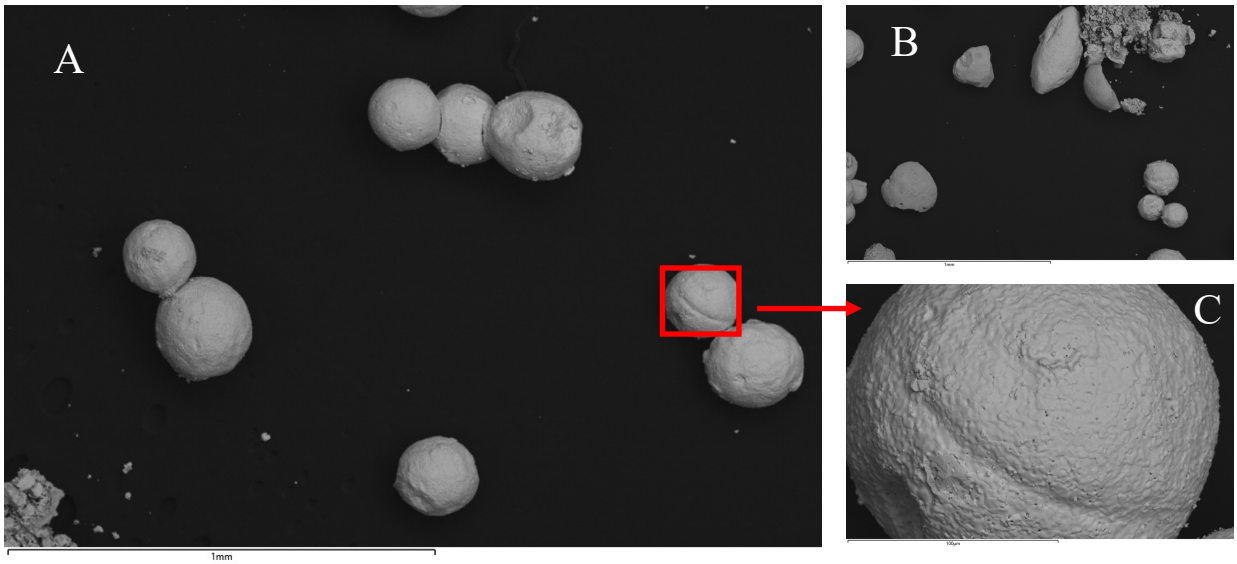

Figure 15. (A) Uranium nitride spheroids shown at 30x magnification with selected spheroid shown at enhanced magnification in (C). (B) Demonstrates inhomogeneities within sphere size and shape.

Measurement on 36 UN spheres revealed an average diameter and standard deviation of 180 ± 40 μm, which is similar to the size of UC spheres; also, the grains size was similar with 6 ± 4 μm (Figure 14 (c)). SEM analysis demonstrated a high degree of microstructural homogeneity with a uniform, dense grain packing and no visual indication of compositional variations. This is in contrast to surrogate material ZrC which was synthesized in much the same manner but resulted in compositionally pure, porous grain structured microspheroids [16]. The shape of individual grain is elongated for both materials (e.g., Figure 15 (c)) and limitation in resolution impede evaluation of grains smaller than 1 μm, which likely explains the skew of distribution to larger grain sizes.

3.3.2 Diffraction pattern analysis

X-ray and neutron diffraction patterns were collected from the as-prepared materials. The diffraction patterns of both kernel samples are fully crystalline materials and exhibit, a predominantly, an *Fm*-3*m* rock-salt structure. Both X-ray and neutron patterns are very similar, with the only immediately discernable differences coming as a result of intensity fluctuations. This of course is expected, as the different instruments (neutron beam, and X-ray beam) possess vastly differing sensitivities to the materials' atomic constituents. The main diffraction peaks in the UC sample are systematically lower in *Q*-space than the analogue peaks in the pattern of the UN sample indicating a larger unit cell, in agreement with literature data [66]. However, the patterns of both samples do exhibit additional, lower intensity, peaks that are not indexed by the rocksalt phase. The pattern collected from the uranium carbide kernel (Figure 16 A & B) exhibits secondary peaks indexed with tetragonal space group *I*4/*mmm*, consistent with a uranium dicarbide (UC_2,) phase (marked by red asterisks in Figure 16 A & B).

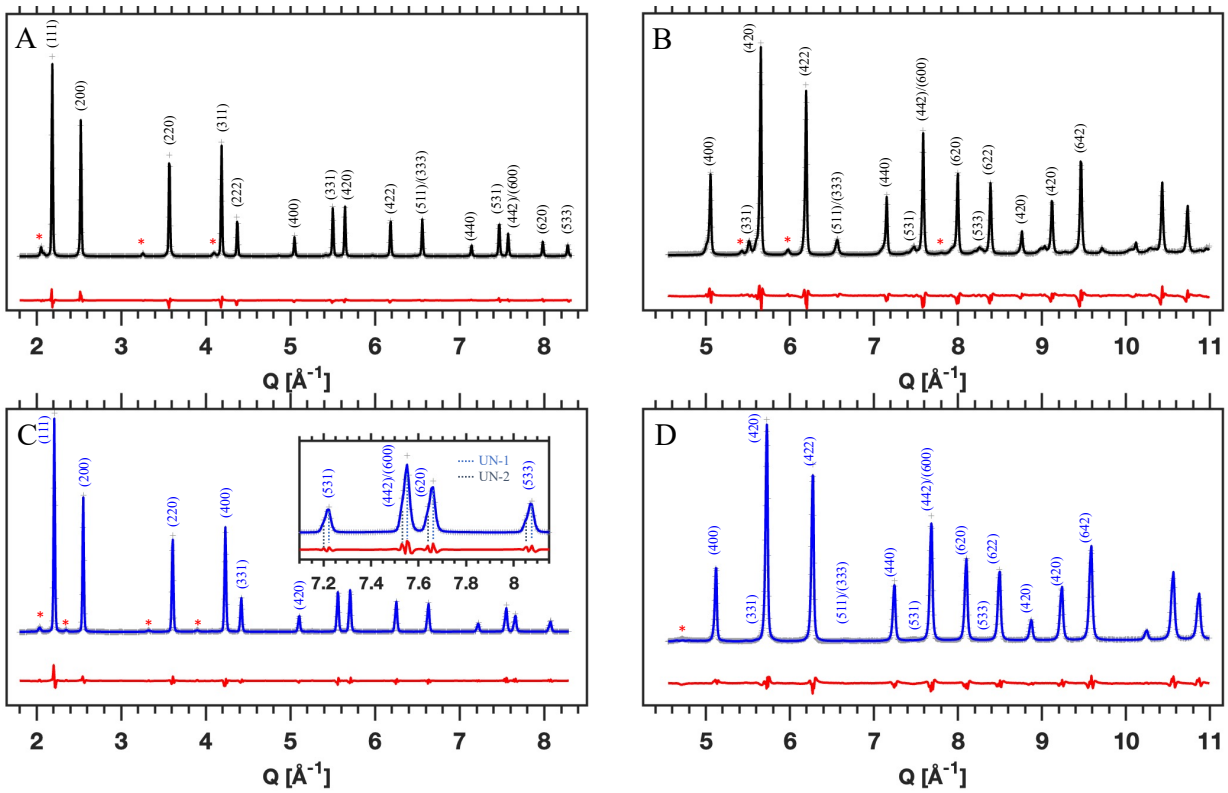

Figure 16. As shown black curve indicating fitted uranium carbide, blue curve fitted uranium nitride, grey markers indicated measurement data, red curve indicates difference curve between fitted and observed data. Selected (hkl) indices provided for primary phase, red asterisks indicate minority phase(s). (A) uranium carbide & (C) uranium nitride XRD results from NSLSii measurements, inset shown to highlight high Q range for UN XRD. (B) uranium carbide & (D) uranium nitride neutron diffraction results from SNS measurements.

For uranium nitride, peaks consistent with cubic space group *Ia*-3, relate to a sesquinitride (α - U_2N_3,) phase (marked by red asterisks in Figures 16 C & D) are present. No additional (uncorrelated) peaks were apparent that would relate to any other impurity phases (*e.g.*, UO_2).

Rietveld refinement results confirm that the uranium carbide sample is best modelled by two crystalline phases, the major rocksalt monocarbide phase and a minor tetragonal dicarbide phase. A summary of the refinement results for uranium carbide is provided in Table 3. The fraction of UC and UC_2 phases differs significantly between X-ray and neutron analysis by about 13 wt.%. This can be correlated to the increased sensitivity of neutrons to low-*Z* elements (here carbon) as compared with X-rays; thus, this demonstrates that neutron diffraction can provide a much more robust phase analysis of uranium carbide materials. Specifically, peaks correlated to UC_2 lattice planes with relatively high carbon occupancy appear significantly more intense in neutron diffraction rather than XRD where the uranium dominant planes vastly overshadow all other peaks. There is also the added benefit with the NOMAD instrument from having well positioned banks that capture a more complete range of scattered particles compared to a single 2D image plate detector. The unit-cell parameters of UC and UC_2 are in agreement to previously reported values, a = 4.96 Å for UC and a = 3.52, c = 6.00 Å for UC_2, and are comparable among refinements of XRD and neutron diffraction patterns (Table 3) [75], [76]. Both analytical probes suggest that the uranium carbide rocksalt phase is within uncertainties fully stoichiometric.

Close inspection of the diffraction peaks related to the uranium nitride rocksalt phase reveals some level of peak asymmetry, skewed towards lower *Q*-values in both neutron and X-ray diffraction patterns, with the latter having much more pronounced intensity, see figure 16C. This asymmetry is consistent with another rock-salt phase exhibiting a larger unit cell parameter.

Table 3. UC Rietveld data, results given for both XRD and neutron diffraction with related errors. * Indicates that these results were selected from bank 5, optimized for highest resolution at high scattering angles.

Uranium Carbide		
Refinement parameter	X-ray (R_w = 9.58 %)	Neutron (R_w = 11.2 %)
Rock-salt (UC) [wt. %]	93.0 ± 0.1	80.1 ± 0.4 *
Secondary phase (UC_2) [wt. %]	7.0 ± 0.1	19.9 ± 0.4 *
UCP rock-salt phase [Å]	4.9600 ± 0.0002	4.95934 ± 0.00006
UCPs UC_2 phase [Å]	A = 3.5378 ± 0.0006 C = 6.004 ± 0.002	A = 3.5381 ± 0.0005 C = 5.9926 ± 0.0009
C-site Z position (UC_2 phase)	Z = 0.47 ± 0.03	Z = 0.39 ± 0.01
C-site occupancy (rock-salt phase)	1.0 ± 0.1	0.98 ± 0.02

Table 4. UN Rietveld data, results given for both XRD and neutron diffraction with related errors. * Indicates that these results were selected from bank 5, optimized for highest resolution at high scattering angles.

Uranium Nitride		
Refinement parameter	X-ray (R_w = 10.8 %)	Neutron (R_w = 10.2 %)
Rock-salt (UN-1) [wt. %]	67.4 ± 0.6	69.6 ± 0.7 *
Rock-salt (UN-2) [wt. %]	28.5 ± 0.6	25.8 ± 0.7 *
Secondary phase (U_2N_3) [wt. %]	4.0 ± 0.1	4.6 ± 0.4 *
UCP UN-1 phase [Å]	4.9036 ± 0.0001	4.90097 ± 0.00009
UCP UN-2 phase [Å]	4.9168 ± 0.0002	4.9111 ± 0.0002
ΔUCP (UN-2 – UN-1) [Å]	0.0132 ± 0.0003	0.0101 ± 0.0003
UCP U_2N_3 phase [Å]	10.650 ± 0.002	10.62 ± 0.01
U2-site X position (U_2N_3 phase)	X = -0.02 ± 0.03	X = 0.00 ± 0.01
N1-site X, Y, Z positions (U_2N_3 phase)	X = 0.4 ± 0.1 Y = 0.2 ± 0.1 Z = 0.4 ± 0.1	X = 0.36 ± 0.05 Y = 0.15 ± 0.05 Z = 0.39 ± 0.05
N-site occupancy (UN-1 phase)	0.83 ± 0.07	0.94 ± 0.03

For uranium nitride, Rietveld refinement of X-ray and neutron diffraction patterns provided good agreement with the data using ~96 wt.% UN rocksalt and ~4 wt.% alpha sesquinitride (α-U_2N_3). The phase fractions differ also between X-ray and neutron data (Table 4), but much less than for the uranium carbide sample (phase fractions of UC_2 from neutron and X-ray data differed by a factor 2). This can be explained by distinct difference in cation configuration in UN and U_2N_3 which are more readily detectable by X-ray probes. Close inspection of the diffraction peaks related to the UN rocksalt phase reveals some level of peak asymmetry, skewed towards lower *Q*-values in both neutron and X-ray diffraction patterns, with the latter being much more pronounced (Figure 16 (c)). This asymmetry seems to be caused by two sets of shifted peaks that suggests the existence of two distinct rocksalt phases in UN with different unit cell parameters. The implemented two-stage refinement approach improved the goodness-of-fit value and demonstrates that besides the U_2N_3 phase (about 4-5 wt.%), two distinct rocksalt phases are present in the uranium nitride sample. The Rietveld refinement results (summarized in Table 4) are within a few % consistent among X-ray and neutron probes and the phase fractions of the two rocksalt structured phases are about 68% for UN-1 and 27% for UN-2. The unit cell parameter of the U_2N_3 phase is in agreement with reported values in literature [76], but the unit cell parameters of both UN-1 and UN-2 phases are larger than expected for an ideal UN rocksalt structure (4.88 Å) [75]. Rietveld refinement was used to estimate the stoichiometry of both UN phases that is expressed by peak intensity variations. X-ray and neutron data show that both rocksalt phases are slightly hypostoichiometric, U_1N_{1-x}, with a more reliable value from neutron diffraction that is somewhat closer to ideal 1:1 stoichiometry (Table 4). Outputted error values for all refinements were computed as a combination of refinement (processing error) and measurement variance (sample error). Processing error was outputted directly from GSAS-II. Measurement variance was found

by considering a tolerance window of ±10% of the best fits R_w value. For example, if the best fit value resulted in a R_w of 9.58 % then a tolerance threshold, R_w of 10.54 % was established. Each individual refinement parameter (as specified in tables 4 & 5) were then adjusted manually until the threshold was met.

3.3.3 Pair distribution function analysis

Neutron PDF analysis was used to evaluate the structural details of both materials over sub-nanometer (<10 Å) length scales. The PDF is an intuitive representation of the short-range structure as histograms of atomic-atomic distances. The peak position represents the distance between atomic pairs (often several pair correlations are beneath one peak), the area under the peak is related to the coordination number, and the width to the disorder in the system. The neutron PDFs of both UC and UN materials are very similar with a nearly identical distribution of pair correlations across *r*-space (Figure 17). The first four peaks in *r*-space correspond to intra-unit cell pair correlations; for instance, the first peak represents the first nearest neighbor (1NN) metal-carbon correlations (1st dominant peak in figure 17 (a) and (b) around 2.2 Å) and is related by symmetry to half of the unit cell parameter. As expected from diffraction pattern analysis, this peak is shifted to smaller-*r* for UN than UC. The next three peaks are nearest neighbor U-U and C/N-C/N correlations, 2NN U-C/N correlations, and 2NN U-U and C/N-C/N correlations (single unit cell translation distances), respectively. The low-intensity features in the PDF below ~2.0 Å are generally the result of a finite Fourier transform (sometimes referred to as '*termination ripples*' [77]). Notably, in the PDF of uranium carbide a more intense, distinct peak is detectable at ~1.2 Å (Figure 7 (a)), which can be attributed to C-C dimer correlations within the UC_2 structure [18], [76]. Carbon atoms bonded coaxially along the *c*-axis have an interatomic distance of ~1.2 Å.

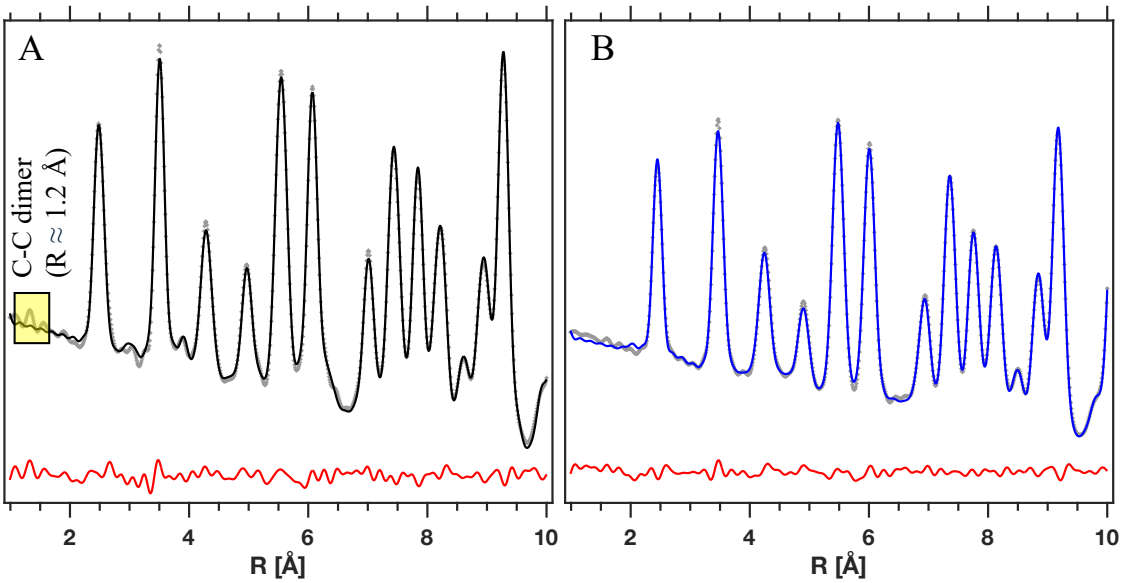

Figure 17. As shown black curve (A) indicating fitted uranium carbide, blue curve (B) fitted uranium nitride, grey markers indicated measurement data, red curve indicates difference curve between fitted and observed data for neutron PDF results from SNS measurements. Yellow box indicates unfitted C-C dimer (correlated distance of 1.2 Å).

Table 5. Tabulated neutron PDF results for uranium carbide and uranium nitride, fitted window from 1 to 10 Å (R-space).

	Uranium Carbide	Uranium Nitride
Refinement parameter	Neutron (SNS) (Rw = 6.30 %)	Neutron (SNS) (Rw = 5.02 %)
Primary phase (rock-salt) [wt. %]	86 ± 1	87 ± 2
Secondary phase [wt. %]	14 ± 1	13 ± 2
Primary phase UCP [Å]	4.9588 ± 0.0006	4.9060 ± 0.0005
Secondary phase UCP(s) [Å]	A = 3.533 ± 0.006, C = 6.02 ± 0.02	10.78 ± 0.06
C/N site occupancy [%] (rock-salt phase)	97 ± 4	79 ± 5

Small box refinement was used to quantitatively analyze the PDFs of both materials. The refinement results were overall consistent with the long-range data, in particular no distinct short-range order or additional impurity phases were detected. As it was the case for the long-range Rietveld refinement, best fit quality was achieved with a mixed UC rocksalt and UC_2 phase (Figure 17A). However, the relatively sharp and intense C-C dimer peak of the UC_2 structure is not captured by the small box modeling, which refines a low-intensity broad peak at ~1.2 Å. This dimer correlated peak offers a strong indication that the two carbon atoms possess a consistent, static bond length that suggests correlated motion, which decreases the peak broadening relative to peaks at larger *r*-values with more stochastic atomic vibrations. This is in contrast to uncorrelated (stochastic thermal) motion which would result in a highly diffuse, unresolvable PDF peak. Unreacted carbon could also contribute to correlations at such low *r*-values; however, this seems unlikely given that most carbon allotropes exhibit C-C correlations larger than ~1.2 Å (between 1.5 - 1.7 Å [78], [79]). Phase fraction analysis based on PDF refinements show that ~86 wt.% of the uranium carbide sample is UC rocksalt and ~14 wt.% UC_2. These phase fractions are somewhat different from neutron diffraction data, but phase fraction generally differ across length scales since, for example, local distortions can affect phase fractions levels determined by PDF analysis. Otherwise, PDF and diffraction data are very consistent, which confirms that the uranium carbide sample is structurally homogeneous across all spatial length scales. The PDF of the uranium nitride system can be well modelled with a UN rocksalt phase plus an additional minor U_2N_3 sesquinitride phase. The phase fractions from PDF refinement differ similarly to the uranium carbide sample from neutron diffraction data. The major UN rocksalt phase was shown with high resolution XRD to consist of two UN rocksalt phases with distinct unit cell parameters (Figure 16 C). Small box modelling with only one rocksalt phase, however, provided the best agreement with

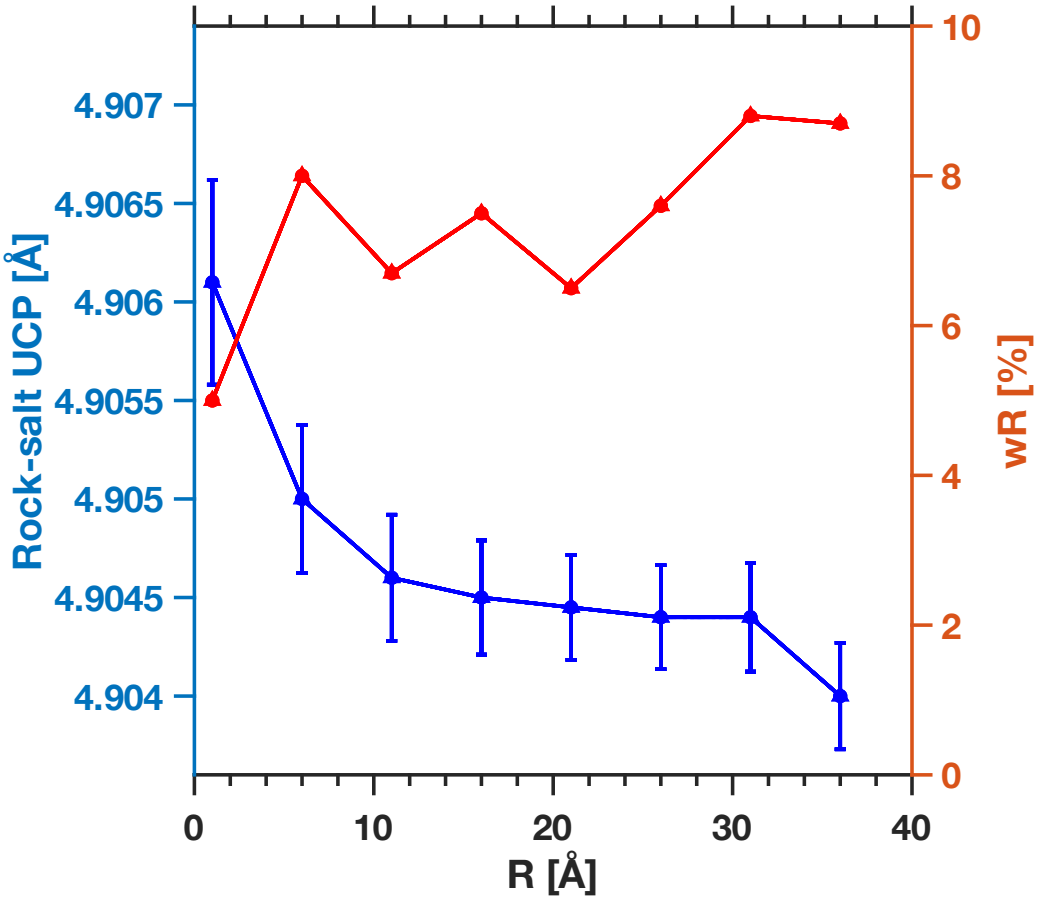

Figure 18. Box-car refinement results for uranium nitride rock-salt phase showing unit cell parameter (left axis) and fit quality (right axis) with respect to sliding real-space R value.

neutron PDF data with a unit cell parameter of 4.9060 ± 0.0006 Å (Table 5); which is close to the weighted average of the unit cell parameters of the two long-range UN-1 and UN-2 rocksalt structures (Table 4). This means that the two rocksalt phases cannot be fully resolved across the short range by small box modeling, which may be indicative of a highly similar local coordination environment of both phases. Finally, X-ray total scattering experiments were performed at NSLS-II which provided with X-ray PDF data. Optimized structural models from neutron PDF analysis were used to analyze the X-ray PDF data of both materials, which showed good agreement (not shown here). Similar to the long-range data, neutron probes are superior in their sensitivity to low-Z elements, which is also expressed in the PDFs. For example, the distinct C-C dimer correlation in the PDF of uranium carbide was not detectable in the corresponding X-ray PDF data.

3.3.3 Thermogravimetric analysis and differential scanning calorimetry

High-temperature calorimetric analysis (TGA/DSC) was performed to get additional insight into the phase behavior of both samples. DSC analysis showed a two-step exothermic reaction for uranium carbide (figure 19) with an onset temperature of the first event at ~300 °C and a peak temperature of ~450 °C. The corresponding temperatures for the second exothermic event are ~450°C and ~590 °C, respectively. This exothermic heat flow is caused by oxidation of the uranium carbide material [80], and the presence of two distinct events correlate may well with the results from structural analysis and the presence of two uranium carbide phases, rocksalt UC and UC_2 [81]. In parallel to the exothermic events, the mass of the sample is increasing based on TGA analysis, with a maximum mass gain of 11.6 ± 0.1 % occurring at 700 °C, a temperature that is higher than peak temperature of the second exothermic event. Upon further heating, TGA data indicates a slight reduction in mass gain to 10.7 ± 0.1 %, up to the highest temperature of 1000 °C. Uranium nitride exhibits much more dramatic exothermic events at comparable temperatures with

much higher heat flows and sharper peaks (Figure 20). The first exotherm has an onset temperature of ~300 °C with the maximum exothermic reaction occurring at ~380 °C. A second distinct exothermic peak follows at ~400 °C with very similar onset and peak temperatures. Several small minor peaks were further detected between 500 and 570 °C. Also, for the uranium nitride sample, the exothermic heat flow is caused by oxidation and the two exothermic events are likely caused by the UN rocksalt and U_2N_3 sesquinitride phases [82]. The TGA curve for UN follows a different trend than for the UC sample, in agreement to previous research [81], [82], reaching a peak mass gain of 14.4 ± 0.1 % at ~500 °C. At higher temperatures, the TGA curve slopes down distinctly up to ~575 °C, which is then followed by a more moderate mass loss (comparable to UC) with increasing temperature reaching 11.1 ± 0.1 % at 1000°C. Over the evaluated temperature regime and ambient atmospheric conditions, both UC and UN materials will oxidize to a final U_3O_8 phase [81], [82]. The results indicate likely oxidation pathways for both materials with the uranium carbide sample following the pathways in equations 11, and 12 and uranium nitride following equations 13 and 14. Subsequent oxidation from UO_2 to U_3O_8 follows equation 15.

$$UC + 2O_{2,(g)} \rightarrow UO_2 + CO_{2,(g)} \quad (11)$$

$$UC_2 + 3O_{2,(g)} \rightarrow UO_2 + 2CO_{2,(g)} \quad (12)$$

$$3UN + O_{2,(g)} \rightarrow U_2N_3 + UO_2 \quad (13)$$

$$U_2N_3 + 2O_{2,(g)} \rightarrow 2UO_2 + 1.5N_{2,(g)} \quad (14)$$

$$3UO_2 + O_{2,(g)} \rightarrow U_3O_8 \quad (15)$$

With each of these individual compounds possessing a standard enthalpy of formation, used to calculate the reaction's overall enthalpy (eq. 16).

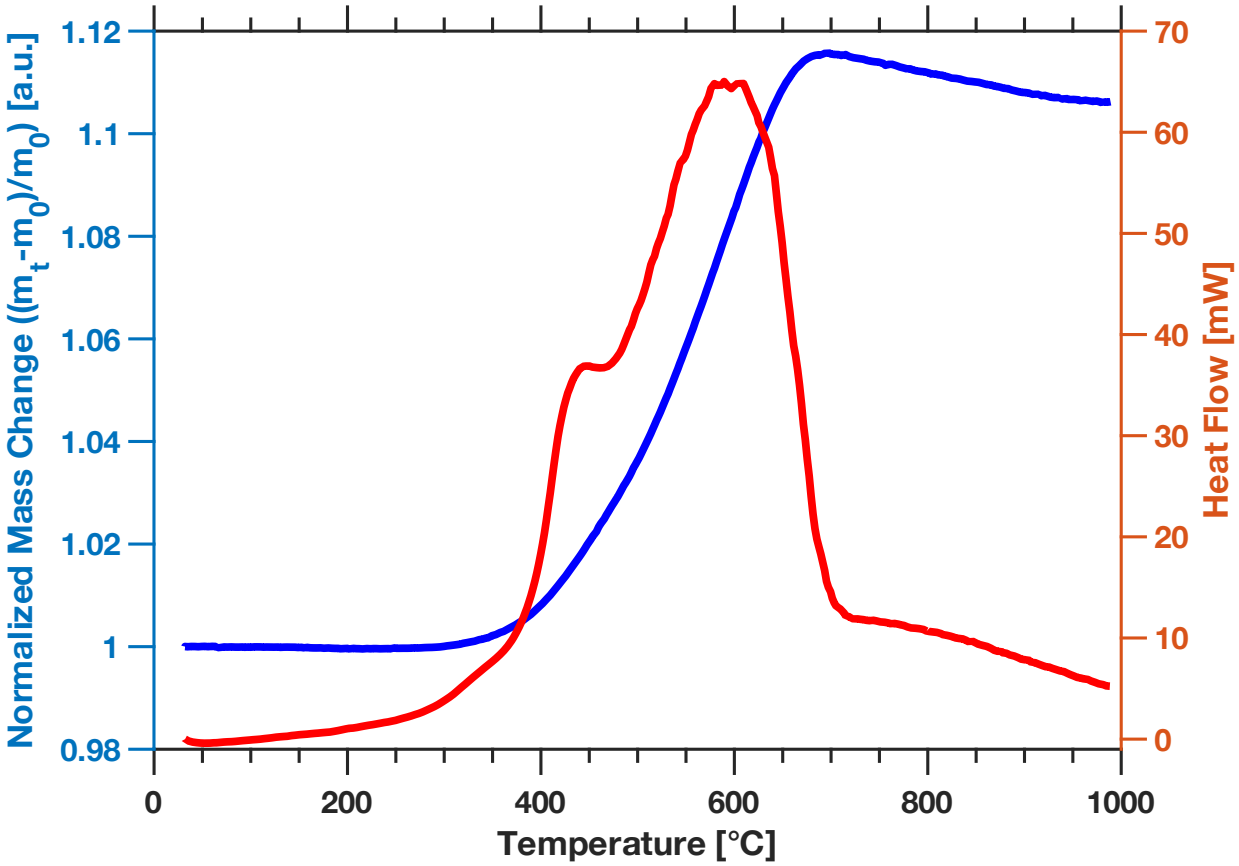

Figure 19. TGA (black curve) and DSC (red curve) thermodynamic results for the uranium carbide sample. Corresponding Y-axes have matching color schemes.

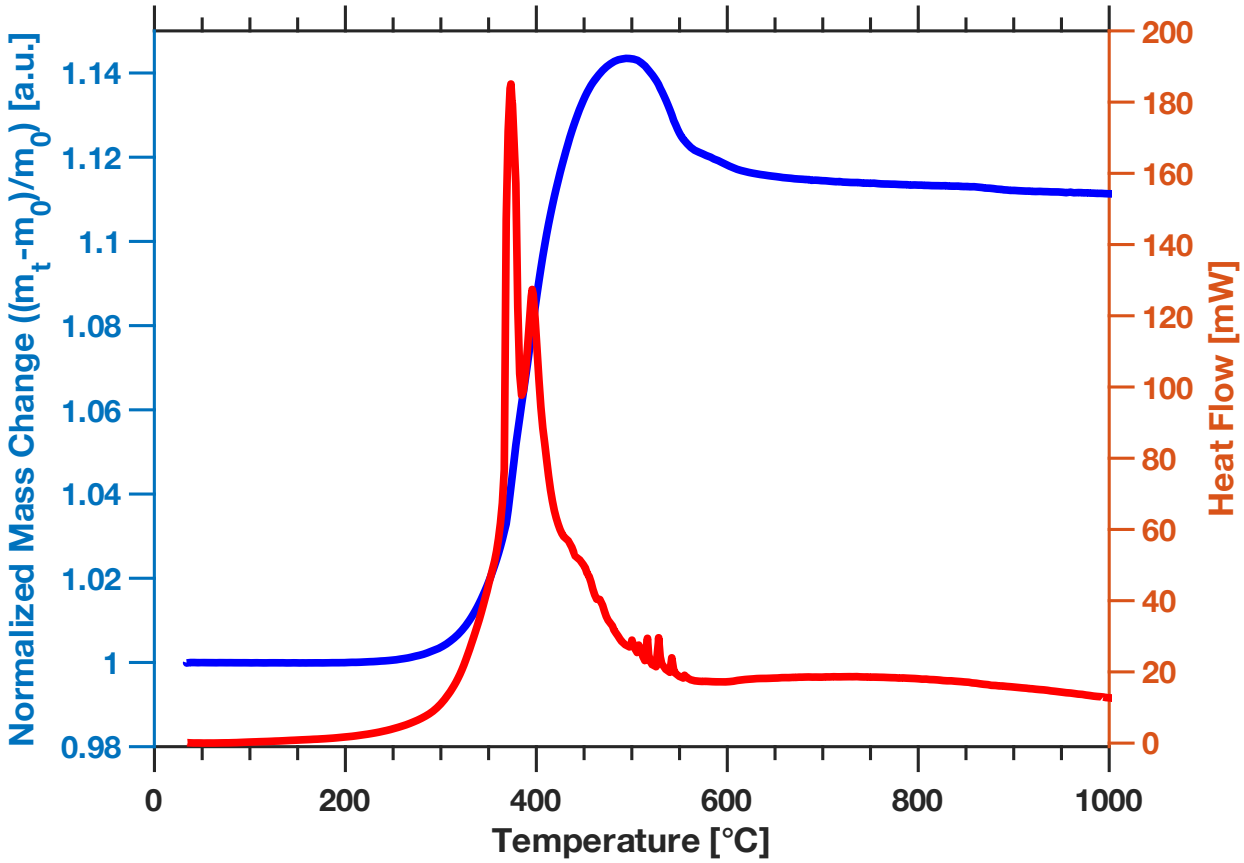

Figure 20. TGA (black curve) and DSC (red curve) thermodynamic results for the uranium nitride sample. Corresponding Y-axes have matching color schemes.

3.5 DISCUSSION

The synthesis of advanced nuclear fuel forms, and in particular uranium carbide and uranium nitride, is a field of intense research. Various synthesis routes have been utilized, including sol-gel, magnetron sputtering of the elemental components, and arc melting [65], [66], [67], [68], [69], [70], [71], [72]. Both magnetron sputtering and arc melting offer high levels of precision for coating thickness and elemental stoichiometry; however, these techniques are limited in their ability to produce high throughput material in a cost-effective manner. For these reasons, the standard technique for commercial grade TRISO fuel production is a sol-gel derived carbothermic reduction (CTR) process as used in this study. With the chosen synthesis conditions, high quality uranium carbide and nitride microspheres were produced with an average diameter between 170 and 180 μm and a grain size on the order of 1 μm. The spheres were regular in shape and size and the internal microstructure dense. Combined X-ray and neutron scattering analysis at large user facilities demonstrated that both materials are predominantly rocksalt structured with only minor secondary phases in each compound. The uranium carbide spheres contained about 20 wt.% of UC_2 and uranium nitride spheres 5 wt.% of U_2N_3. There was no evidence of oxidation in either material, nor was there any notable quantity of unreacted carbon material.

Uranium carbide and nitride materials produced by the sol-gel derived carbothermic reduction (CTR) process has been extensively studied with various techniques. *In situ* neutron diffraction characterization of uranium carbide synthesis was conducted by Reiche *et al*., utilizing precursor uranium oxide and graphite powders loaded within a heated sample crucible. They used a carbon to uranium (C:U) molar ratio of 3.0, lower than the 3.5 used in this study. Similar to the present study rocksalt uranium carbide and tetragonal uranium dicarbide were produced up to temperatures of ~1500°C [69]. The final synthesis product contained up to 97 wt.% UC rocksalt

phase and only 3 wt.%. Other studies [62], [65], [83] reported similar phase compositions and unit cell parameter values, demonstrating a high degree of consistency of the sol-gel synthesis route. Sol-gel synthesized uranium nitride kernels have been also studied in detail, for example by Dunwoody *et al.* [66]. The sample was predominantly UN rocksalt with a minor dicarbide phase impurity. The U_2N_3 sesquinitride phase impurity has been reported as both a synthesis by-produced in the production of UN with various phase fractions and as a stand alone phase [84], [85].

This study provides a complimentary analytical approach to characterize uranium carbide and nitrides synthesized by the sol-gel method. Key is that the same samples were investigated structurally by total scattering experiments with spallation neutron and synchrotron X-ray probes, and thermodynamically by using high temperature calorimetry. This allowed detailed insight into phase composition of both compounds as derived by different techniques. Calorimetric studies independently confirmed the existence of a major and minor phase in each compound. The phase fractions can differ among the different analytical probes as illustrated by uranium carbide, for which phase fractions of the rocksalt UC phase and the tetragonal UC_2 phase differed among X-ray and neutron probes significantly. Based on XRD characterization the phase purity was with 93% UC rocksalt relatively high with only 7% of the impurity UC_2 phase (Table 3). In contrast, neutron diffraction revealed that this material consists of only 80% UC and 20% of UC_2 (Table XXX). This discrepancy can be explained by the very high sensitivity of neutron probes to low-*Z* elements. Neutron assessment is much more reliable for such fuel type materials and it is expected that laboratory-based X-ray characterization have even larger discrepancies than synchrotron-based XRD. This finding is critical, as uncertainty of phase composition leads to uncertainty in performance of these materials, which must be considered. The variation among different probes depend also on the material system and type of impurity phase. For the uranium nitride spheres,

the amount of the minority U_2N_3 sesquinitride phase was more similar among XRD and neutron diffraction (Table 4). In this case, the minority phase is more different with respect to the cation sublattice, which makes X-ray characterization more reliable. Neutron analysis with spallation neutrons is very involved and not feasible for routine phase fraction determination on fuel kernel materials, but it will provide important benchmark data that could be used to calibrate other, more readily accessible techniques. Additionally, it should be noted that C/N-site atomic stoichiometries for both the UC_2 and U_2N_3 impurity phases could not readily be determined through Rietveld refinement due to low phase concentration, it can only be inferred from the Rietveld data that these phases are both likely hypostoichiometric.

One of these techniques is DSC, which demonstrated that each phase in the uranium carbide and nitride spheres exhibits a fingerprint in DSC data as shown by the two heat release events in each material (figures 19 & 20). As it is the case for the structural data, the majority and minority phases are detectable two separated peaks with different areas. The sequence of both peaks is reversed in the carbide and nitride with the UC_2 minority phase preceding the main UC phase, while the peak for U_2N_3 follows the main UN maximum. This behavior can be explained by the oxidation behavior of the different phases. Oxidation of UC_2 occurs at lower temperatures as compared with UC [86], while U_2N_3 functions as an intermediary phase between the UN and UO_2, resulting in a higher oxidation temperature [38]. This behavior can be explained by the distinctively different oxygen activation energies of the primary *versus* impurity phases and the differences in reaction energy, defined by the following equation:

$$\Delta H_{rxn} = \sum \Delta H_f^o{}_{products} - \sum \Delta H_f^o{}_{reactants} \quad (16)$$

Where, $\sum \Delta H_f^o{}_{products}$ is the sum of the product phases standard enthalpy of formation. Likewise for the reactants. The following table summarizes the activation energies and reaction energy for

both uranium carbide and uranium nitride (with both progressing to U_3O_8, table 6). The TGA results for both datasets show some indication of a similar two-stage mass gain (resolved by evaluating the slope of the TGA curve) although it is less clear than with the DSC, offering a complementary confirmation. The area under the heat release peaks depend on the energetics of the oxidation process and one the fraction of the associated phase. Quantitative analysis of the area under each peak and their relative fraction gave for uranium carbide and uranium nitride 80% UC and 20% UC_2 as well as 40% UN and 60% U_2N_3, respectively.

An earlier series of studies by Goncharov, *et al*. also combined (laboratory-based) XRD studies and DSC/TGA analysis on uranium carbide and uranium nitride, prepared by arc melting [81], [82]. The results of these studies found predominantly monophase, rocksalt monocarbide and mononitride, respectively. Calorimetry found that with uranium carbide only a single, broad DSC peak forms with the onset of the exotherm beginning around 500 K [81]. This differs from the author's result with uranium nitride which exhibits a sharp peak doublet, with the first peak starting around 670 K and the second peak centered around 680 K, reaching a modestly higher value [82]. This two peak configuration was suggested as an indication of a two-step oxidation process as described before. Complementary EXAFS was performed in both of these studies as a form of local bonding assessment. Here they found evidence of impurity hyperstoichiometric phases, α-UC_2 in the carbide and both α- and β-U_2N_3 phases in the nitride [81], [82].

High resolution XRD analysis clearly showed that the rocksalt structured UN material consists of two phases with distinct unit cell parameters, none matching the ideal value of pure UN, 4.889 Å (figure 21) [65], [66], [75], [83], [91], [92], [93], [94], [95], [96].

Table 6: Oxidation energetics for relevant uranium carbide and uranium nitride crystallographic phases

Crystallographic phase	**Oxidation activation energy [kJ/mol]**	**Reaction enthalpy [kJ/mol]**
UC	29.7 [80]	-1625 [81], [87], [88]
UC_2	Low [89]	-2025 [81], [87], [88]
UN	30-32 [90]	-2600 [82], [87], [88]
U_2N_3	–	-1995 [82], [87], [88]

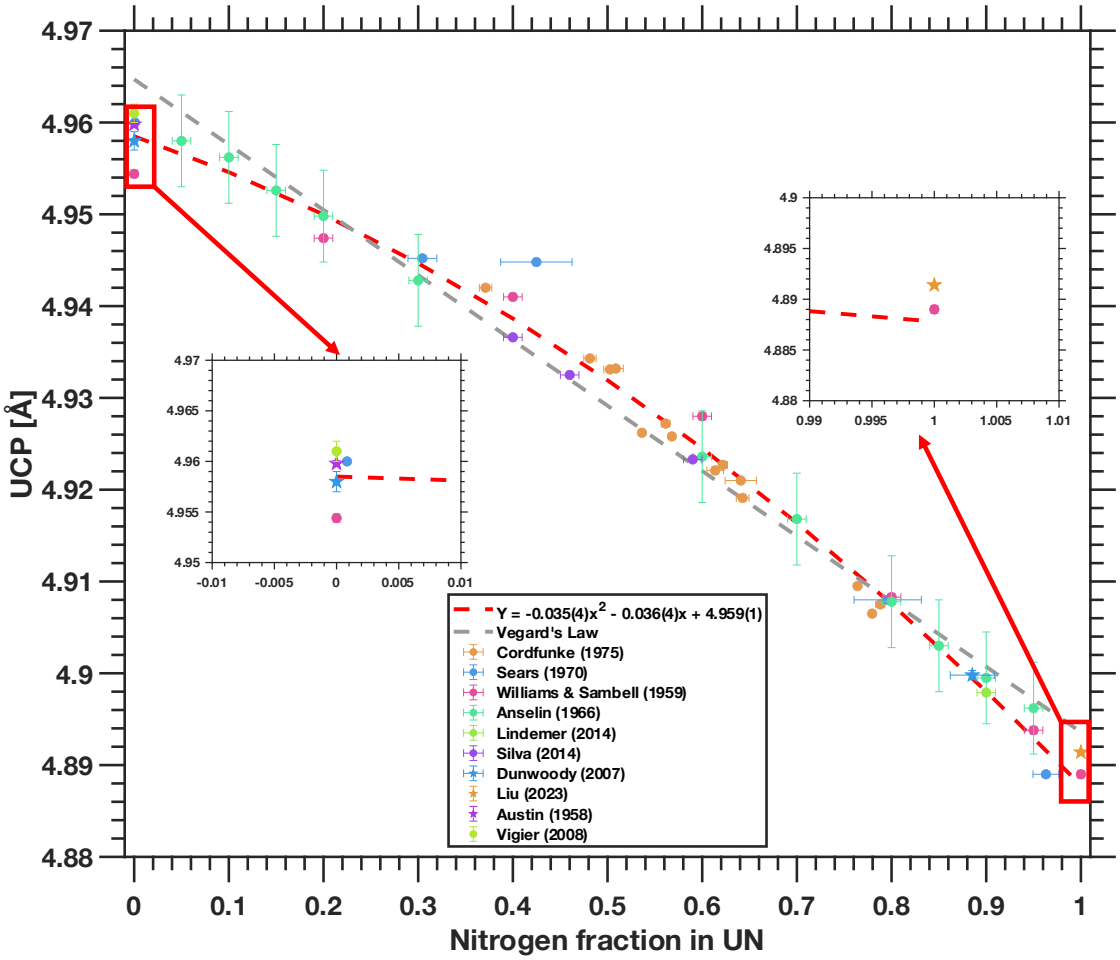

Figure 21. Unit cell correlation plot reproduced from [65], [66], [75], [83], [91], [92], [93], [94], [95], [96], with results of unit cell parameter and fraction of nitrogen lattice sites occupied by N-atoms of the rock-salt uranium nitride. Correlated quadratic with results of unit cell parameter and fraction of nitrogen lattice sites occupied by N-atoms of the rock-salt uranium nitride. Correlated quadratic expression (red dashed line) shown on figure. A linear regression in accordance with Vegard's law is shown (grey dashed line).

The unit cell parameter values from this study are as follows: uranium carbide (unit cell parameter (a) = 4.95934 ± 0.00006 Å), UN-1 (A = 4.90097 ± 0.00009 Å), UN-2 (A = 4.9111 ± 0.0002 Å) all values produced from neutron diffraction measurements. When fit to correlated quadratic trendline (figure 21) the calculated values of the carbon content (as a percentage of overall nitrogen lattice site) are as follows. Using the uranium carbide as a standard (no nitrogen assumed) we can compute the carbon content as 100.3 ± 0.3 %. This suggests that the overall error from fitting to this correlation is ~1 %. Therefore, the UN-1 sample nitrogen content would be 87 ± 1 % and the UN-2 sample would be 76 ± 1 %. With neutron diffraction we are also able to produce detailed assessments of peak intensity which can be directly refined during Rietveld analysis, see table 4. This technique works by considering the neutron scattering length (figure 9), and a series of simple algebraic expressions (eqn. 17 & 18).

$$f_R b_N = f_N b_n + f_C b_c + f_O b_o + f_v b_v \tag{17}$$

$$f_n + f_c + f_o + f_v = 1 \tag{18}$$

Where b_x is the neutron scattering length of the atom species (N = nitrogen, C = carbon, O = oxygen, and V = vacancy) and f_x is the fraction of the atom species '*x*', f_R is the refined site occupancy from table 4. With two equations and four unknown variables we must consider simplifying assumptions *(1) neglect vacant lattice sites*, and *(2) using two distinct binary models, only nitrogen and either carbon or oxygen may be present*. From here, we derive two models, the first is a binary system of carbon and nitrogen where we find a nitrogen content of 85 ± 15 % which is broadly in agreement with unit cell parameter calculation. With the second binary model with oxygen and nitrogen we find nitrogen content of 90 ± 10 %. Further combustion analysis may be relevant to deduce which case is the most likely configuration. Peak intensity fitting works in a similar fashion for the uranium carbide system where only the carbon/oxygen binary system is

relevant. Here, we find carbon content of 85 ± 15 %. From these results it can be concluded that neutron peak assessment may work as a qualitative comparison only given that all values, are broadly in agreement to unit cell correlations and other values produced from literature.

3.6 CONCLUSIONS

On-going investigations into the characteristics of the uranium carbide and nitride systems continue to improve the nuclear fuel industry's understanding of structural and chemical characteristics during kernel production. This study comprehensively evaluates the multi-scale structural phenomenon with both X-ray and neutron total scattering techniques. With both techniques offering critical insight into the uranium and non-metal lattice subsystems. Neutron total scattering results proved to be superior for local scale (sub-nanometer assessments). These results validated the phase compositions of both samples and can be used to improve modeling investigations in future work. This includes proving the correlated motion of the C-C dimer in the uranium carbide system and the phase morphology of the U_2N_3 structure. Long-range diffraction results were best produced with the ultra-high resolution powder synchrotron powder XRD. These results yielded an interesting finding within the uranium nitride system which appears to undergo phase segregation into two separate UC_xN_{1-x} phases. Insight from literature, figure 21, helps to diagnose the compositions of these phases. Further evaluation of the uranium nitride system may be warranted as the sample was synthesized to be intentionally hypostoichiometric and yet, produced a hyperstoichiometric U_2N_3 phase. This suggests that either continued nitridation or potential stabilization for unreacted oxygen. From the provided phase diagrams, figures 4 and 5, we can confirm the presence of the primary expected phases within both systems meaning that this synthesis pathway may be viable for future fuel production.

CHAPTER 4: RADIATION RESPONSE OF TRANSITION METAL CARBIDES TO SHI IRRADIATION

Portions of this chapter were previously published in the Journal of Applied Physics by Jacob A. Minnette, Evan Williams, William F. Cureton, Alexandre Solomon, Eric O'Quinn, Matthew Kurley, Rodney D. Hunt, Changyong Park, Ina Schubert, Christina Trautmann, and Maik Lang. For these works, J.A.M., E.W., W.F.C., M.K., R.D.H., and M.L. conceived experiments; J.A.M., E.W., W.F.C., A.S., E.O., C.P., I.S., C.T. and M.L. prepared relevant samples and performed formal analysis; J.A.M. drafted the manuscript with input from all co-authors.

The following chapter involves first of its kind SHI irradiation studies on transition metal carbides. This work was done to address the knowledge gap with highly ionizing radiation to highly resilient structures. To accomplish this objective, we must address the following open questions:

1. What is the response mechanism of TMCs (*e.g.*, ZrC) to SHI irradiation?
2. How does this response mechanism compare to other materials?
3. What role does grain size have on the impact of the irradiation response?

4.1 ABSTRACT

Zirconium carbide (ZrC) is commonly used for energy sector research, as well as a surrogate for the proposed advanced nuclear fuel candidate uranium carbide. This study investigates structural modifications to nanocrystalline and microcrystalline ZrC resulting from dense electronic excitations induced by swift heavy ion exposure. Samples were irradiated with 946 MeV Au ions to various fluences up to 6×10^{13} ions cm^{-2} and characterized using synchrotron-based x-ray diffraction. The evolution of the unit-cell parameter and heterogeneous microstrain were evaluated as a function of fluence and compared with those of nanocrystalline and microcrystalline CeO_2 (a surrogate for UO_2 fuel) irradiated under identical conditions. Distinct differences were observed in the radiation responses of the carbide and oxide across both grain

sizes. Most notably, microcrystalline ZrC exhibits swelling characterized by two distinct regimes, which does not result in saturation at the ion fluences achieved. This contrasts with CeO_2, which exhibits the well-documented direct-impact defect accumulation mechanism, reaching a steady-state saturation of swelling at higher fluences. Nanocrystalline CeO_2 undergoes more pronounced swelling compared with microcrystalline CeO_2, in contrast to nanocrystalline ZrC, which exhibits only minimal unit-cell changes. These results demonstrate that swift heavy ion-induced structural changes can be quite different in carbides and oxides, which must be considered when extrapolating fission-fragment type damage in current fuels to advanced fuels.

4.2 INTRODUCTION

A major obstacle to the development of next generation nuclear reactors is the fabrication of fuel forms that are not only radiation tolerant but also exhibit outstanding mechanical and thermal properties under operating conditions. Currently, the most widely used fuel form in nuclear reactors is uranium dioxide (UO_2) [97], which falls within a broad group of materials that exhibit the fluorite structure (*Fm-3m*) as shown in Fig. 22*a*. While these materials often offer impressive radiation tolerance, they tend to exhibit low fracture resistance and thermal conductivity [98], [99], [100]. Advanced reactors, such as high-temperature gas-cooled reactors, usually operate at elevated temperatures compared to current generation reactors; as such, advanced fuel forms require enhanced thermal properties relative to UO_2 [101]. One such proposed alternative fuel candidate for use in generation IV reactors is rocksalt-structured (*Fm-3m*) uranium carbide (UC), shown in Fig. 22*b*. UC has a high thermal conductivity, which minimizes fuel-related accident scenarios and increases the possible reactor operating temperature [18], [102]. However, a major drawback of carbide fuel forms is their lower radiation tolerance, characterized by a more drastic

volumetric swelling under prolonged in-reactor irradiation at elevated temperatures when compared with conventional oxide fuels [103], [104].

Characterizing nuclear fuel performance under irradiation is essential, as damage induced by neutrons and fission fragments can dictate the lifetime of the fuel. Fission fragments, which fall within the broader category of radiation known as *swift heavy ions* (SHIs) [44], share the majority of the energy released in the fission reaction (typically on the order of 70–100 MeV per fission fragment). Such high-energy projectiles interact with matter through electronic excitations and ionization in the target material (electronic energy loss), which differs from the interaction mechanism of neutrons and low-energy ions (nuclear energy loss). Coulombic interactions with the electrons of the target atoms transfer the energy from the projectile to the electronic subsystem, which couples to the atomic subsystem through electron-phonon interactions [44]. In many insulators, the resulting rapid heating and quenching process along the ion trajectory leads to the formation of an *ion track*, a cylindrical region of 5–10 nm diameter with length of tens of μm [44]. Within an ion track, the irradiated material often undergoes chemical and structural modifications that can lead to simple and complex defect formation as well as phase transformations, which are correlated to both unit-cell swelling and microstrain buildup [44]. It is only near the end of the ion range (Fig. 2) where direct displacements through knock-on, ballistic collisions with target atoms dominate, similar to those induced by neutrons and low-energy ions (keV range). While the majority of the displacement dose (expressed as displacements per atom, dpa) is a result of such ballistic collisions, the intense ionization processes occurring within the electronic energy loss regime are the dominant energy deposition mechanism along the majority of the ion track.

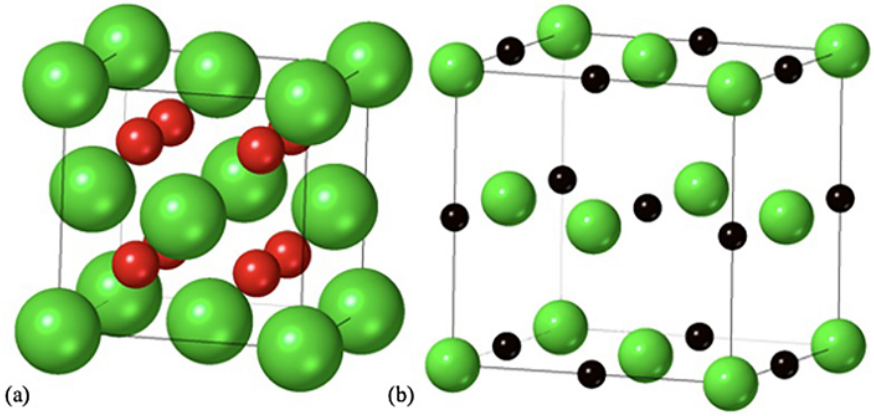

Figure 22. (a) Fluorite UO_2 and (b) rocksalt UC atomic arrangements. Uranium atoms are displayed as green spheres in both figures, oxygen as red, and carbon as black. Respectively isostructural to the two materials used in this study: (a) CeO_2 and (b) ZrC.

The current understanding of ionization-induced radiation effects in nuclear fuel is incomplete, and even less is known for advanced fuel forms such as UC, despite that it is essential for better modeling of fuel swelling and gas particle transport (*e.g.*, fission off-gas) [17], [105].

In this study we examine effects across varying crystalline size domains. A previous study found a significant influence of grain size on the associated materials' performance in engineering applications [106]. In general, many nanocrystalline materials, relative to their microcrystalline counterparts, possess superior mechanical properties (*e.g.*, increased strength and ductility) that are highly desirable in energy production technologies [107]. For neutron and low-energy ion irradiated samples, multiple studies have suggested that nanocrystalline ceramics are more tolerant of radiation-induced degradation effects compared with bulk materials (*e.g.*, reduced swelling) [108], [109], [110]. This is related to the increased surface area relative to the volume of grains, which enables enhanced annealing of radiation-induced defects [111].

Given the complexity of handling radionuclides, it is common to simulate the response of actinide-bearing materials under irradiation using nonradioactive isostructural analogue materials. In place of UO_2, the commonly used surrogate in the nuclear energy community is cerium dioxide (CeO_2) [112], which has been extensively studied under different irradiation conditions (*e.g.*, swift and low-energy ions, neutrons) [40], [113], [114]. While details of defect formation differ between CeO_2 and UO_2 both materials are highly tolerant to SHI irradiation [17]. Defects have been shown to form along the ion trajectories that lead to unit-cell expansion and heterogeneous microstrain [17], [115]. At high irradiation fluences, when individual tracks overlap, both unit-cell expansion and heterogeneous microstrain saturate. Such behavior is best described by a direct-impact model which considers that each individual swift heavy ion produces a cylindrical nanoscopic track with a modified structure. Ion fluence accumulation results in track overlap, which progressively

reduces additional damage and leads to a steady-sta14te behavior, characterized by simultaneous defect production and annealing. In the initial stage of irradiation (isolated tracks), the observed structural modifications increase linearly. At higher fluences, this is followed by a sublinear trend (overlapping tracks), and saturation finally occurs when the sample is completely covered with tracks. This is described by a Poisson exponential evolution and is a typical indicator of a direct-impact process. From the evolution of the unit-cell parameter, a, as a function of fluence, ϕ, the damage cross section, σ, can be extracted from an exponential fit to the data using the Poisson equation (19) [45]:

$$\frac{\Delta a}{a_0} = \frac{a(\phi)-a_0}{a_0} = \frac{a_{sat}-a_0}{a_0}\left(1 - e^{-\sigma\phi}\right). \quad (19)$$

Poisson-type damage accumulation is consistently observed for CeO_2 independently of whether the irradiation is performed with SHIs or low-energy ions [116]. Exposure to SHIs was shown to induce redox changes in CeO_2 ($Ce^{4+} \rightarrow Ce^{3+}$) that account for some of the observed unit-cell swelling and microstrain [117]. Such redox changes are critically dependent on the cations' accessible oxidation states in oxides, which explains the different responses that were observed under SHI irradiation in CeO_2 (Ce^{3+} and Ce^{4+}), UO_2 (U^{4+}, U^{5+}, and U^{6+}), and ThO_2 (Th^{4+}) [40].

For carbide fuel forms, zirconium carbide (ZrC) is utilized as a non-radioactive analogue for uranium carbide and exhibits the same rocksalt crystal structure as UC. In general, radiation effects in carbides have been studied to a lesser extent than oxides, and ZrC has so far only been investigated using low-energy ions within the nuclear stopping regime [118], [119]. In such studies it was found that swelling evolves similarly as for CeO_2 following a direct-impact process. As SHIs predominantly interact with target electrons, however, the respective responses to ionizing radiation may differ between these materials due to the different character of atomic bonding: mostly ionic in CeO_2 *versus* mostly covalent in ZrC [120], [121]. In this study, we investigate the

responses of microcrystalline and nanocrystalline ZrC under irradiation by 946 MeV Au ions. The irradiated samples are characterized using synchrotron-based XRD. Unit-cell expansion and microstrain are determined, and the fluence-dependent behavior is compared with that of microcrystalline and nanocrystalline CeO_2 irradiated under identical conditions.

4.3 RESULTS

The following section summarizes the experimental findings, as well as the results from the processed data as collected. All data were collected, processed, and refined using the techniques described previously in *chapter 2*.

4.3.1 Microcrystalline samples

Analysis of XRD patterns reveals that all ZrC samples (labeled from table 1: PVD1, SG1, SG2) exhibit the rocksalt structure prior to irradiation with no discernible impurity phases (Figure 23*a* shows the XRD pattern of the PVD1 sample). Rietveld refinement of the PVD1 sample yields an initial unit-cell parameter of 4.70 ± 0.01 Å with stoichiometry of $ZrC_{0.96\pm0.01}$; respective values for the sol-gel samples (SG1 and SG2) are 4.70 ± 0.01 Å and $ZrC_{0.98\pm0.02}$. Vacant carbon site fractions within the ZrC samples were determined by comparing the relative peak maxima from XRD data. The synthesis of ZrC with a hypostoichiometric anion sublattice agrees well with previous reported data that utilized synchrotron ZRD and neutron scattering diffraction data [16], [118]. No amorphization is evident in ZrC after ion irradiation to the maximum fluence (6×10^{13} ions cm^{-2}), and no new diffraction maxima emerge. All Bragg peaks are retained but shift to lower values of 2θ with increasing fluence [Fig. 23(b)], indicative of an ion-induced expansion of the unit cell.

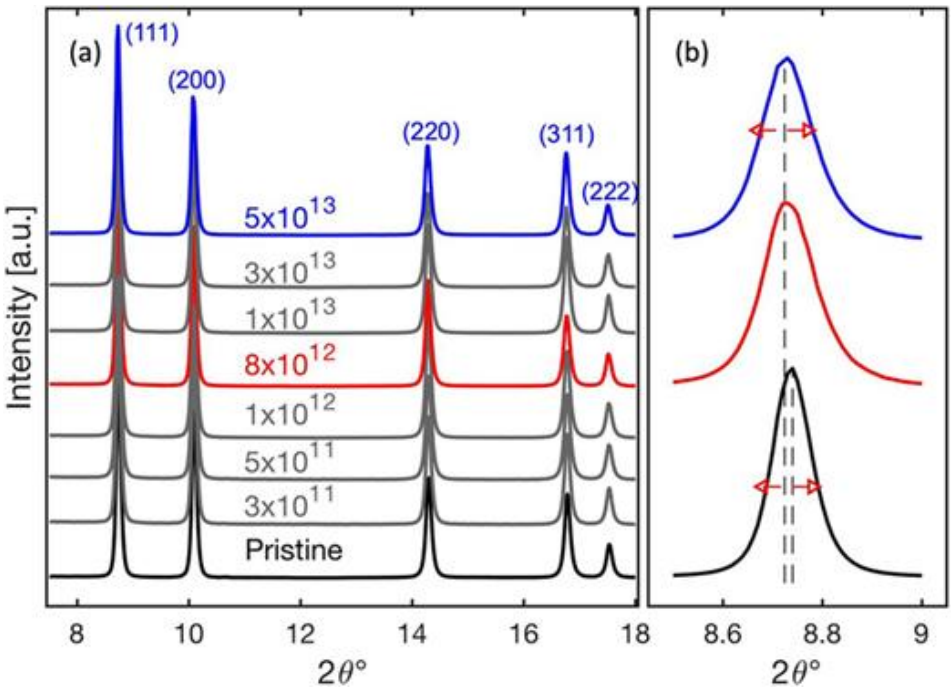

Figure 23. (a) Stacked synchrotron XRD patterns of microcrystalline PVD1 ZrC (400–1200 nm grain size) with normalized intensity, pristine and irradiated with 946 MeV Au ions of increasing fluence (given in ions cm−2). (b) enlarged view of (111) diffraction peak, to display peak shift (dashed black vertical line) and broadening (red horizontal arrows).

The FWHM of the peaks also increases with fluence [Fig. 23(b)], which can be explained either by a reduced grain size or by an accumulation of microstrain. Qualitatively, this radiation response agrees with that of micro-CeO_2 irradiated under identical conditions in this study (not shown) and previously reported [17].

Rietveld refinement of XRD patterns reveals that the unit-cell parameters of all microcrystalline ZrC samples (PVD1, SG1, and SG2) initially increase linearly with ion fluence before saturating at a relative swelling of ~0.03% [Fig. 4(a)]. This behavior is best described by the direct-impact model [Eq. (13)], indicating that defects in ZrC are created within individual ion tracks and reach a steady-state when tracks overlap. Saturation is observed at a fluence of approximately 8×10^{11} ions cm^{-2}, which corresponds to a damage cross section of $\sigma = 95 \pm 5$ nm^2 and a track diameter of 11 ± 2 nm, assuming cylindrical track geometry. Upon further irradiation spanning more than one order of magnitude ($\sim 1 \times 10^{13}$ ions cm^{-2}), the saturation of the unit-cell expansion is maintained within the uncertainties. At higher fluences, however, the unit cell starts to further expand linearly, reaching 0.11 ± 0.01% for SG2 at the maximum fluence tested (6×10^{13} ions cm^{-2}). This second defect accumulation process at higher fluences was consistently observed [Fig. 24(a)] for two types of ZrC samples irradiated during the same beamtime (PVD1 and SG1), as well as across two independent ion irradiation experiments (SG1 and SG2). Under swift heavy ion irradiation, defect accumulation proceeds in ZrC by a distinct two-step mechanism: direct-impact behavior, for which swelling saturates, followed by a second linear swelling regime with no apparent saturation.

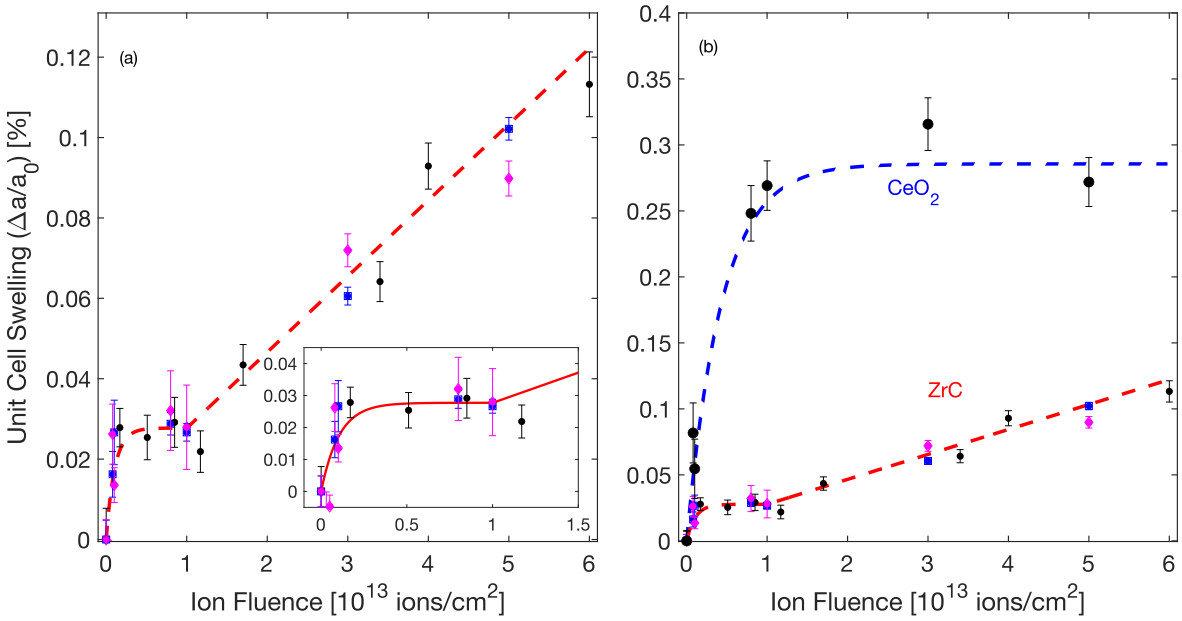

Figure 24. Unit-cell expansion determined by Rietveld refinement of XRD patterns as a function of ion fluence for microcrystalline ZrC and CeO2. (a) Different ZrC samples were irradiated during two beamtimes under the same conditions with 946 MeV Au ions (blue PVPVD1, magenta SG1, black SG2; see table for sample labeling). The inset highlights unit-cell expansion in the direct-impact regime (fluences up to ~1.0×10^{13} ions cm^{-2}). (b) CeO_2 unit-cell expansion compared with ZrC from (a). The error bars represent uncertainties from Rietveld refinements. The dashed lines suggest trends to guide the eye).

In clear contrast, CeO_2, Fig. 24 B, does not exhibit the second swelling mechanism, and the fluence-dependent unit-cell parameter changes are completely described by a direct-impact behavior. Saturation of unit-cell expansion is observed at a higher fluence as compared with ZrC ($\sim 1.5 \times 10^{13}$ ions cm^{-2}), and the corresponding track diameter in CeO_2 is 6 ± 1 nm, which is about half of the value observed in ZrC. Relative swelling of CeO_2 at the maximum fluence is $0.27 \pm 0.02\%$, which is approximately 2.4 times higher than the relative swelling of ZrC observed at the maximum fluence point. The irradiation behavior of CeO_2 agrees well with previous results obtained under the same ion-beam conditions [40], [117]. The microstrain evolution of micro-CeO_2 shows a similar trend as the unit-cell expansion [Fig. 24(b)], with maximum microstrain levels of $0.32 \pm 0.03\%$ at a fluence of 5×10^{13} ions cm^{-2}, with a calculated cross-section diameter of 14 ± 2 nm.

The microstrain of unirradiated ZrC (PVD1) is $0.22 \pm 0.01\%$, which is approximately six-fold more than that observed for unirradiated CeO_2 with a value of $0.035 \pm 0.008\%$. The initial microstrain of the sol-gel synthesized ZrC (SG1/SG2, not shown) is about one order of magnitude lower than the PVD1 sample, as shown in previous studies [16], [122]. Williamson–Hall analysis revealed that peak broadening in ZrC with increasing fluence is primarily due to a buildup of microstrain. No irradiation-induced fragmentation is observed and, instead, the domain size appears to increase to a minor degree (Fig. 25 C). The overall coherent domain size of the PVD1 ZrC pristine sample based on XRD measurements, 68 ± 2 [Å], is considerably smaller than the reported mean grain size of 400-1200 [nm], in agreement with electron microscopy conducted in a prior study [16].

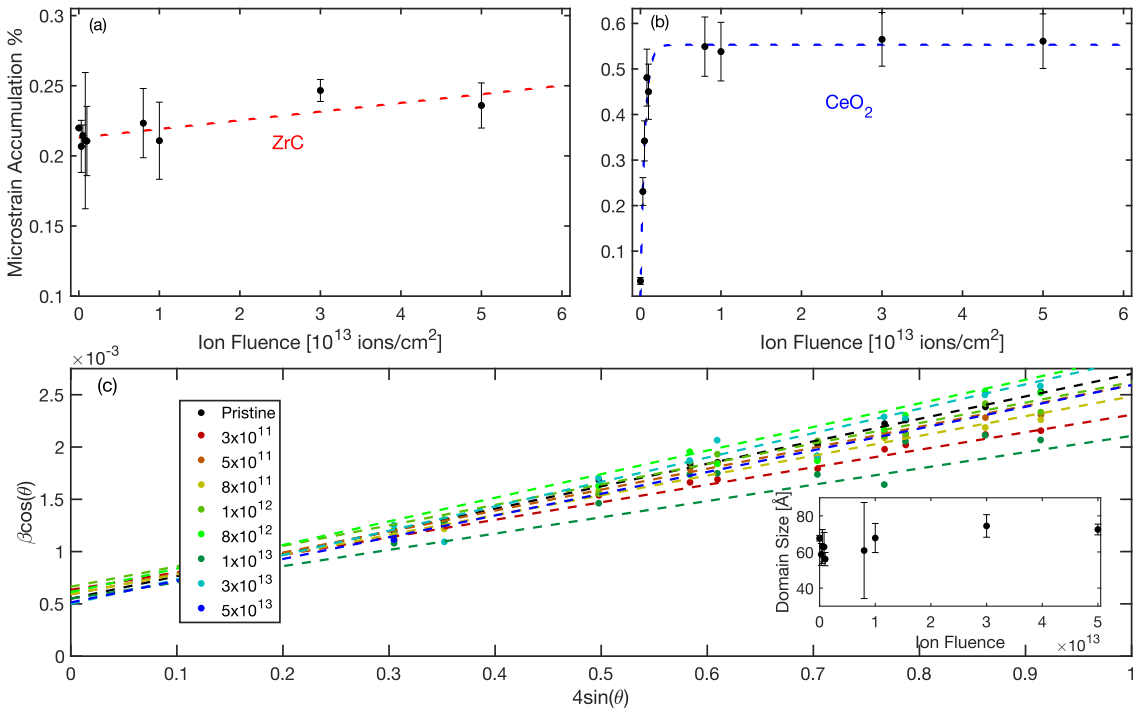

Figure 25. Microstrain accumulation for (a) microcrystalline ZrC, red line is a suggested guide to the eye, and (b) microcrystalline CeO2 both synthesized via the PVD method as a function of increasing ion fluence, the blue line shows Poisson fit of direct impact trend, as determined by Williamson-Hall plots. (c) Coherent domain size as determined with Williamson-Hall analysis for PVD1 ZrC. Error bars represent uncertainties from Williamson-Hall analysis.

Although the trend is less clear, the non-saturating nature of the microstrain accumulation may suggest that a mechanism similar to the unit-cell expansion is occurring [Fig. 24(a)]. In either case, despite the lower initial microstrain in unirradiated CeO_2, the accumulated microstrain after irradiation to the maximum fluence is more than a factor of 2 higher than that of ZrC (PVD1) (Fig. 24, $0.56 \pm 0.06\%$ vs $0.24 \pm 0.02\%$).

4.3.2 Nanocrystalline samples

The synchrotron XRD pattern of pristine nanocrystalline ZrC (PVD2) with a nominal reported grain size of 20 nm is unambiguously indexed with the pure rocksalt structure with no detectable impurities, particularly any oxide phases. The unit-cell parameter was determined to be 4.68 ± 0.01 Å with a sample stoichiometry of $ZrC_{0.93\pm0.01}$. The diffraction peaks shift and broaden with increasing fluence (Fig. 26). However, in contrast to the systematic peak shift to smaller 2θ values with increasing fluence and accompanied peak broadening in the case of microcrystalline ZrC, the XRD patterns of the nanomaterial reveal a more scattered peak shift to smaller and larger 2θ values along with varied broadening. Refinement of the XRD patterns suggests, but does not conclusively indicate, minor unit-cell contraction in nanocrystalline ZrC as a result of irradiation (Fig. 26). The origin of this behavior remains unclear, but the inconsistent trend may be a result of minor oxidation and formation of a ZrO_2 impurity phase as fluence increases. However, this process seems to be highly heterogenous, as measurements of several sample platelets irradiated to the same fluence (e.g., for 3×10^{13} ions cm^{-2}) exhibit a large variation in the relative unit-cell size (e.g., between −0.039% and −0.104% for 3×10^{13} ions cm^{-2}). The formation of ZrO_2 is evident in some of the XRD patterns above a fluence of 5×10^{11} ions cm^{-2} at a 2θ value of ~8 degrees (Fig. 26).

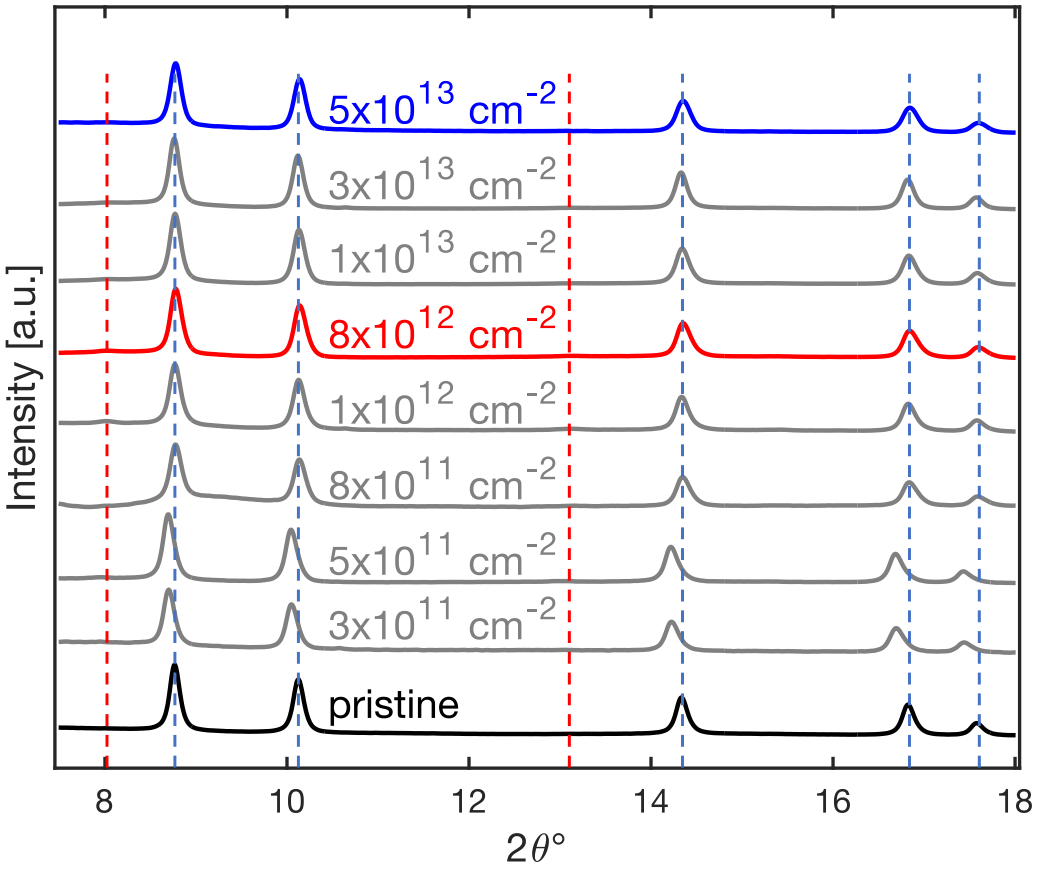

Figure 26. Stacked XRD patterns of nanocrystalline ZrC (20 nm grain size, PVD2) before and after irradiation with 946 MeV Au ions of increasing fluence (given in ions cm−2), with normalized intensity. The vertical dashed lines indicate ZrO2 (tetragonal) peak locations.

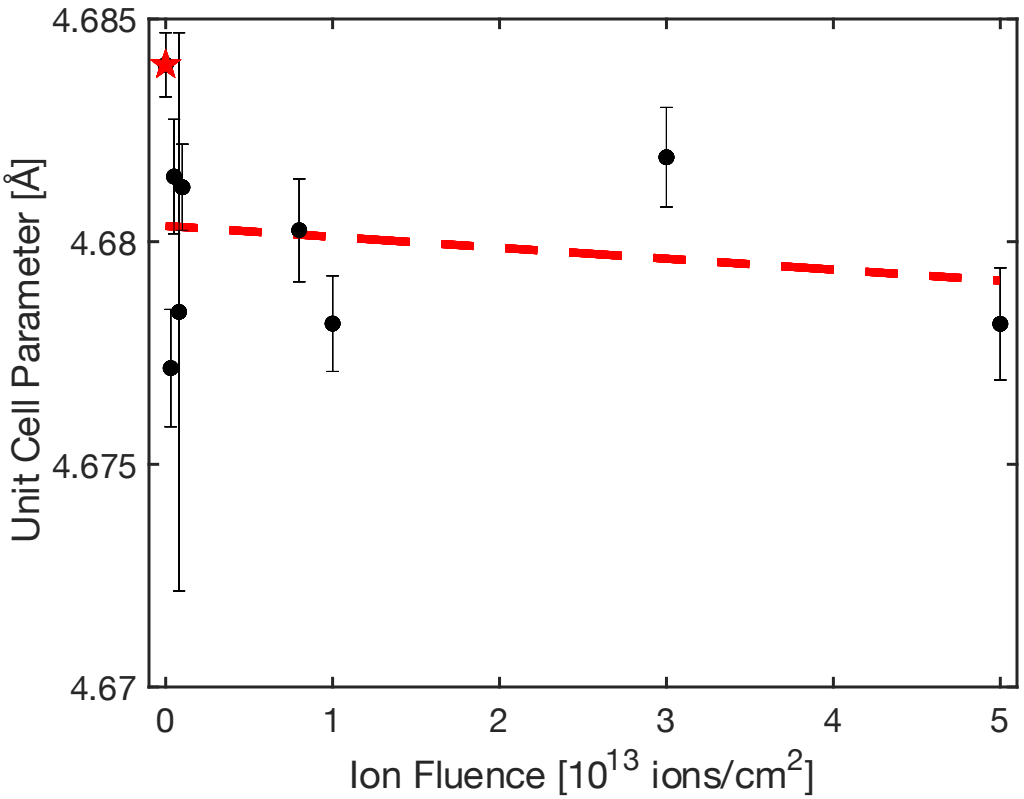

Figure 27. Evolution of a unit-cell parameter in nanocrystalline ZrC as a function of ion fluence, determined by Rietveld refinement of XRD patterns. The red dashed line, produced from linear regression of average value of unit-cell parameter, serves to guide the eye. The error bars represent uncertainties from Rietveld refinements. The red star indicates unirradiated sample with a unit-cell parameter value of 4.68 ± 0.01 Å.

Rietveld refinement of the XRD patterns of irradiated nano-ZrC was used to determine the degree of oxidation as a weight fraction. The results show some variation with ion fluence (maximum ZrO_2 fraction of 11 ± 1 wt. % at 1×10^{12} ions cm^{-2}). The presence of ZrO_2 suggests that nanocrystalline ZrC undergoes some degree of oxidation either during irradiation or after irradiation. Rietveld refinement showed that both the tetragonal and the cubic high-temperature ZrO_2 phases provide a good fit to the diffraction peaks of the oxide phase. A recent oxidation study on the same ZrC nanomaterial showed that thermally induced oxidation occurred at lower temperatures (~350 °C) as compared with a microcrystalline counterpart (~375 °C), and that the oxide phase initially formed is tetragonal ZrO_2 [123]. In either case, the minor unit-cell contraction in nanocrystalline ZrC as opposed to the pronounced unit-cell swelling reported for nanocrystalline CeO_2 irradiated under identical conditions [17]. Because of enhanced redox changes for smaller grain sizes and formation of $Ce_{11}O_{20}$, nanocrystalline CeO_2 has a ~30% greater saturation swelling value when compared with its microcrystalline counterpart irradiated over the same fluence regime [17]. This shows that the response of ZrC under SHI irradiation is distinct from that of CeO_2 for both microcrystalline and nanocrystalline materials.

4.3.3 Results across different material compositions and beam conditions

Follow-on studies from the initial work published in Minnette, *et al*. (2023), evaluated ZrC (same as PVD1) and HfC (similarly produced, microcrystalline powder) that were irradiated at DC-60 in a similar procedure as described in *Chapter* 2. This work was published by Williams, *et al*., comparing ZrC to hafnium carbide (HfC), the results summarized in the table below [42].

Table 7. Tabulated results for comparison of different SHI irradiations of TMCs from this study and Williams, *et al.* [42].

	ZrC (946 MeV Au)	ZrC (198 MeV Xe)	HfC (198 MeV Xe)
Initial UCP [Å]	4.70 ± 0.01	4.69 ± 0.01	4.63 ± 0.01
Initial swelling saturation* [%]	0.03 ± 0.01	0.02 ± 0.01	0.02 ± 0.01
Swelling at highest fluence [%]	0.11 ± 0.01	0.18 ± 0.02	0.23 ± 0.03
Effective ion track size (diameter) [nm]	11 ± 1	6 ± 1	6 ± 1
Average electronic stopping power (S_e) [keV/nm]	42.7 ± 0.5	22.8 ± 0.5	23.4 ± 0.5
Wesch parameter [keV/nm]	160 ± 20	190 ± 30	200 ± 30

From Williams, *et al*., we observe two clear trends, the first being the lower energy ions (198 MeV Xe ions *versus* 946 MeV Au ions) result in more damage, not less. The second trend shown, is that the difference in target material composition (ZrC *versus* HfC) matters less than ion energy [42]. In all beam/material cases the same two-stage trend emerges with a consistent initial saturation starting around 8×10^{12} ions cm^{-2}. To reconcile the differences in ion energies, the most effective normalization technique is through an energy density correction. For SHIs a so-called Wesch correction factor, defined in the equation below, can be utilized [124].

$$w = S_e * 1/\pi\beta^{4k} \tag{20}$$

Where w is the energy density Wesch parameter, in keV/nm, S_e, is the electronic energy loss, in keV/nm, β, is the ion velocity expressed as a fraction of the speed of light, and k, is a corrective term taken to be 0.25. With this correction, the swelling values between various ion beam conditions normalizes.

4.4 DISCUSSION

The present study demonstrates that ZrC, like many simple oxide compounds (e.g., CeO_2), is highly tolerant to SHI irradiation. No amorphization is evident even after exposure to very high fluences (6×10^{13} ions cm^{-2}), and the only detectable material modification for microcrystalline ZrC is unit-cell expansion with microstrain buildup. In contrast to CeO_2, unit-cell expansion proceeds with ion fluence in a complex manner and is characterized by two distinct processes (Fig. 24). The initial damage-accumulation process for micro-ZrC appears to be similar to that of CeO_2 with a direct-impact defect creation mechanism. The cylindrical damage zone, or "track," for ZrC has a diameter on the order of 10 nm, which agrees well with the track sizes reported for many other ceramics irradiated under comparable conditions [38]. Defects are produced within individual ion tracks in a similar way as in CeO_2, and the relative unit-cell expansion reaches a

steady state at 0.03% for ZrC, and at 0.3% for CeO_2, when tracks overlap [125]. Coupled x-ray diffraction and x-ray absorption measurements previously showed that redox effects are an important component of radiation-induced swelling in CeO_2. Reduction of the cerium cation corresponds to an increase in the ionic radius, leading to the relatively large unit-cell expansion [17]. Given the covalent bonding of ZrC, along with the monovalancy of zirconium, similar radiation-induced redox changes would not be expected. Synchrotron XRD alone cannot provide the information needed to identify the type of defects that form in swift heavy ion-irradiated ZrC, but a direct comparison with CeO_2 shows that their impact on the unit-cell parameter is small (lower saturation swelling). The same Poisson-type trend in unit-cell expansion was also reported for both materials in low-energy ion irradiations within the nuclear energy loss regime, where ZrC had a relative unit-cell expansion of 0.14% with 4 MeV Au ions [118], [119], with ZrC retaining its starting structure following low-energy ion exposure. This was explained in part due to the mixed covalent and metallic bonding nature in ZrC, which decreased overall displaced atom mobility, leading to increased local recombination. The increased recombination rate allows for steady–state defect production and annealing, thereby leading to saturation [119], [126]. Neutron irradiations have also been performed on ZrC at varying temperatures (between 600 and 1600 °C) within a nuclear reactor [127]. Under these conditions, unit-cell expansion is much higher, reaching ~1.2% at 9 dpa [127]. This swelling was linked to the formation of "black-spot" defects that were identified as dislocation loops using transmission electron microscopy (TEM) [127], [128]. Temperature effects were also correlated in this study and, as expected from other materials [129], [130], the average loop size grew with increasing neutron irradiation temperature as a result of increased vacancy mobility, with concomitant decrease in loop density. Compared with all these

previous irradiation studies, we show here that swift heavy ions cause damage in ZrC, which leads only to isolated defect formation and changes in the unit-cell parameters.

The distinguishing feature for ZrC is the existence of a second damage mechanism at high fluences succeeding the direct-impact behavior. This defect accumulation process is characterized by a linear swelling regime with increasing fluence with no apparent saturation up to the maximum fluence, reaching a relative swelling value of ~0.11% at 6×10^{13} ions cm^{-2} (Fig. 24). The origin of this behavior remains unclear, and additional characterization is required to gain further insight (e.g., neutron total scattering or TEM). The second defect accumulation process is absent in CeO_2 and must be related to material properties specific to ZrC. Key differences between the two materials include (*i*) the presence of intrinsic carbon vacancies in ZrC with a maximum carbon site occupancy of ~96 at. % (in contrast to CeO_2 with pure anion stoichiometry) [119], (*ii*) pronounced covalent bonding character in ZrC *vs* ionic bonding present in CeO_2 [120], [121], and (*iii*) the distinct rocksalt and fluorite structures of ZrC and CeO_2, respectively.

It has been previously reported that fully stoichiometric ZrC cannot be synthesized, with a calculated limit of $ZrC_{0.96\pm0.01}$ [7], [9]; however, ZrC, as well as many other covalently bonded transition metal materials, retains phase homogeneity despite this non-stoichiometric nature down to $ZrC_{0.62\pm0.02}$ [7]. Carbon vacancies are shown to occur in as-synthesized hypostoichiometric ZrC_x samples ($0.5 \leq \times \leq 1.0$) creating short-range order (SRO) related to a Zr_8C_7 phase identified by TEM and neutron scattering [14], [131]. ZrC as synthesized by way of carbothermic reduction from ZrO_2 may lead to residual oxygen retained within the sample [131]. This residual oxygen remains dissolved within the rocksalt structure and contributes to filling intrinsic carbon vacancies [132], [133]. Additional vacant carbon sites are likely induced by SHI irradiation that are filled with oxygen, leading to the observed lattice contraction in nanocrystalline ZrC [132]; ingress of

oxygen appears to be much lower in microcrystalline ZrC as evidenced by the consistent unit-cell expansion and lack of ZrO_2 formation across all three sample series. A recent combined neutron and x-ray total scattering study on the pristine SG and PVD samples used in this study determined a Zr:C stoichiometry that reaches the limit with $ZrC_{0.98\pm0.02}$ [16]. Therefore, similar SRO can be expected in the starting materials, which cannot be detected with a long-range XRD analysis. This SRO is probably modified under irradiation through (*a*) accumulation of point defects created by the initial direct-impact regime and induced local stoichiometry fluctuations, as well as (*b*) migration of carbon site vacancies enabled by the intense ionizing radiation, promoting the formation of more complex vacancy clusters. Complex vacancy clusters are unfavorable in unirradiated ZrC due in part to the restricted second-nearest neighbor vacant site coordination [134], but the highly nonequilibrium conditions created by SHI irradiation may alleviate this restriction. Such vacancy clusters would explain the nonsaturating swelling at higher fluences as they create larger local domains of hypothetically "*pure*" ZrC stoichiometry with an increased unit cell volume [9] and form additional free volume into which the lattice can expand as shown for other materials [131]. Additional studies are needed to evaluate the influence of SRO and carbon stoichiometry on the swelling behavior in ZrC and to determine whether or not the nonstoichiometry can explain the nonsaturating unit-cell swelling at higher fluences.

The covalent bonding character in ceramic materials (ZrC) is less restrictive relative to ionic systems (CeO_2), enabling the existence of a wide variety of defect configurations. Covalent forces tend to dominate short-range interactions, as opposed to ionic forces, which dominate long-range interactions [135], [136]. Covalent bonding enables more numerous pathways for atomic mobility in irradiated materials via energized atom pairs acting in cooperation to break an existing bond [135], [137]. In many systems (e.g., ABO_3) this can result in amorphization [135]. Although

no amorphization is observed here, a similar model of covalently bonded individual atomic pairs (i.e., Zr–C and C–C) may work together to break bonds in the ZrC crystal during the thermal spike phase and prior to recrystallization during the quench phase of SHI irradiation [38]. This may explain how larger and more complex defects could form and contribute to the second swelling mechanism. Both items (*a*) and (*b*) may rely on prior irradiation of the structure (i.e., first swelling mechanism), wherein simple defects both weaken bonds and create initial lattice swelling.

Additional structural considerations may also contribute to the different radiation responses of CeO_2 and ZrC. Both materials are cubic, but the anion sublattices of the respective systems are simple cubic (CeO_2) and face-centered cubic (ZrC). This leads to different slip systems, which alters how intermolecular bonds within a crystalline material break under strain [138]. This may contribute to the formation of more complex defects such as loops and clusters at higher fluences. It has been previously shown that track sizes are similar in a wide range of amorphizable ceramics with different chemical compositions and structures [38]. However, the final damage morphology within the ion tracks depends on the recrystallization processes following the thermal spike and the structure of the target material [139]. The different anion arrangement and related diffusion properties may contribute to the observed effects [139].

Within irradiated nanocrystalline ZrC, the fluctuation in oxide phase fractions suggests a heterogeneous oxidation process. It remains unclear at which point oxidation occurred and whether it was induced during or after ion-beam exposure. Oxygen has been consistently reported in as synthesized ZrC, dissolved within vacant carbon sublattice sites of the rocksalt structure with no clear signature in XRD patterns [131], [137]. Under intense swift heavy ion irradiation, additional oxygen may be driven into ZrC, surpassing the solubility limit, and forming ZrO_2 at higher fluences. This effect was not observed in microcrystalline ZrC, which can be likely attributed to

much lower dissolved oxygen in the pristine sample due to, the decreased fraction of vacant carbon sublattice sites, and the decreased relative surface area-to-volume ratio [123]. The compressive strain induced by the ZrO_2 phase can result in unit-cell contraction within ZrC, which would explain the observed radiation response of nanocrystalline ZrC [140], [141]. The opposite is observed in nanocrystalline CeO_2, which experiences ~30% more swelling compared with microcrystalline CeO_2 [17]. This effect was shown to be the result of cation reduction (Ce^{4+} to Ce^{3+}), which is much more enhanced for nanocrystalline samples [17]. As mentioned above, redox effects are inactive in ZrC due to the monovalent character of the zirconium cation. Despite the unclear trend in unit-cell volume change, it is still clear that nanocrystalline ZrC retains a high degree of resiliency to SHI irradiation.

The validity of specific non-radioactive surrogates for this study is subject to some degree of uncertainty. Numerous parameters crystallographic, chemical, electrical, and thermodynamic properties should be aligned in order to claim that any given surrogate carbide is compatible to uranium carbide when subject to these conditions. For instance, uranium carbide's thermal conductivity is on the order of 280 W/mK compared to zirconium carbide which is around 50 W/mK [142], [143]. Similarly electric conductivity for the two materials are more comparable with both values being around 2.5×10^6 S/m [142], [144]. Both values are highly important when considering the mechanisms driving energy exchange and defect formation (during the thermal spike phase) resulting from SHIs [38].

4.5 CONCLUSIONS

The response to ionizing radiation of a ZrC advanced nuclear fuel analogue was examined and compared with that of CeO_2, an analogue for current UO_2 nuclear fuels. Synchrotron XRD analysis with structural refinement reveals distinct defect formation processes in each material.

Microcrystalline ZrC is resistant against amorphization but exhibits an unexpected two-step defect accumulation behavior. Independently of the synthesis procedure, the unit cell initially increases with fluence according to a direct-impact behavior. The deduced track diameter is 11 ± 2 nm and is comparable to that observed in other insulators. Once tracks severely overlap and swelling reaches saturation at high fluences, a second defect accumulation process initiates which is characterized by a pronounced linear swelling. The highest observed unit-cell expansion was ~0.11%, with no apparent saturation up to the maximum fluence tested (6×10^{13} ions cm^{-2}). This second damaging regime is absent in CeO_2, which only shows the direct-impact behavior to the same maximum fluence. The underlying atomic-scale mechanisms associated with this second damaging process are not accessible by synchrotron XRD analysis alone. It is likely that the hypostoichiometric nature of zirconium carbide with high levels of intrinsic anion vacancies, together with the covalent bonding character, play a critical role. This two-step defect accumulation process appears to be related to electronic energy loss, as it has never been observed for low-energy ion irradiation of ZrC. Nanocrystalline ZrC irradiated under the same conditions did not exhibit a two-step defect accumulation process, and instead the unit cell underwent minor contraction with increasing ion fluence. This is accompanied by oxidation, resulting in the formation of a small fraction of ZrO_2. Further studies are necessary to gain additional insight into the complex response of ZrC to swift heavy ion irradiation. Future experimentation will also be required to correlate the observed atomic scale swelling to macroscopic swelling as a result of SHI irradiation. If ionizing fission-fragment type irradiation at elevated temperatures leads to the same swelling behavior with no saturation in UC compounds, this may have important implications for these advanced fuel forms compared to conventional oxide fuels.

CHAPTER 5: RESPONSE OF URANIUM CARBONITRIDES AND OXIDE TO HIGHLY IONIZING RADIATION

The following chapter covers the radiation response of actinide carbides, nitrides, and oxides to SHIs. The UC_xN_{1-x} system is of great interest as a candidate material within as a TRISO particle fuel kernel. Understanding the impact of SHIs, used here to mimic fission fragments, is essential to fill knowledge gaps on radiation performance in reactor environments. To accomplish this objective the following questions will be answered:

1. What impact does highly ionizing radiation have on the UC_xN_{1-x} material system?
2. What, if any, radiation response variance is there between carbides, nitrides, and oxides subject to the same conditions?
3. Are the same complex, multi-stage swelling mechanisms demonstrated in TMCs present with uranium bearing materials?

5.1 ABSTRACT

Uranium carbide (UC), nitride (UN) and oxide (UO_2) subjected to swift heavy ions (SHIs) undergo multifaceted structural transformations that alter physical properties. 198-MeV Xe ions, serving as an analog to fission fragments, were used to fully irradiate 10 μm thick powder samples in order to promote a more detailed understanding of how electronic energy exchange mechanisms create defects and the effect of such defects on the crystal structure of the respective materials. A systematic study of 12 fluence points ranging from unirradiated to the highest fluence of 8×10^{13} cm^{-2} were independently measured with synchrotron X-ray diffraction. Uranium carbide and uranium oxide both exhibit a modest direct-impact swelling trend, with UC at 0.152 ± 0.002 % and UO_2 at 0.06 ± 0.02 %. An equivalent cross-section diameter value of 3.1 ± 0.1 nm and 4.9 ± 0.5 nm was observed as well. Uranium nitride, meanwhile, exhibits a non-saturating incoherent trend. Complex phase interplay results from SHI exposure with oxide phase impurities growing

with fluence in both carbide and nitride materials. Subsequent characterization techniques, including Raman spectroscopy, scanning electron microscopy, and energy dispersive spectroscopy were all implemented to examine the mechanisms driving these structural modifications in the nuclear fuel-form materials.

5.2 INTRODUCTION

A reinvigorated push towards advancing the development of new nuclear energy technologies has been underway since the 2000s [145]. This includes the development of generation IV reactor capable nuclear fuel forms, supported by the advanced fuels campaign (AFC). Under the AFC, a major development effort has been dedicated to the advancement of accident tolerant fuels [146]. A prominent example of such is tri-structural isotropic (TRISO) coated particles. TRISO is generally comprised of a three layer configuration consisting of an internal fuel kernel, typically some combination of uranium carbide, nitride, or oxide (UC, UN, & UO_2, respectively). This internal layer is then encapsulated with pyrolytic carbon buffer layer(s) and a hermetically sealed silicon carbide containment layer [62], [63]. The combination of the three layers extending radially outwards allows for remarkable retention of fission off-gases as well as improved thermomechanical properties (*e.g.*, thermal conductivity) [63]. TRISO fuel particles have been studied in great depth for over 60 years, evaluating the fuel forms performance under several differing regimes (*e.g.*, neutron irradiation) however, there exists a clear knowledge gap pertaining to the fuel kernels radiation response to highly energetic fission fragments [63], [147], [148], [149].

Each of the two fission fragments produced during a fission event possess between 70-100 MeV of kinetic energy accounting for over 90% of the overall energy released during a fission event. These highly energetic ions interact with the fuel matrix through two mechanisms:

electronic energy loss, and nuclear energy loss [150]. Prior studies have probed the effects of nuclear (ballistic) energy loss on a variety of fuel compositions (*e.g.*, UC, UN, & UO_2) [28], [104], [151], [152], [153], [154], [155]. By contrast, there is little to no such comprehensive literature on the effects of the isolated component of electronic energy loss in carbonitride fuels (*i.e.*, UC_xN_{1-x}). To evaluate the effects of electronic energy loss we employ so-called *swift heavy ions* (SHIs) [44]. Here, we define SHIs as any ion with a mass more than ^{12}C, with an energy in excess of 1 MeV/amu. In this regime of ion-matter interactions, incident ions create intensive electronic excitation and ionization events (imparting energy on the order of 10s of eV per atomic bond), and through electron-phonon coupling, the energy is transferred to the target atoms [44]. In many ceramics these interactions, characterized by rapid and intensive heating along the ion trajectory before an equally rapid quench [38], result cylindrically confined zone of material surrounding the ion trajectory, defined as the ion track. Inside the track, a wide range of ion- and material-dependent modifications have been observed ranging from simple point defects to complete amorphization [35], [38], [39], [40], [41], [42]. It is only at the end of the ion range that nuclear energy loss begins to dominate [38].

In many ceramic compounds swelling from SHI irradiation have been shown to follow a direct-impact model [17], [44], [45], [46]. Within the direct-impact model, defects first are shown to accumulate linearly within individual tracks, before the tracks begin to overlap resulting in a sub-linear trend, and finally the entire sample is covered in tracks resulting in a steady-state condition where defects are produced and annealed at equal rates. This track overlap effect is related both to the ion fluence (ϕ) and a cross-section term (σ), which is directly related to the cross-sectional area of the impinging ion track. In the case of lattice swelling the evolution of the lattice parameter (a) can be described as a function of σ and ϕ using a Poisson equation (eq. 2):

Prior studies have shown that similar actinide materials follow this same Poisson trend, in *Cureton et al*., we see both ThO_2 and, to a lesser extent, nanocrystalline UO_2 lattice swelling follows the trend described with eq. 2. While no prior SHI irradiation studies have been conducted on UC_xN_{1-x}, similar studies have found that isostructural surrogate materials zirconium carbide (ZrC) and hafnium carbide (HfC) follow an altogether distinct trend [41], [42]. Both ZrC and HfC exhibit a two-stage swelling mechanism wherein, the first stage is governed by a Poisson trend (eq. 2) before an extended saturation that yields to a continued linear swelling regime. A set of proposed theories discussing the origin of this more complex behavior is discussed in *Minnette et al*, where it is suggested that the intrinsically hypostoichiometric nature of the transition metal carbide compounds may be the primary driver [41].

For this study, 198 MeV ^{132}Xe ions were used to irradiate the fuel form compounds. An energy loss plot as a function of penetration depth into the sample, produced using SRIM, is shown in figure 8 [43]. Here, we find that these ions are sufficiently energetic to fully penetrate the sample thickness (10 μm). The average energy deposition for Xe ions in UC was found to be 22 ± 7 keV/nm, as calculated over the full thickness of the sample using SRIM results. Nuclear energy loss was found to be ~2 orders of magnitude lower than the contribution from electronic energy loss and was therefore neglected. Refined results produced from the post-irradiated examination conducted with XRD are discussed below and may be a guide to help produce more detailed holistic models of advanced nuclear fuel compounds under reactor operation.

5.3 RESULTS

The following section summarizes the experimental findings, as well as the results from the processed data as collected. All data were collected, processed, and refined using the techniques described previously in *chapter 2*.

5.3.1 Scanning electron microscopy and energy dispersion spectroscopy

Scanning electron microscopy (SEM) and electron dispersive spectroscopy (EDS) measurements were conducted on both unirradiated and irradiated uranium carbide and nitride platelets. Quantification of both grain/particle size and qualitative assessment of the materials' chemical characteristics were conducted to help better correlate potential defect creation pathways following SHI irradiation. Figures 28 and 29 depict the results from these measurements. For the pristine UC, we observe a mostly uniform and concise distribution of grains with minimal coarse chunks of material. EDS concurs with this result as the pristine sample shows no distinctive regions of chemical heterogeneities (*i.e.*, no oxide rich regions). This however changes when irradiated ($\Phi = 6 \times 10^{13}$ cm^{-2}) with SHIs, where distinct black regions, correlated to oxygen rich material, appear. We also observe large particles of material that are an order of magnitude larger than the primary distribution. This large particle effect may be correlated to material preparation or irradiation. The opposite fluence trend is depicted for the UN sample, with the pristine possessing large chunks of oxygen rich material whereas the irradiated sample ($\Phi = 4 \times 10^{13}$ cm^{-2}), where the black regions appear dispersed into small pockets. Additionally, it should be noted that the EDS signature is almost indistinguishable between carbon and nitrogen atoms, with the graphite mounting tape dominating the EDS output for the UN pristine sample.

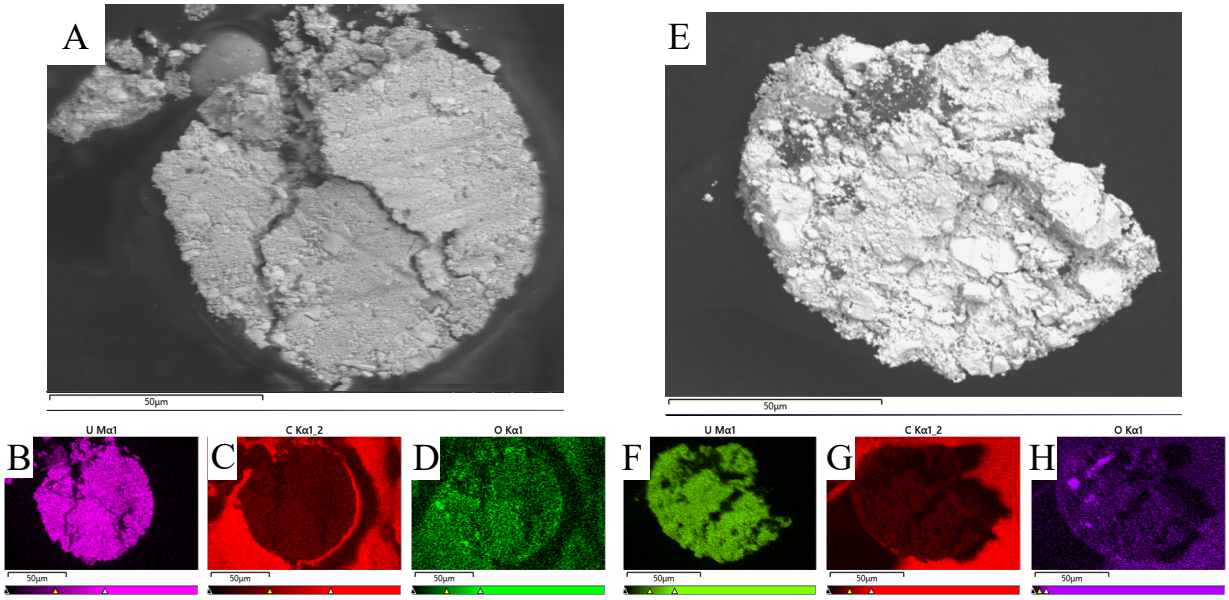

Figure 28. SEM of pristine UC (A), and irradiated ($\Phi = 6 \times 10^{13}$ cm^{-2}) collected at 750 times magnification (scale bar depicted on images). Corresponding EDS is shown for uranium, carbon, and oxygen. Figures B, C, & D (respectively) for pristine (A) and F, G, & H (respectively) for irradiated (E).

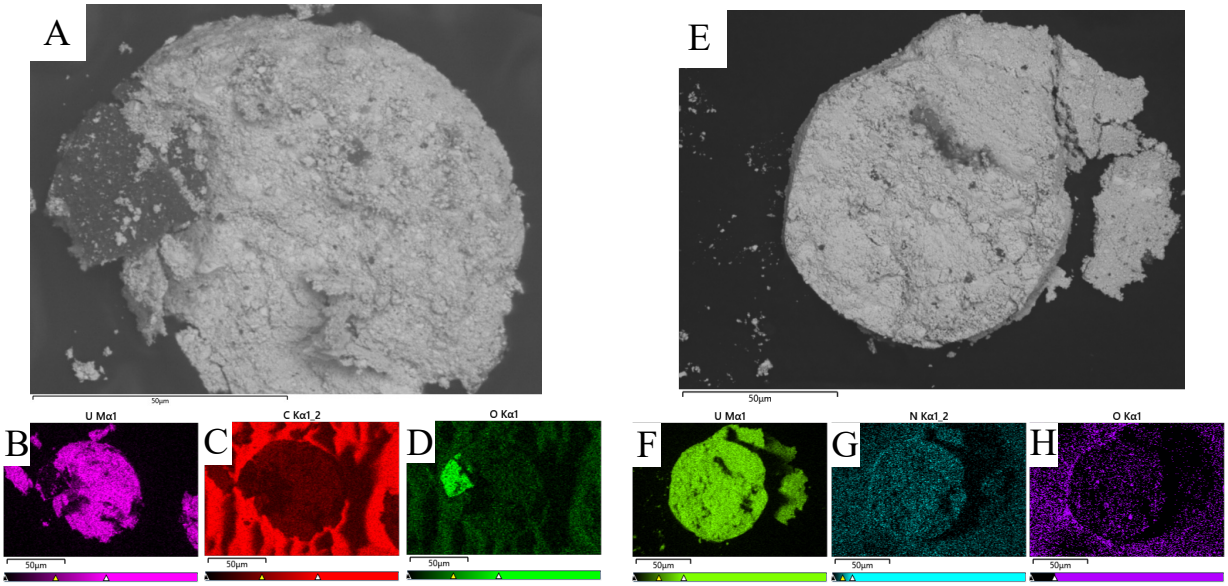

Figure 29. SEM of pristine UN (A), and irradiated ($\Phi = 4 \times 10^{13}$ cm^{-2}) collected at 750 times magnification (scale bar depicted on images). Corresponding EDS is shown for uranium, carbon, and oxygen. Figures (B), (C), & (D) for pristine (A) and (F), (G), & (H) for irradiated.

Grain size quantification was conducted in ImageJ with the smallest resolvable features in the micrographs being defined as '*particles*' or discrete collections of fine grains. Resolution limits make it difficult to determine the exact grain structure, but it can be assumed as no larger than the reported particle size. Following the described methodology (*chapter 2*), the mean grain size for the uranium carbide sample came out as 2 ± 1 μm for the pristine sample and 1.7 ± 0.6 μm for the irradiated sample. Likewise, for uranium nitride, pristine grain size of 0.7 ± 0.4 μm and for the irradiated sample 0.9 ± 0.7 μm. These results imply that no, or very minimal, grain size changes occur as a result of irradiation.

5.3.2 XRD and Rietveld analysis

The XRD patterns, figure 30, for the uranium carbide (figure 30 A) sample before irradiation revealed that the dominant peak contribution exhibits the rock-salt (Fm-3m) structure, which is correlated with the monocarbide/mononitride (UC/UN) phase. In addition, uranium carbide sample exhibits the tetragonal (*I*4/*mmm*) dicarbide (UC_2) phase. Figure 30 B highlights the primary (highest intensity) peaks for the phases resolved in the uranium carbide sample. Two primary trends emerge, the first is the evolution of an additional phase (indexed with the red dashed line) that can be correlated to UO_2 (*Fm*-3*m*). This evolution appears to scale with ion fluence, with the primary peak intensity growing relative to the rocksalt monocarbide and tetragonal dicarbide phases. The second observed trend is a small, but apparent, shift in the monocarbide rocksalt (111) peak. This leftward shift is correlated to a larger unit cell parameter, consistent with ion induced swelling. The uranium nitride sample (figure 30 C) also exhibited a primarily rocksalt (*Fm*-3*m*) structured phase that is accompanied with an additional broad peak (shown in figure 30 D) that is correlated to α - U_2N_3 (*Ia*-3, described in greater detail in *chapter* 3) as well as UO_2 (*Fm*-3*m*). The contributions from either phase are demarked with purple and red dashed lines respectively.

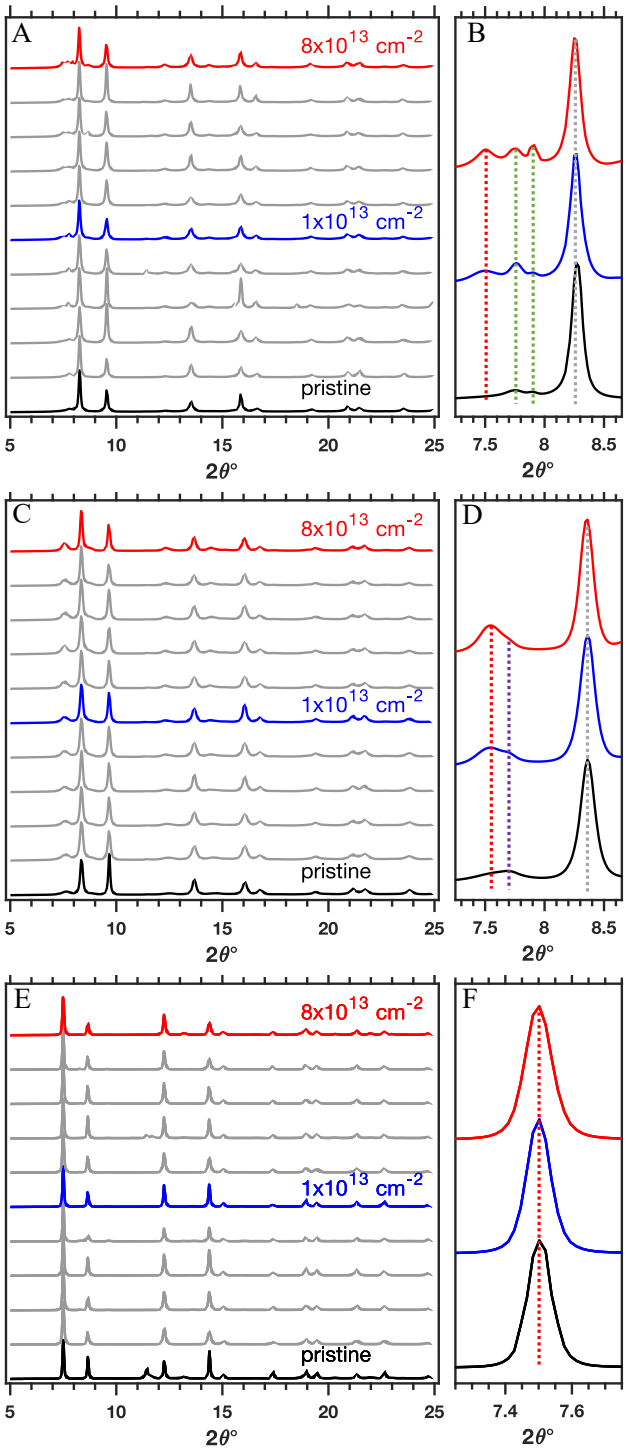

Figure 30. XRD diffraction plots: (A) UC, (C) UN, (E) UO_2. Plots (B), (D), and (F) depict a zoomed version of (111) reflection for highlighted fluence points, corresponding to UC, UN, and UO_2, respectively. Dashed lines indicate reflections for the following phases: rock-salt (shown in grey), UC_2 (shown in green), U_2N_3 (shown in purple) and UO_2 (shown in red).

Figure 30 D depicts the highest intensity peaks for all three phases, from this we observe a multitude of phenomenon. The first being the growth and broadening of the impurity phases (U_2N_3 and UO_2) peaks with respect to the mononitride UN (111) peak. Additionally, we can resolve that the U_2N_3 peaks (purple dashed line) diminishes as fluence increases, while the UO_2 peak (red dashed line) increases. This seems to suggest a correlated relationship between the two phases. Finally, although far less apparent compared to the UC (111) peak, we observe very modest peak shifts between the pristine and highest fluence (8×10^{13} ions cm^{-2}). The uranium oxide sample (figure 30 E), used primarily as a benchmark for comparison to the uranium carbide and nitride samples, far simpler with only the fluorite structured UO_2 phase being resolved. No fluence based phase evolution is observed and peak shifts are not readily detectable from the XRD plot alone. Minor peaks appear at inconsistent fluences (*e.g.*, at 11º in the pristine UO_2 sample) that are not correlated to any probable phase, rather these are artifacts from the sample gasket (304 AuSS). As shown, all materials are resilient to irradiation-induced amorphization up to the highest fluence evaluated (8×10^{13} ions cm^{-2}). Rather, evidence suggests minor crystalline distortions, *e.g.*, unit cell swelling, and phase transitions are induced from the SHI radiation evidenced by shifting UC/UN Bragg peaks, and the intensity fluctuations of impurity Bragg peaks.

Following SHI irradiation, Rietveld refinement was used to quantify unit cell swelling in the predominant rocksalt-structured monocarbide phase. For uranium carbide, the initial unit cell parameter of the UC phase was found to be 4.962 ± 0.001 Å. Refinement results also indicated an initial phase mix of 88 ± 2 wt. % UC and 12 ± 2 wt. % UC_2 (no detectable UO_2 in the pristine sample). With increasing fluence, the unit cell increases generally linearly with fluences before exhibiting a sublinear trend and saturation (figure 31).

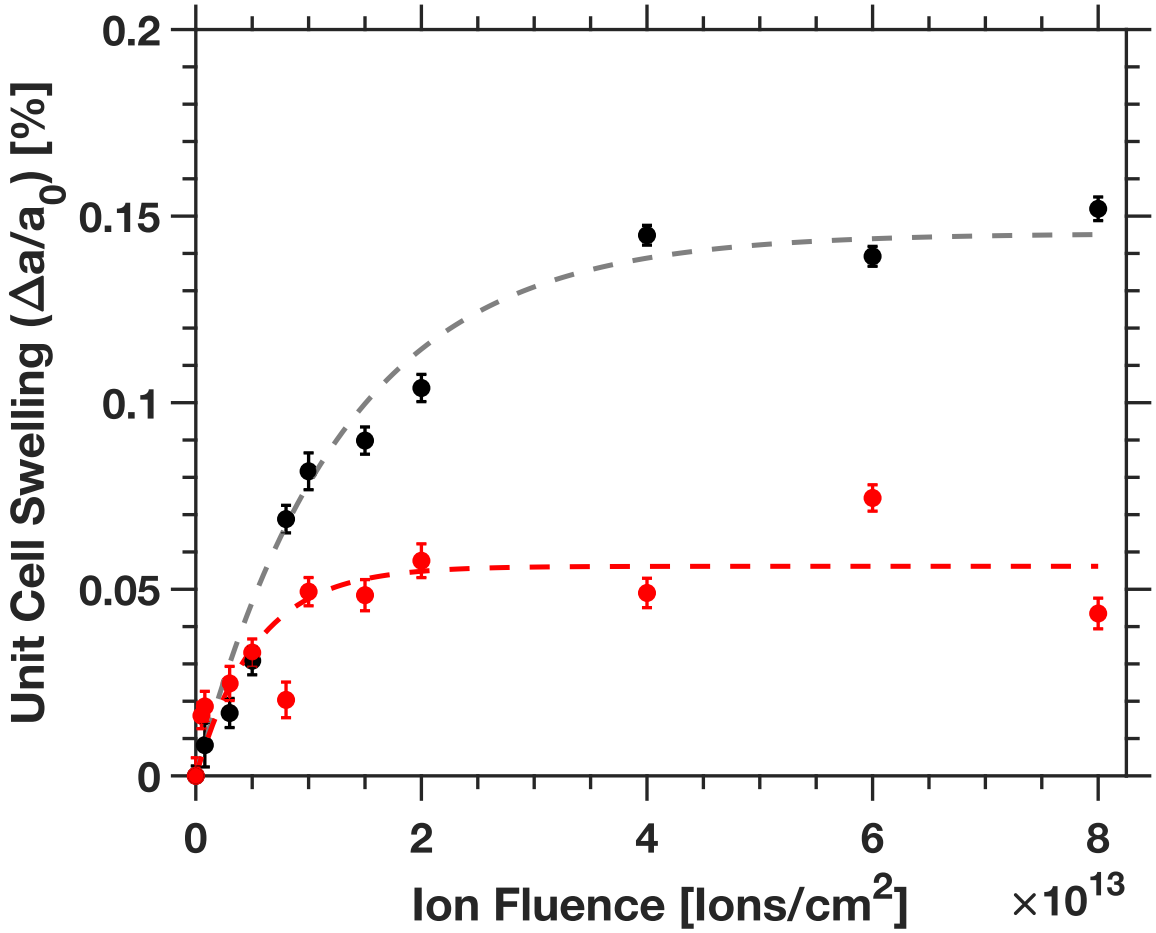

Figure 31. Relative unit cell swelling with respect to ion fluence of the UC (monocarbide, rock-salt) phase shown in black, with reference UO_2 swelling shown in red. Error bars indicate sample and refinement errors. Poisson trendline shown in respective colors.

This swelling profile closely follows the direct-impact Poisson trend [45], described in *equation (2)*, with UC swelling saturating starting at 4×10^{13} ions cm^{-2} reaching a level of 0.152 ± 0.003 % at the highest fluence 8×10^{13} ions cm^{-2}. Eq (2) allows us to extract the value of the damage cross-section which directly translates to the ion track cross-sectional area. In figure 31, the calculated cross-section diameter for UC is 3.1 ± 0.1 [nm] and for UO_2 4.9 ± 0.5 [nm]. The phase evolution, quantified by assessing the phase respective peak intensities using Rietveld refinement, figure 32, depicts a clear trend of decreasing UC phase fraction with increasing UO_2 phase fraction. These results agree with the SEM results (figure 28). The UO_2 phase reaches a saturation of 10 ± 1 wt. % at 2×10^{13} ions cm^{-2}. The UC phase decreases until reaching a saturation limit of 72 ± 5 wt. % and the UC_2 phase remains consistent at 15 ± 5 wt. % across all fluence points. Like the swelling profile, a Poisson-type trend can be used to describe the phase fractions. A cross-section value may be found for the UC phase with a diameter of 3 ± 1 nm, and for the oxide phase the cross-section diameter was found to be similar, at 4 ± 1 nm. Neither of the secondary phases possess any conclusive swelling profile.

Rietveld refinement results for uranium nitride were used to quantify both the swelling of the primary UN phase (figure 33), as well as the phase concentrations of the primary and impurity phases (figure 34). For the pristine uranium nitride, the UN phase has an initial unit cell parameter value of 4.907 ± 0.002 Å. The initial phase blend comprised of UN, U_2N_3, and UO_2 with values for each being 84 ± 5 wt. % UN, 10 ± 5 wt. % U_2N_3 and 6 ± 5 wt. % UO_2. As the fluence increases it becomes apparent that the UN swelling profile, figure 33, does not follow a Poisson-trend. As indicated, the swelling profile does not appear to have a clear saturation up to the highest fluence evaluated. Rather, the data scatter seemingly indicates a linear trend, with the relative swelling value of the highest fluence point evaluated being 0.099 ± 0.002 %.

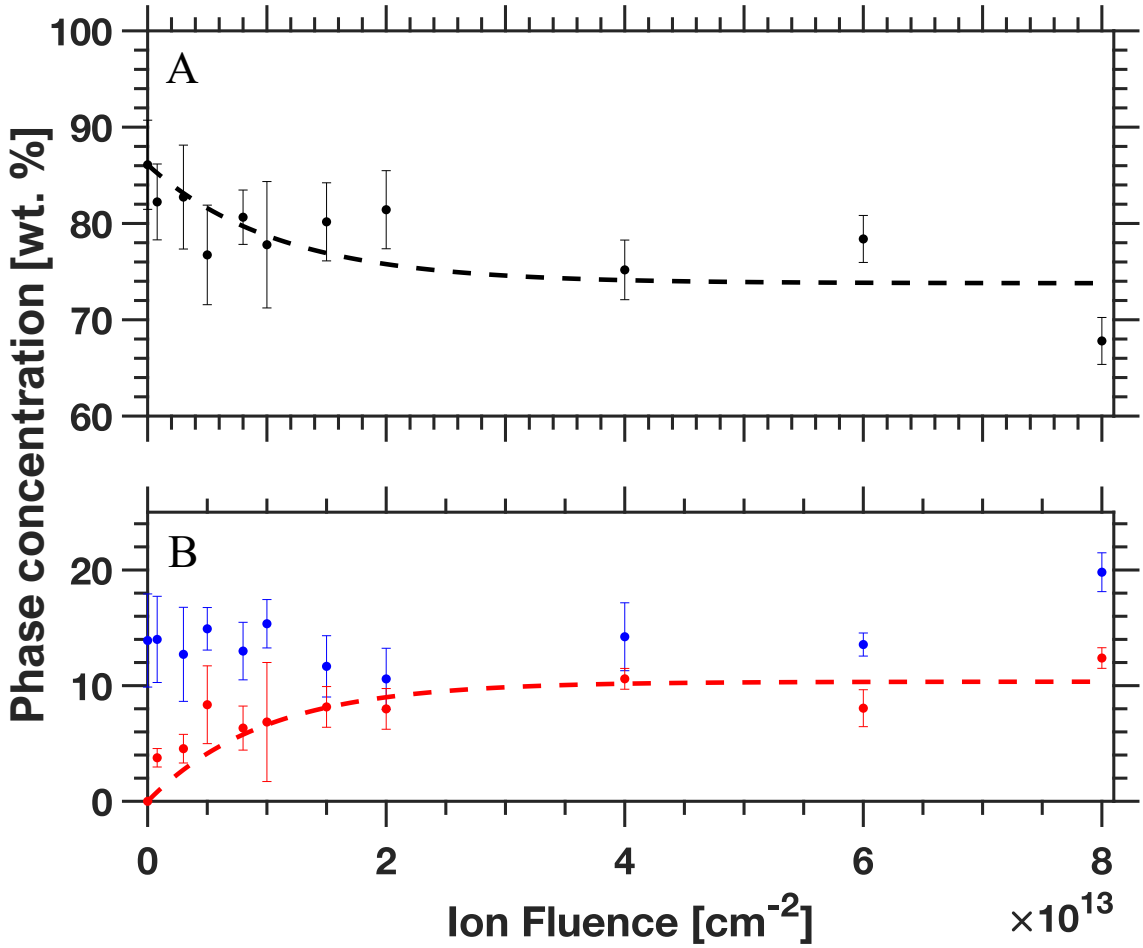

Figure 32. (A) Primary (UC), and (B) secondary phases (UC_2 & UO_2) in uranium carbide irradiated samples. Presented in black, red, and blue respectively. Error bars indicate sample and refinement errors.

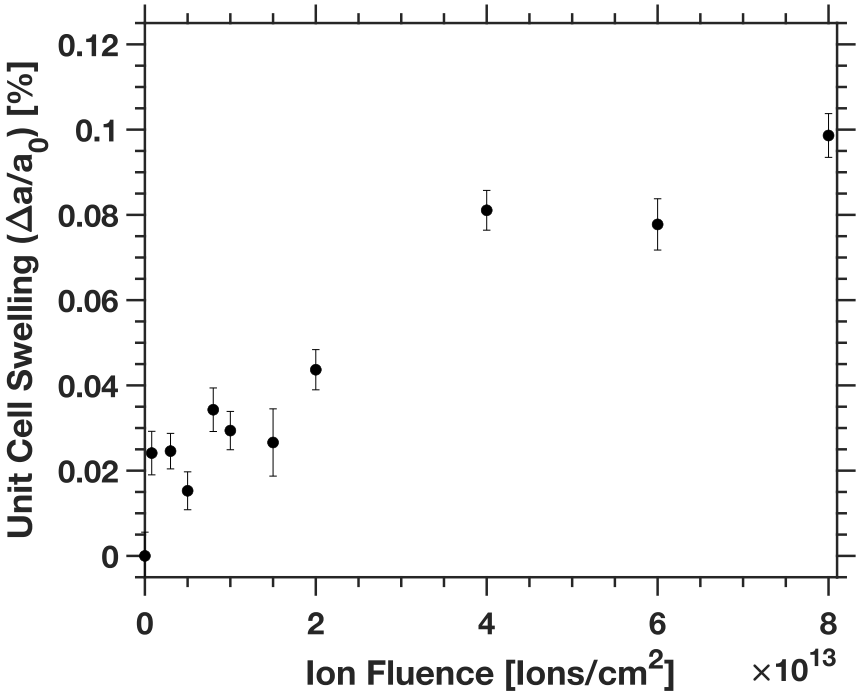

Figure 33. Relative unit cell swelling with respect to ion fluence of the UN (mononitride, rock-salt) phase. Error bars represent uncertainties from refinement.

The phase evolution within the uranium nitride sample, figure 34, is complex. With all three phases, UN, U_2N_3, and UO_2 changing with respect to ion fluence. The UN phase remains dominant but decreases as fluence increases. No clear trend can be resolved from the data scatter for UN but, the final value for phase fraction came out to be 70 ± 3 wt. % for UN, 26 ± 2 wt. % for UO_2, and 3 ± 2 wt. % for U_2N_3. UO_2 phase fraction systematically increases with ion fluence, following a Poisson trend with a correlated cross-section diameter is 3 ± 1 nm. U_2N_3 has an initial, rapid, spike, prior to a gradual depletion with increasing fluence. No one single trend was directly attributed due to this multi-step phenomenon. Like the uranium carbide sample, neither of the secondary phases possess any conclusive swelling profile.

XRD patterns were collected for the reference UO_2 irradiated sample, where only the fluorite (Fm-3m) phase was found. The initial unit cell parameter of UO_2 was found to be 5.470 ± 0.005 Å. UO_2 saturated at a fluence of 1×10^{13} ions cm^{-2} reaching a maximum swelling magnitude of 0.06 ± 0.02 % at the highest fluence evaluated, see figure 31. This result is highly interesting as it conflicts with the previously reported result in Cureton *et al*. which depicts unit cell contraction in microcrystalline UO_2. Albeit, the previously studied UO_2 possessed a smaller initial unit cell parameter value of 5.436 Å [17]. This is below the values found in other literature for a purely stoichiometric UO_2 sample, which typically fall within the range of 5.470 Å to 5.472 Å [156]. The various in stoichiometry and ion beam conditions likely explains the differences observed between the Cureton, *et al.* study and this project's findings.

Williamson-Hall analysis, figure 35, was performed to find the heterogenous microstrain, an indication of point-type defects for the uranium carbide and uranium nitride samples, as evaluated. Only the primary rocksalt structured phases were considered during this evaluation.

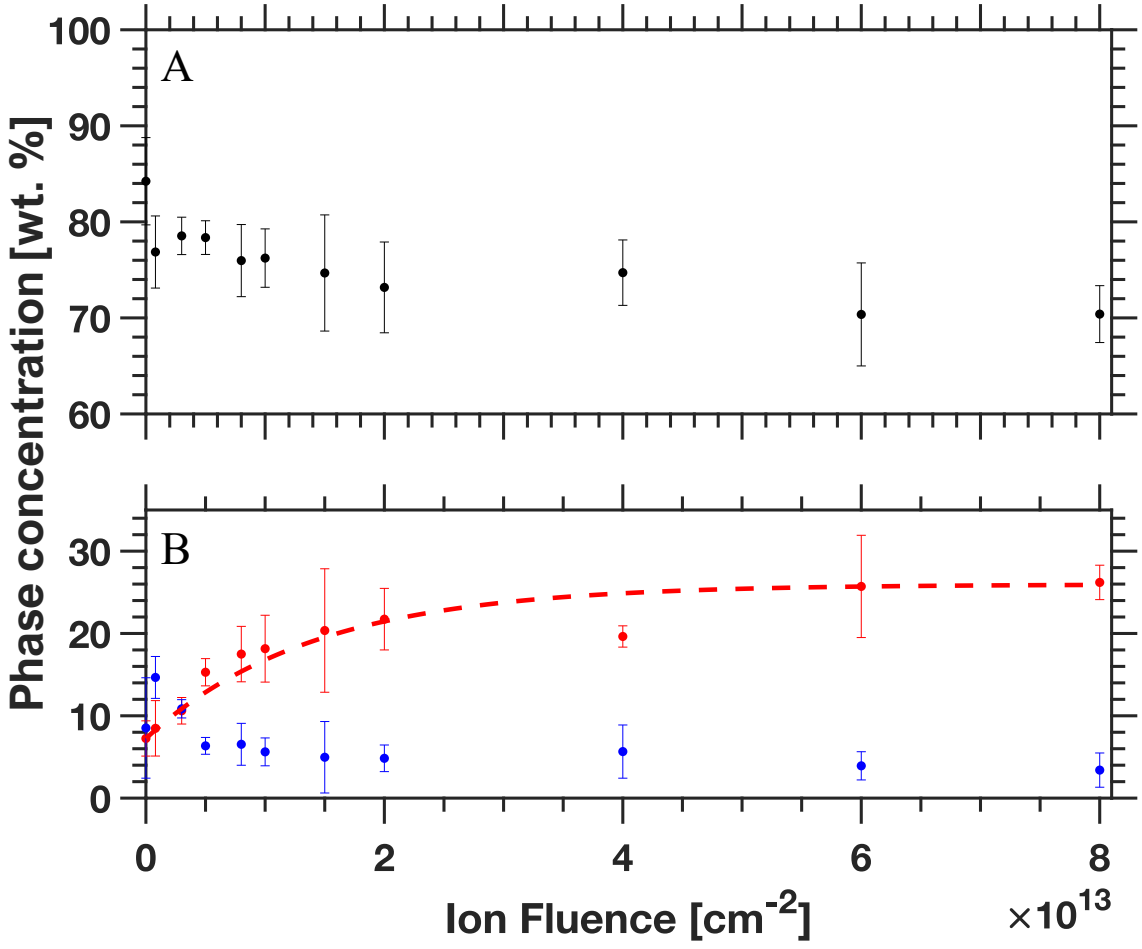

Figure 34. Refined phase fractions within UN sample, black represents the dominant mononitride phase, red is fluorite UO_2, and blue is U_2N_3. Representative error bars are shown.

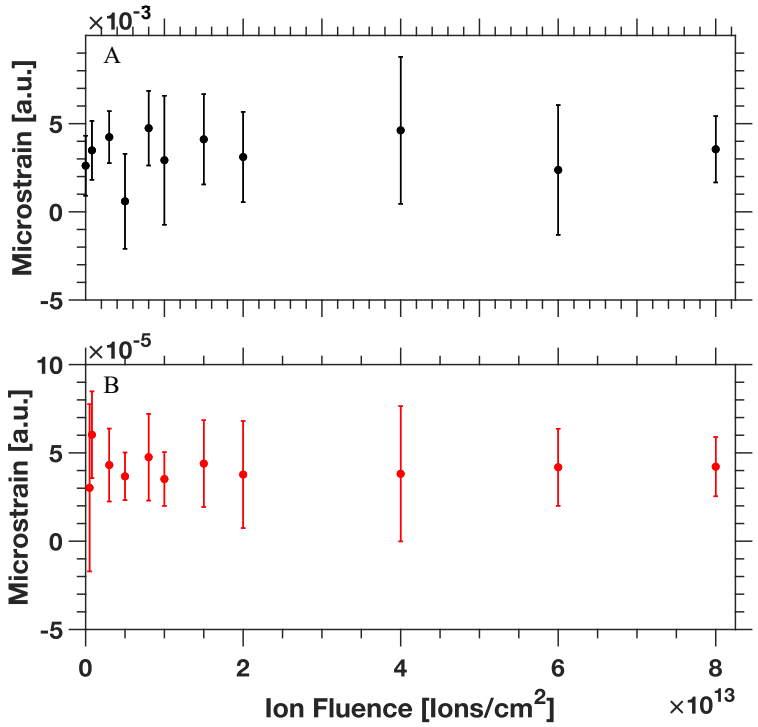

Figure 35. Microstrain with respect to fluence: A) UC (monocarbide, rock-salt phase), and B) UN (mononitride, rock-salt phase) samples. Error bars indicate sample and data analysis error.

Both the uranium carbide (shown in black in figure 35 A) and the uranium nitride (shown in red in figure 35 B) have no coherent microstrain accumulation trend. The initial strain value for the uranium carbide sample is 0.003 ± 0.002 %, this value fluctuates with increasing ion fluence ultimately reaching an identical value of 0.003 ± 0.002 % at the highest fluence point. The UN sample consistently has a microstrain value that is ~ 2 orders of magnitude lower than UC at each respective fluence point. The trend, or lack thereof, is similar between the two samples. For the uranium nitride sample the initial value is 0.00003 ± 0.00005 %, within error of 0, reaching a value of 0.00004 ± 0.00002 % at the highest fluence point evaluated. As found in prior studies, transition metal carbides (TMCs) synthesized using the sol-gel process typically have very low microstrain [16], [41]. The results here appear to confirm this phenomenon.

5.3.3 Raman spectroscopy

Raman spectroscopy was performed for qualitative assessment of defect types within the samples. Specifically, for the UO_2 sample which possesses a highly Raman active fluorite structure [17], [51], [156], [157]. The rocksalt structure meanwhile, is Raman inactive, meaning that any signal observed is due to defects or impurities within the probed region. These include the carbon correlated D and G bands, which have previously been observed in similarly produced uranium nitride samples [158]. Raman spectra were conducted on all three samples across the entire fluence range. A selection of data is presented in figure 36. With the uranium carbide sample, no fluence dependent behavior is obvious. The observed Raman modes around 1400 and 1600 cm^{-1} are correlated to carbon (D- and G-bands respectively) [159]. Both uranium carbide and nitride are observed to have broad peaks around 400-700 cm^{-1} which may correlate with fluorite-derivative peaks (UO_2 or U_2N_3) [160], [161].

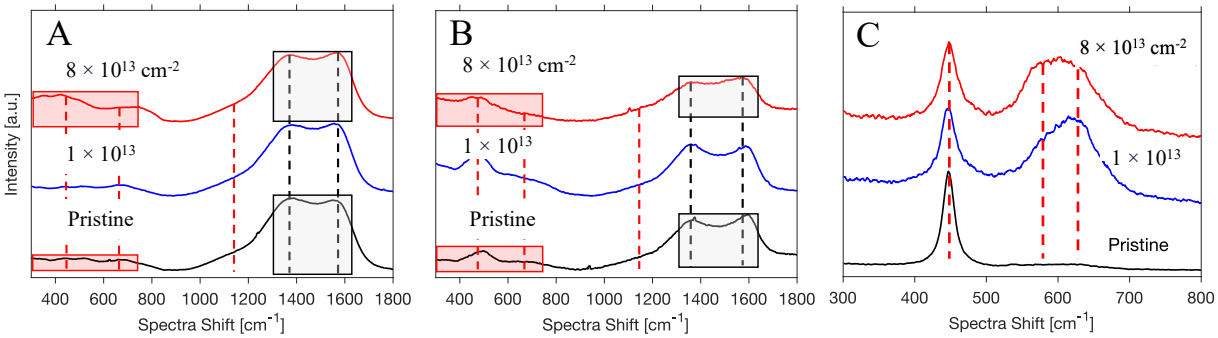

Figure 36. Collected Raman spectra for, (A) UC, (B) UN, and (C) UO_2 samples. Black dashed lines indicate Raman active modes associated with carbon; red dashed lines indicate Raman active modes associated with UO_2.

As observed within the UO_2 Raman spectra, two primary features dominate. The first is a sharp peak centered around 450 cm^{-1} this is related to the T2g mode, correlated to a purely crystalline fluorite structure. The second emerges with increasing fluence and is found between 550 and 650 cm^{-1}. The peak at 550 cm^{-1} is the 1LO Raman mode, this mode is typically inactive unless the fluorite structure is defective. The peak at 650 cm^{-1} is correlated to oxygen clusters related to the U_4O_9 phase, not observed in the XRD data [17], [160]. This can be seen by observing the 650 cm^{-1} peak growth relative to the T2g peak in figure 36 C. An additional trend emerges with increasing fluence, at intermediate fluence points we observe that the oxide cluster peak dominates over the 1LO (general defect) peak, however, at the highest evaluated fluence, the two peaks reach a nominally equal intensity. Exact quantifications of these results require informed input from DFT simulations.

5.5 DISCUSSION

SEM results show a large variance in observed particle size across the uranium carbide and uranium nitride samples. Resolution limitations from these SEM measurements made it difficult to interpret the exact microstructural make-up of the pristine and irradiated pellets however, we may assume that no nanocrystalline phenomenon are present. Additionally, we may use the correlated particle size as an upper bound on grain size meaning that it is unlikely that any one particle exceeded the dimension of the gasket hole within the thin foil. This is a useful confirmation as it implies that the packing fraction was below 100% throughout the sample and that the sample was fully irradiated (see figure 8). EDS offers some additional insight on the homogeneity across the samples. For uranium carbide it appears that carbon distribution is relatively uniform with no obvious pockets of uranium dicarbide or uranium oxide rich material. However, uranium nitride more clearly shows variance across the samples surveyed. With clear and apparent large oxide rich

pockets that were likely residual from either synthesis or created during the grinding process. The general tendency increased variability within the uranium nitride sample may offer some indicate as to why the swelling trend is incoherent.

The XRD results demonstrate clearly that all three materials are resilient to SHI irradiation, with minimal observed swelling/strain accumulation and no evidence of amorphization. The swelling behavior of uranium carbide is a clear example of the direct-impact model, saturating clearly before the highest ion fluence. Uranium oxide behaves in a similar manner, but these results conflict with what has been reported previously by Cureton, *et al*. where they observed very minimal unit cell contraction within their microcrystalline specimen [17]. In this previous study the researchers probed both microcrystalline and nanocrystalline samples following SHI irradiation with 946 MeV Au ions. They found swelling in the nanocrystalline sample that clearly followed a direct-impact trend. The main difference between the two samples was reconciled by evaluating the unit cell parameter and defect bands in the Raman spectra. The UO_2 sample in both studies possess a dominant T2g band at ~450 cm^{-1}, correlated to the pure fluorite oxide phase; however, the higher bands at ~575 and ~650 cm^{-1} are related to disordered and hyperstoichiometry, respectively. The ratio of the resolved peaks can be used to inform defect accumulation mechanisms. In this study, the defect bands in the pristine Raman spectrum are minimal in comparison to T2g band, suggesting minimal defects and nominally pure stoichiometry. The pristine unit cell parameter, 5.470 Å, is within the expected value for pure UO_2 [156]. Both UO_2 defect bands grow rapidly with fluence with the hyperstoichiometric band growing first and higher compared to the general disorder band. This suggests the irradiation is triggering the formation of oxygen clusters. Interestingly, this result tracks well with the nanocrystalline UO_2 from Cureton *et al*. which exhibits swelling, albeit with a greater magnitude [17]. Of note, U_3O_8 which was not

detected in any of the XRD patterns, offers an indication of some measure of hyperstoichiometric UO_{2+x} may exist on local length scales.

It is well understood that UO_2 contracts with increasing hyperstoichiometry, this was correlated to a stiffening of the bonds between U-O [156], [162]. Additionally, it is understood that in a general sense that UO_{2+x}, in comparison to UO_2, is a less stable system that can more readily incorporate additional O atoms, thereby leading to further oxidation and in turn, further unit cell contraction [163], [164]. This leads to the likely possibility that the initial differences in the starting oxidation state of the UO_2 samples drives a difference in defect generation kinetics, with the sample in Cureton, *et al*., oxidizing further and faster than the sample in this study [17]. Furthermore, the effects of general defect production (*i.e.*, defects not specific to oxidation) lead to volumetric expansion. Uranium Frenkel pairs, for instance, result in net volumetric expansion on the order of a few percent [165]. The competing effect of general (uranium driven) defects and oxidation defects likely results in the low swelling magnitude observed within this study.

The swelling behavior of uranium nitride is less clear in comparison to uranium carbide and nitride, this may be explained by inhomogeneities within the sample. This UN sample was produced from a carbide precursor. From XRD analysis alone, it is impossible to definitively quantify what fraction of the nonmetallic component is nitrogen or carbon. From previous studies, the uranium nitride sample was found to have resolved carbon within the UN phase, as described in *Chapter 3*. Using the following correlation, we can estimate the carbon fraction in UN with the unit cell parameter.

$$C = -38.29156 * a^2 + 363.323 * a - 860.02253 \quad (21)$$

Where, 'C' is the atomic fraction of carbon, and 'a' is the unirradiated unit cell parameter found using Rietveld refinements. The result suggests an atomic fraction of nitrogen (uranium

mononitride) of 80 ± 5 ph. %. From the collected Raman spectra, it can be shown that both the UC and UN samples produce some amount of oxide phase. It is also shown that the D and G bands, associated with carbon bonding at ~1350, and ~1550 cm^{-1} are present in both UC and UN samples. This offers an indication of residual carbide phase within the UN sample as suggested from the XRD results.

Uranium carbide and nitride, relative to isostructural transition metal carbides, have both been previously shown to have narrow homogeneity intervals [10]. That is, the range of stoichiometries that can maintain a common structure. Previous studies with isostructural transition metal carbides had proposed a strong interplay between defect formation kinetics and high concentrations of intrinsic structural vacancies, as described in *Chapter 4* [41], [42]. Modeling work may help diagnose the defect creation mechanisms and better inform what point defects are probably contributors to the observed swelling trend. For instance, oxygen incorporation energy in uranium nitride is known to be negative [22], so it is possible that dissolved oxygen permeates from both UN and U_2N_3 altering the respective unit cells in a manner that may be independent of simple defect formation (*e.g.*, Frenkel pairs).

5.6 CONCLUSIONS

The present study conducted a first of its kind, SHI irradiation experiment on uranium carbide and nitride materials. This study incorporated synchrotron X-ray microdiffraction to rapidly analyzed irradiated materials in a fluence based study. These studies may be used to help better inform models on the specific contribution of intensive electronic excitations within advanced nuclear fuels. To better inform these studies a direct comparison to uranium oxide, a material that has been previously studied with SHIs, was likewise irradiated, and measured in identical conditions. Overall, all three materials were found to be highly resilient to SHI irradiation,

with no detectable amorphization and only minimal lattice swelling having been observed. Uranium carbide and uranium oxide swell according to a well-established Poisson-type trend, with swelling saturating at 0.152 ± 0.003 % and 0.06 ± 0.02 % respectively. Correlated cross-sections for these swelling values were found to be 3 ± 1 nm and 4 ± 1 nm respectively. Uranium nitride, meanwhile, exhibits a less clear trend with the maximum swelling value being 0.099 ± 0.002 %. This behavior may be correlated to the complex chemical composition of nitrogen sublattice, which has been previously shown to incorporate oxygen and carbon atom species. The phases present in the uranium carbide and nitride samples likewise evolve with fluence, with both materials oxidizing. Although the exact origin of the oxidation is not fully understood, the effect likely impacts the ultimate swelling of both materials. In a similar manner, the structure of uranium oxide is known to be highly influenced by its stoichiometry with increasing oxidation driving unit cell contraction. Several open questions still remain following this study including, investigations into the defect structure of uranium carbide and nitride under similar conditions and the impact of stoichiometry on the radiation response to all three materials.

CHAPTER 6: CONCLUSIONS

These studies have revealed in greater detail, the complex nature of the structure of ultra-high temperature ceramics proposed for use in nuclear fuel form applications. Ranging from transition metal carbides to actinide metal carbonitrides, these materials offer great promise for use in industrial applications. Many open questions were answered with these studies, including the structure across-length scales with uranium carbide and nitride which had previously not been experimentally probed with total scattering techniques. From this work we managed to resolve, not only the phase composition of these materials, but other fundamental properties, including the susceptibility of carbon in uranium nitrides. On local length scales, the structure of both uranium carbide and uranium nitride follow closely to what is observed for the averaged long-range structure. Specifically, we were able to correlate bonding distances down to ~1.2 Å, relevant to the C-C dimer in the uranium dicarbide (UC_2) phase as observed. These techniques can help guide better synthesis routes for future utilization in nuclear fuel fabrication. Additionally, the work completed within this project involved the development of many techniques new to actinide/nuclear fuel characterization work, enabling more rapid characterization and validation of synthesized TRISO fuel kernels.

Studies into the effects of swift heavy ions (SHIs) in both transition metal carbides and actinide metal carbonitrides had presented a major knowledge gap. These studies are relevant as they can be utilized to understand the specific effect of fission-fragment energy range ions on high temperature ceramics for use in nuclear fuels. Zirconium and hafnium carbides exhibit a complex multi-stage swelling trend that has been observed previously. The swelling follows a Poisson-type trend that saturates at a modest fluence of 1×10^{13} ions cm^{-2}. Much beyond this fluence a secondary trend follows that appears linear, without apparent saturation up to the highest fluence point

evaluated of 6×10^{13} ions cm^{-2}. The origins of this trend are complex, but literature informed review has guided a hypothesis driven by the intrinsically hypostoichiometric nature of these materials. Further studies are still needed to confirm this hypothesis, including potential future studies with high resolution transmission electron microscopy or neutron total scattering.

Despite the inherently complex chemical nature of actinide carbonitrides, the swelling trend of these materials when exposed to SHIs follows a more simplistic trend. For uranium carbide and uranium oxide modest swelling is shown to follow a Poisson-type trend, much like previously studied CeO_2. This trend implies that these materials reach a saturation point wherein, defects are created and annealed at the same rate. Uranium nitride does not display a coherent trend but may still follow this same behavior. These results represent the first data isolating the impacts of electronic excitations from energetic heavy ions analogous to fission fragments on advanced nuclear fuel materials.

BIBLIOGRAPHY

[1] C. Folsom, C. Xing, C. Jensen, H. Ban, and D. W. Marshall, “Experimental measurement and numerical modeling of the effective thermal conductivity of TRISO fuel compacts,” *J. Nucl. Mater.*, vol. 458, pp. 198–205, Mar. 2015, doi: 10.1016/j.jnucmat.2014.12.042.

[2] C. Forsberg and A. Kadak, “Safeguards and Security for High-Burnup TRISO Pebble Bed Spent Fuel and Reactors,” *Nucl. Technol.*, vol. 210, no. 8, pp. 1354–1365, Aug. 2024, doi: 10.1080/00295450.2023.2298157.

[3] D. Olander, “Nuclear fuels – Present and future,” *J. Nucl. Mater.*, vol. 389, no. 1, pp. 1–22, May 2009, doi: 10.1016/j.jnucmat.2009.01.297.

[4] G. Locatelli, M. Mancini, and N. Todeschini, “Generation IV nuclear reactors: Current status and future prospects,” *Energy Policy*, vol. 61, pp. 1503–1520, Oct. 2013, doi: 10.1016/j.enpol.2013.06.101.

[5] E. Wuchina, E. Opila, M. Opeka, B. Fahrenholtz, and I. Talmy, “UHTCs: Ultra-High Temperature Ceramic Materials for Extreme Environment Applications,” *Electrochem. Soc. Interface*, vol. 16, no. 4, pp. 30–36, Dec. 2007, doi: 10.1149/2.F04074IF.

[6] G. S. Was, *Fundamentals of radiation materials science: metals and alloys*. Berlin ; New York: Springer, 2007.

[7] A. I. Gusev, A. A. Rempel, and A. J. Magerl, *Disorder and Order in Strongly Nonstoichiometric Compounds: Transition Metal Carbides, Nitrides and Oxides*, vol. 47. in Springer Series in Materials Science, vol. 47. Berlin, Heidelberg: Springer Berlin Heidelberg, 2001. doi: 10.1007/978-3-662-04582-4.

[8] Hagg, G., “Gezetsmassigkeiten im Kristallbau bei Hydriden, Boriden, Karbiden und Nitriden der Ubergangselemente,” *Phys. Chem.*, vol. 12, pp. 33–56, 1931.

[9] A. I. Gusev, S. I. Alyamovskii, Y. G. Zainulin, and G. P. Shveikin, “Structural Vacancies in Compounds of Variable Composition,” *Russ. Chem. Rev.*, vol. 55, no. 12, p. 1175, Dec. 1986, doi: 10.1070/RC1986v055n12ABEH003250.

[10] A. I. Gusev, “Short-range Order and Local Displacements of the Atoms in Non-stoichiometric Compounds,” *Russ. Chem. Rev.*, vol. 57, no. 10, pp. 913–928, Oct. 1988, doi: 10.1070/RC1988v057n10ABEH003401.

[11] J. C. Slater, “Atomic Radii in Crystals,” *J. Chem. Phys.*, vol. 41, no. 10, pp. 3199–3204, Nov. 1964, doi: 10.1063/1.1725697.

[12] B. Wei, Y. Wang, H. Zhang, D. Wang, S. Peng, and Y. Zhou, “Microstructure evolution of nonstoichiometric ZrC0.6 with ordered carbon vacancies under ion irradiation,” *Mater. Lett.*, vol. 228, pp. 254–257, Oct. 2018, doi: 10.1016/j.matlet.2018.06.010.

[13] Y. Zhou, T. W. Heitmann, E. Bohannan, J. C. Schaeperkoetter, W. G. Fahrenholtz, and G. E. Hilmas, “Carbon vacancy ordering in zirconium carbide powder,” *J. Am. Ceram. Soc.*, vol. 103, no. 4, pp. 2891–2898, Apr. 2020, doi: 10.1111/jace.16964.

[14] M. V. Klein, J. A. Holy, and W. S. Williams, “Raman scattering induced by carbon vacancies in Ti C x,” *Phys. Rev. B*, vol. 17, no. 4, pp. 1546–1556, Feb. 1978, doi: 10.1103/PhysRevB.17.1546.

[15] A. Ul-Hamid, “The effect of deposition conditions on the properties of Zr-carbide, Zr-nitride and Zr-carbonitride coatings – a review,” *Mater. Adv.*, vol. 1, no. 5, pp. 988–1011, 2020, doi: 10.1039/D0MA00232A.

[16] P. C. Huston *et al.*, “Characterization of zirconium carbide microspheres synthesized via internal gelation,” *J. Nucl. Mater.*, vol. 557, p. 153218, Dec. 2021, doi: 10.1016/j.jnucmat.2021.153218.

[17] W. F. Cureton *et al.*, “Grain size effects on irradiated CeO2, ThO2, and UO2,” *Acta Mater.*, vol. 160, pp. 47–56, Nov. 2018, doi: 10.1016/j.actamat.2018.08.040.

[18] G. Vasudevamurthy and A. T. Nelson, “Uranium carbide properties for advanced fuel modeling – A review,” *J. Nucl. Mater.*, vol. 558, p. 153145, Jan. 2022, doi: 10.1016/j.jnucmat.2021.153145.

[19] Charles Yeamans, “Synthesis of Uranium Flourides from Uranium Dioxide with Ammonium Biflouride and Ammonolysis of Uranium Flourides to Uranium Nitrides,” Ph.D. Dissertation, University of California, Berkley, Berkley, California, 2008.

[20] R. Benz and W. B. Hutchinson, “U + N2 Reaction layer growths,” *J. Nucl. Mater.*, vol. 36, no. 2, pp. 135–146, Aug. 1970, doi: 10.1016/0022-3115(70)90137-6.

[21] D. Bocharov, D. Gryaznov, Yu. F. Zhukovskii, and E. A. Kotomin, “Ab initio modeling of oxygen impurity atom incorporation into uranium mononitride surface and sub-surface vacancies,” *J. Nucl. Mater.*, vol. 416, no. 1–2, pp. 200–204, Sept. 2011, doi: 10.1016/j.jnucmat.2010.11.090.

[22] D. A. Lopes, A. Claisse, and P. Olsson, “Ab-initio study of C and O impurities in uranium nitride,” *J. Nucl. Mater.*, vol. 478, pp. 112–118, Sept. 2016, doi: 10.1016/j.jnucmat.2016.06.008.

[23] M. Freyss, “First-principles study of uranium carbide: Accommodation of point defects and of helium, xenon, and oxygen impurities,” *Phys. Rev. B*, vol. 81, no. 1, p. 014101, Jan. 2010, doi: 10.1103/PhysRevB.81.014101.

[24] A. Yu. Kuksin, S. V. Starikov, D. E. Smirnova, and V. I. Tseplyaev, “The diffusion of point defects in uranium mononitride: Combination of DFT and atomistic simulation with novel

potential," *J. Alloys Compd.*, vol. 658, pp. 385–394, Feb. 2016, doi: 10.1016/j.jallcom.2015.10.223.

[25] B. Ye *et al.*, "Irradiation effects in UO2 and CeO2," *J. Nucl. Mater.*, vol. 441, no. 1–3, pp. 525–529, Oct. 2013, doi: 10.1016/j.jnucmat.2012.09.035.

[26] C. Onofri *et al.*, "Full characterization of dislocations in ion-irradiated polycrystalline UO2," *J. Nucl. Mater.*, vol. 494, pp. 252–259, Oct. 2017, doi: 10.1016/j.jnucmat.2017.07.043.

[27] Hj. Matzke, P. G. Lucuta, and T. Wiss, "Swift heavy ion and fission damage effects in UO2," *Nucl. Instrum. Methods Phys. Res. Sect. B Beam Interact. Mater. At.*, vol. 166–167, pp. 920–926, May 2000, doi: 10.1016/S0168-583X(99)00801-0.

[28] A. Turos, S. Fritz, and Hj. Matzke, "Defects in ion-implanted uranium nitride," *Phys. Rev. B*, vol. 41, no. 7, pp. 3968–3977, Mar. 1990, doi: 10.1103/PhysRevB.41.3968.

[29] T. Wiss, Hj. Matzke, C. Trautmann, M. Toulemonde, and S. Klaumünzer, "Radiation damage in UO2 by swift heavy ions," *Nucl. Instrum. Methods Phys. Res. Sect. B Beam Interact. Mater. At.*, vol. 122, no. 3, pp. 583–588, Feb. 1997, doi: 10.1016/S0168-583X(96)00754-9.

[30] Y. Miao *et al.*, "Nano-crystallization induced by high-energy heavy ion irradiation in UO2," *Scr. Mater.*, vol. 155, pp. 169–174, Oct. 2018, doi: 10.1016/j.scriptamat.2018.04.006.

[31] S. D. Günay, "Investigation of Oxygen Diffusion in Irradiated UO2 with MD Simulation," *High Temp. Mater. Process.*, vol. 35, no. 10, pp. 981–987, Nov. 2016, doi: 10.1515/htmp-2015-0137.

[32] G. Martin, S. Maillard, L. V. Brutzel, P. Garcia, B. Dorado, and C. Valot, "A molecular dynamics study of radiation induced diffusion in uranium dioxide," *J. Nucl. Mater.*, vol. 385, no. 2, pp. 351–357, Mar. 2009, doi: 10.1016/j.jnucmat.2008.12.010.

[33] Hans Matzke, *Radiation effects in nuclear fuels*. Dordrecht: Springer Netherlands, 2007.

[34] S. J. Zinkle and G. S. Was, “Materials challenges in nuclear energy,” *Acta Mater.*, vol. 61, no. 3, pp. 735–758, Feb. 2013, doi: 10.1016/j.actamat.2012.11.004.

[35] M. Lang, F. Djurabekova, N. Medvedev, M. Toulemonde, and C. Trautmann, “Fundamental Phenomena and Applications of Swift Heavy Ion Irradiations,” in *Comprehensive Nuclear Materials*, Elsevier, 2020, pp. 485–516. doi: 10.1016/B978-0-12-803581-8.11644-3.

[36] A. J. Popel *et al.*, “Structural effects in UO 2 thin films irradiated with fission-energy Xe ions,” *J. Nucl. Mater.*, vol. 482, pp. 210–217, Dec. 2016, doi: 10.1016/j.jnucmat.2016.10.024.

[37] W. J. Weber and F. P. Roberts, “A Review of Radiation Effects in Solid Nuclear Waste Forms,” *Nucl. Technol.*, vol. 60, no. 2, pp. 178–198, Feb. 1983, doi: 10.13182/NT83-A33073.

[38] M. Lang, R. Devanathan, M. Toulemonde, and C. Trautmann, “Advances in understanding of swift heavy-ion tracks in complex ceramics,” *Curr. Opin. Solid State Mater. Sci.*, vol. 19, no. 1, pp. 39–48, Feb. 2015, doi: 10.1016/j.cossms.2014.10.002.

[39] A. P. Solomon, C. L. Tracy, E. C. O’Quinn, D. Severin, and M. K. Lang, “Transformations to amorphous and X-type phases in swift heavy ion-irradiated Ln2O3 and Mn2O3,” *J. Appl. Phys.*, vol. 129, no. 22, p. 225903, June 2021, doi: 10.1063/5.0050028.

[40] W. F. Cureton, C. L. Tracy, and M. Lang, “Review of Swift Heavy Ion Irradiation Effects in CeO2,” *Quantum Beam Sci.*, vol. 5, no. 2, p. 19, June 2021, doi: 10.3390/qubs5020019.

[41] J. Minnette *et al.*, “Response of ZrC to swift heavy ion irradiation,” *J. Appl. Phys.*, vol. 134, no. 18, p. 185901, Nov. 2023, doi: 10.1063/5.0165821.

[42] E. Williams *et al.*, “Swift heavy ion irradiation effects in zirconium and hafnium carbides,” *Nucl. Instrum. Methods Phys. Res. Sect. B Beam Interact. Mater. At.*, vol. 548, p. 165248, Mar. 2024, doi: 10.1016/j.nimb.2024.165248.

[43] J. F. Ziegler, M. D. Ziegler, and J. P. Biersack, “SRIM – The stopping and range of ions in matter (2010),” *Nucl. Instrum. Methods Phys. Res. Sect. B Beam Interact. Mater. At.*, vol. 268, no. 11–12, pp. 1818–1823, June 2010, doi: 10.1016/j.nimb.2010.02.091.

[44] M. Lang *et al.*, “Characterization of ion-induced radiation effects in nuclear materials using synchrotron x-ray techniques,” *J. Mater. Res.*, vol. 30, no. 9, pp. 1366–1379, May 2015, doi: 10.1557/jmr.2015.6.

[45] W. J. Weber, “Models and mechanisms of irradiation-induced amorphization in ceramics,” *Nucl. Instrum. Methods Phys. Res. Sect. B Beam Interact. Mater. At.*, vol. 166–167, pp. 98–106, May 2000, doi: 10.1016/S0168-583X(99)00643-6.

[46] C. L. Tracy *et al.*, “Defect accumulation in ThO2 irradiated with swift heavy ions,” *Nucl. Instrum. Methods Phys. Res. Sect. B Beam Interact. Mater. At.*, vol. 326, pp. 169–173, May 2014, doi: 10.1016/j.nimb.2013.08.070.

[47] R. D. Hunt, J. W. McMurray, G. W. Helmreich, B. D. Eckhart, A. L. McAlister, and A. T. Nelson, “Production of 28 μm zirconium carbide kernels using the internal gelation process and microfluidics,” *J. Nucl. Mater.*, vol. 528, p. 151870, Jan. 2020, doi: 10.1016/j.jnucmat.2019.151870.

[48] G. K. Williamson and W. H. Hall, “X-ray line broadening from filed aluminium and wolfram,” *Acta Metall.*, vol. 1, no. 1, pp. 22–31, Jan. 1953, doi: 10.1016/0001-6160(53)90006-6.

[49] T. B. Lindemer *et al.*, “Quantification of process variables for carbothermic synthesis of UC1-xNx fuel microspheres,” *J. Nucl. Mater.*, vol. 483, pp. 176–191, Jan. 2017, doi: 10.1016/j.jnucmat.2016.11.006.

[50] J. W. McMurray *et al.*, “Investigation of sol-gel feedstock additions and process variables on the density and microstructure of UN microspheres,” *J. Nucl. Mater.*, vol. 520, pp. 78–86, July 2019, doi: 10.1016/j.jnucmat.2019.04.003.

[51] R. I. Palomares *et al.*, “Defect accumulation in swift heavy ion-irradiated CeO_2 and ThO_2,” *J. Mater. Chem. A*, vol. 5, no. 24, pp. 12193–12201, 2017, doi: 10.1039/C7TA02640D.

[52] R. D. Hunt, J. L. Collins, M. H. Lloyd, and S. C. Finkeldei, “Production of more ideal uranium trioxide microspheres for the sol-gel microsphere pelletization process without the use of carbon,” *J. Nucl. Mater.*, vol. 515, pp. 107–110, Mar. 2019, doi: 10.1016/j.jnucmat.2018.12.029.

[53] Robert E. Dinnebier and Simon J.L. Billinge, *Powder diffraction: theory and practice*. Royal society of chemistry, 2015.

[54] C. A. Schneider, W. S. Rasband, and K. W. Eliceiri, “NIH Image to ImageJ: 25 years of image analysis,” *Nat. Methods*, vol. 9, no. 7, pp. 671–675, July 2012, doi: 10.1038/nmeth.2089.

[55] C. Park *et al.*, “New developments in micro-X-ray diffraction and X-ray absorption spectroscopy for high-pressure research at 16-BM-D at the Advanced Photon Source,” *Rev. Sci. Instrum.*, vol. 86, no. 7, p. 072205, July 2015, doi: 10.1063/1.4926893.

[56] J. Neuefeind, M. Feygenson, J. Carruth, R. Hoffmann, and K. K. Chipley, “The Nanoscale Ordered MAterials Diffractometer NOMAD at the Spallation Neutron Source SNS,” *Nucl. Instrum. Methods Phys. Res. Sect. B Beam Interact. Mater. At.*, vol. 287, pp. 68–75, Sept. 2012, doi: 10.1016/j.nimb.2012.05.037.

[57] Eric O’Quinn, “Neutron Total Scattering Analysis of Materials for the Nuclear Fuel Cycle,” *Nucl. Sci. Eng.*, 2025.

[58] V. Ciupină, S. Zamfirescu, and G. Prodan, “Evaluation of Mean Diameter values using Scherrer Equation Applied to Electron Diffraction Images,” in *Nanotechnology – Toxicological Issues and Environmental Safety and Environmental Safety*, P. P. Simeonova, N. Opopol, and M. I. Luster, Eds., in NATO Science for Peace and Security Series. , Dordrecht: Springer Netherlands, 2007, pp. 231–237. doi: 10.1007/978-1-4020-6076-2_15.

[59] B. H. Toby and R. B. Von Dreele, “*GSAS-II* : the genesis of a modern open-source all purpose crystallography software package,” *J. Appl. Crystallogr.*, vol. 46, no. 2, pp. 544–549, Apr. 2013, doi: 10.1107/S0021889813003531.

[60] C. L. Farrow *et al.*, “PDFfit2 and PDFgui: computer programs for studying nanostructure in crystals,” *J. Phys. Condens. Matter*, vol. 19, no. 33, p. 335219, Aug. 2007, doi: 10.1088/0953-8984/19/33/335219.

[61] D. L. Drey, E. O'Quinn, S. Finkeldei, J. Neuefeind, and M. Lang, “Local Ordering in Disordered Nd $_{x}$Zr $_{1-x}$O $_{2-0.5x}$ Pyrochlore as Observed Using Neutron Total Scattering,” *SSRN Electron. J.*, 2021, doi: 10.2139/ssrn.3890348.

[62] P. A. Demkowicz, B. Liu, and J. D. Hunn, “Coated particle fuel: Historical perspectives and current progress,” *J. Nucl. Mater.*, vol. 515, pp. 434–450, Mar. 2019, doi: 10.1016/j.jnucmat.2018.09.044.

[63] J. J. Powers and B. D. Wirth, “A review of TRISO fuel performance models,” *J. Nucl. Mater.*, vol. 405, no. 1, pp. 74–82, Oct. 2010, doi: 10.1016/j.jnucmat.2010.07.030.

[64] P. A. Demkowicz *et al.*, “Irradiation performance of AGR-1 high temperature reactor fuel,” *Nucl. Eng. Des.*, vol. 306, pp. 2–13, Sept. 2016, doi: 10.1016/j.nucengdes.2015.09.011.

[65] T. B. Lindemer, S. L. Voit, C. M. Silva, T. M. Besmann, and R. D. Hunt, “Carbothermic synthesis of 820μm uranium nitride kernels: Literature review, thermodynamics, analysis,

and related experiments," *J. Nucl. Mater.*, vol. 448, no. 1–3, pp. 404–411, May 2014, doi: 10.1016/j.jnucmat.2013.10.036.

[66] John Dunwoody, "Synthesis of Uranium Nitride and Uranium Carbide Powder by Carbothermic Reduction," Los Alamos National Laboratory, Los Alamos, New Mexico, LA-UR-07-4706, 2007.

[67] R. Springell *et al.*, "A review of uranium-based thin films," *Adv. Phys.*, vol. 71, no. 3–4, pp. 87–165, Oct. 2022, doi: 10.1080/00018732.2023.2230292.

[68] Pertti Malkki, "The manufacturing of uranium nitride for possible use in light water reactors," Doctoral dissertation, KTH Roayl Institute of Technology.

[69] H. M. Reiche, S. C. Vogel, and M. Tang, "In situ synthesis and characterization of uranium carbide using high temperature neutron diffraction," *J. Nucl. Mater.*, vol. 471, pp. 308–316, Apr. 2016, doi: 10.1016/j.jnucmat.2015.12.044.

[70] G. Vasudevamurthy and T. W. Knight, "Production of High-Density Uranium Carbide Compacts for Use in Composite Nuclear Fuels," *Nucl. Technol.*, vol. 163, no. 2, pp. 321–327, Aug. 2008, doi: 10.13182/NT08-A3991.

[71] D. M. King *et al.*, "Synthesis and Structure of a Terminal Uranium Nitride Complex," *Science*, vol. 337, no. 6095, pp. 717–720, Aug. 2012, doi: 10.1126/science.1223488.

[72] Y. Zhang, D. Meng, Q. Xu, and Y. Zhang, "Pulsed laser nitriding of uranium," *J. Nucl. Mater.*, vol. 397, no. 1–3, pp. 31–35, Feb. 2010, doi: 10.1016/j.jnucmat.2009.12.002.

[73] R. D. Hunt and J. L. Collins, "Uranium kernel formation *via* internal gelation," *Radiochim. Acta*, vol. 92, no. 12, pp. 909–915, Dec. 2004, doi: 10.1524/ract.92.12.909.55110.

[74] S. J. Cavazos, S. Younus, J. Uresti-Mireles, E. S. Sooby, and M. H. A. Piro, "Rare Earth Carbide (Nd-C and Ce-C) Synthesis and Characterization to Inform Phase Equilibrium in

Advanced Nuclear Fuels," *Metals*, vol. 14, no. 12, p. 1322, Nov. 2024, doi: 10.3390/met14121322.

[75] M. Bradley Sears, "Reactions of uranium carbonitrides and uranium nitride with aqueous solutions of hydrochloric, sulfuric, and nitric acids," *J. Inorg. Nucl. Chem.*, vol. 32, no. 9, pp. 2971–2984, Sept. 1970, doi: 10.1016/0022-1902(70)80363-3.

[76] R. E. Rundle, N. C. Baenziger, A. S. Wilson, and R. A. McDonald, "The Structures of the Carbides, Nitrides and Oxides of Uranium1," *J. Am. Chem. Soc.*, vol. 70, no. 1, pp. 99–105, Jan. 1948, doi: 10.1021/ja01181a029.

[77] T. Egami, "Atomic Dynamics in Real Space and Time," in *Inelastic X-Ray Scattering and X-Ray Powder Diffraction Applications*, A. Cunsolo, M. K. K. D. Franco, and F. Yokaichiya, Eds., IntechOpen, 2020. doi: 10.5772/intechopen.88334.

[78] John Desmond Bernal, "The structure of graphite," *Proc. R. Soc. Lond. Ser. Contain. Pap. Math. Phys. Character*, vol. 106, no. 740, pp. 749–773, Dec. 1924, doi: 10.1098/rspa.1924.0101.

[79] D. F. R. Mildner and J. M. Carpenter, "On the short range atomic structure of non-crystalline carbon," *J. Non-Cryst. Solids*, vol. 47, no. 3, pp. 391–402, Feb. 1982, doi: 10.1016/0022-3093(82)90215-0.

[80] E.W. Murbach, "The Oxidation of 'Reactive' Uranium Carbide (No. NAA-SR-6331)," Atomics Inter. Div. of North American Aviation, Inc., Canoga Park, Calif., 1961.

[81] V. G. Goncharov *et al.*, "Energetics of oxidation and formation of uranium monocarbide," *J. Nucl. Mater.*, vol. 581, p. 154446, Aug. 2023, doi: 10.1016/j.jnucmat.2023.154446.

[82] V. G. Goncharov *et al.*, "Energetics of oxidation and formation of uranium mononitride," *J. Nucl. Mater.*, vol. 569, p. 153904, Oct. 2022, doi: 10.1016/j.jnucmat.2022.153904.

[83] C. M. Silva *et al.*, “Characteristics of uranium carbonitride microparticles synthesized using different reaction conditions,” *J. Nucl. Mater.*, vol. 454, no. 1–3, pp. 405–412, Nov. 2014, doi: 10.1016/j.jnucmat.2014.08.038.

[84] T. B. Lindemer, S. L. Voit, C. M. Silva, T. M. Besmann, and R. D. Hunt, “Carbothermic synthesis of 820μm uranium nitride kernels: Literature review, thermodynamics, analysis, and related experiments,” *J. Nucl. Mater.*, vol. 448, no. 1–3, pp. 404–411, May 2014, doi: 10.1016/j.jnucmat.2013.10.036.

[85] C. M. Silva, R. D. Hunt, L. L. Snead, and K. A. Terrani, “Synthesis of Phase-Pure U_2 N_3 Microspheres and Its Decomposition into UN,” *Inorg. Chem.*, vol. 54, no. 1, pp. 293–298, Jan. 2015, doi: 10.1021/ic502457n.

[86] H. P. Nawada, P. S. Murti, G. Seenivasan, S. Anthonysamy, and C. K. Mathews, “Thermogravimetric study of the oxidation behaviour of uranium dicarbide,” *J. Therm. Anal.*, vol. 35, no. 4, pp. 1145–1155, July 1989, doi: 10.1007/BF01913032.

[87] J. D. Cox, D. D. Wagman, and V. A. Medvedev, *CODATA Key Values for Thermodynamics*, 1st ed. New York: Hemisphere Publishing Corp., 1984.

[88] E. J. Huber and C. E. Holley, “Enthalpies of formation of triuranium octaoxide and uranium dioxide,” *J. Chem. Thermodyn.*, vol. 1, no. 3, pp. 267–272, May 1969, doi: 10.1016/0021-9614(69)90046-9.

[89] M. Marchand, O. Fiquet, and M. Brothier, “Oxidation kinetic analysis of a mixed uranium dicarbide and graphite compound,” *J. Nucl. Mater.*, vol. 437, no. 1–3, pp. 310–316, June 2013, doi: 10.1016/j.jnucmat.2013.02.028.

[90] R. M. Dell, V. J. Wheeler, and E. J. McIver, “Oxidation of uranium mononitride and uranium monocarbide,” *Trans. Faraday Soc.*, vol. 62, p. 3591, 1966, doi: 10.1039/tf9666203591.

[91] E. H. P. Cordfunke, “Investigations on uranium carbonitrides (I),” *J. Nucl. Mater.*, vol. 56, no. 3, pp. 319–326, June 1975, doi: 10.1016/0022-3115(75)90049-5.

[92] J. Williams and R. A. J. Sambell, “The uranium monocarbide-uranium mononitride system,” *J. Common Met.*, vol. 1, no. 3, pp. 217–226, June 1959, doi: 10.1016/0022-5088(59)90030-X.

[93] F. Anselin, “Preparation and study of the nitrides and mixed carbide-nitrides of uranium and plutonium,” CEA Fontenay-aux-Roses, France, Thesis CEA-R--2988, June 1966.

[94] J. Liu *et al.*, “Thermal expansion and steam oxidation of uranium mononitride analysed via in situ neutron diffraction,” *J. Nucl. Mater.*, vol. 575, p. 154215, Mar. 2023, doi: 10.1016/j.jnucmat.2022.154215.

[95] A. E. Austin, “Carbon positions in uranium carbides,” *Acta Crystallogr.*, vol. 12, no. 2, pp. 159–161, Feb. 1959, doi: 10.1107/S0365110X59000445.

[96] N. Vigier *et al.*, “New Data on the Structure of Uranium Monocarbide,” *Chem. Mater.*, vol. 20, no. 9, pp. 3199–3204, May 2008, doi: 10.1021/cm8001783.

[97] D. R. Olander, “Fundamental aspects of nuclear reactor fuel elements,” TID-26711-P1, 7343826, Jan. 1976. doi: 10.2172/7343826.

[98] W. D. Kingery, J. Francl, R. L. Coble, and T. Vasilos, “Thermal Conductivity: X, Data for Several Pure Oxide Materials Corrected to Zero Porosity,” *J. Am. Ceram. Soc.*, vol. 37, no. 2, pp. 107–110, Feb. 1954, doi: 10.1111/j.1551-2916.1954.tb20109.x.

[99] I. L. Pioro, Ed., *Handbook of generation IV nuclear reactors*. in Woodhead Publishing series in energy, no. number 103. Amsterdam: Elsevier ; Woodhead Publishing, 2016.

[100] S. L. Hayes, J. K. Thomas, and K. L. Peddicord, “Material property correlations for uranium mononitride,” *J. Nucl. Mater.*, vol. 171, no. 2–3, pp. 289–299, May 1990, doi: 10.1016/0022-3115(90)90376-X.

[101] *Structural materials for generation iv nuclear reactors*, 1st edition. Waltham, MA: Elsevier, 2016.

[102] I. Pioro and S. Buruchenko, “Nuclear Power as a Basis for Future Electricity Generation,” *IOP Conf. Ser. Earth Environ. Sci.*, vol. 95, p. 042002, Dec. 2017, doi: 10.1088/1755-1315/95/4/042002.

[103] J. J. Serna *et al.*, “Experimental Observations on Fuel Pellet Performance at High Burnup,” *J. Nucl. Sci. Technol.*, vol. 43, no. 9, pp. 1045–1053, Sept. 2006, doi: wihyp.

[104] J. W. Harrison, “The irradiation-induced swelling of uranium carbide,” *J. Nucl. Mater.*, vol. 30, no. 3, pp. 319–323, Apr. 1969, doi: 10.1016/0022-3115(69)90248-7.

[105] J. Rest and G. L. Hofman, “Dynamics of irradiation-induced grain subdivision and swelling in U3Si2 and UO2 fuels,” *J. Nucl. Mater.*, vol. 210, no. 1–2, pp. 187–202, June 1994, doi: 10.1016/0022-3115(94)90237-2.

[106] N. Wang, Z. Wang, K. T. Aust, and U. Erb, “Effect of grain size on mechanical properties of nanocrystalline materials,” *Acta Metall. Mater.*, vol. 43, no. 2, pp. 519–528, Feb. 1995, doi: 10.1016/0956-7151(94)00253-E.

[107] H. Gleiter, “Nanocrystalline materials,” *Prog. Mater. Sci.*, vol. 33, no. 4, pp. 223–315, 1989, doi: 10.1016/0079-6425(89)90001-7.

[108] N. Nita, R. Schaeublin, and M. Victoria, “Impact of irradiation on the microstructure of nanocrystalline materials,” *J. Nucl. Mater.*, vol. 329–333, pp. 953–957, Aug. 2004, doi: 10.1016/j.jnucmat.2004.04.058.

[109] M. Rose, A. G. Balogh, and H. Hahn, “Instability of irradiation induced defects in nanostructured materials,” *Nucl. Instrum. Methods Phys. Res. Sect. B Beam Interact. Mater. At.*, vol. 127–128, pp. 119–122, May 1997, doi: 10.1016/S0168-583X(96)00863-4.

[110] Y. Chimi, A. Iwase, N. Ishikawa, M. Kobiyama, T. Inami, and S. Okuda, “Accumulation and recovery of defects in ion-irradiated nanocrystalline gold,” *J. Nucl. Mater.*, vol. 297, no. 3, pp. 355–357, Sept. 2001, doi: 10.1016/S0022-3115(01)00629-8.

[111]X.-M. Bai, A. F. Voter, R. G. Hoagland, M. Nastasi, and B. P. Uberuaga, “Efficient Annealing of Radiation Damage Near Grain Boundaries via Interstitial Emission,” *Science*, vol. 327, no. 5973, pp. 1631–1634, Mar. 2010, doi: 10.1126/science.1183723.

[112] J. Roleček, Š. Foral, K. Katovský, and D. Salamon, “A feasibility study of using CeO_2 as a surrogate material during the investigation of UO_2 thermal conductivity enhancement,” *Adv. Appl. Ceram.*, vol. 116, no. 3, pp. 123–131, Apr. 2017, doi: 10.1080/17436753.2016.1264122.

[113] J.-M. Costantini, G. Lelong, M. Guillaumet, W. J. Weber, S. Takaki, and K. Yasuda, “Color-center production and recovery in electron-irradiated magnesium aluminate spinel and ceria,” *J. Phys. Condens. Matter*, vol. 28, no. 32, p. 325901, Aug. 2016, doi: 10.1088/0953-8984/28/32/325901.

[114] R. J. M. Konings, K. Bakker, J. G. Boshoven, R. Conrad, and H. Hein, “The influence of neutron irradiation on the microstructure of Al2O3, MgAl2O4, Y3Al5O12 and CeO2,” *J. Nucl. Mater.*, vol. 254, no. 2–3, pp. 135–142, Apr. 1998, doi: 10.1016/S0022-3115(97)00355-3.

[115] S. Takaki, K. Yasuda, T. Yamamoto, S. Matsumura, and N. Ishikawa, “Atomic structure of ion tracks in Ceria,” *Nucl. Instrum. Methods Phys. Res. Sect. B Beam Interact. Mater. At.*, vol. 326, pp. 140–144, May 2014, doi: 10.1016/j.nimb.2013.10.077.

[116] W. J. Weber, “Alpha-irradiation damage in CeO_2, UO_2 and PuO_2,” *Radiat. Eff.*, vol. 83, no. 1–2, pp. 145–156, Jan. 1984, doi: 10.1080/00337578408215798.

[117] C. L. Tracy *et al.*, “Redox response of actinide materials to highly ionizing radiation,” *Nat. Commun.*, vol. 6, no. 1, p. 6133, May 2015, doi: 10.1038/ncomms7133.

[118] D. Gosset, M. Dollé, D. Simeone, G. Baldinozzi, and L. Thomé, “Structural evolution of zirconium carbide under ion irradiation,” *J. Nucl. Mater.*, vol. 373, no. 1–3, pp. 123–129, Feb. 2008, doi: 10.1016/j.jnucmat.2007.05.034.

[119] S. Pellegrino, L. Thomé, A. Debelle, S. Miro, and P. Trocellier, “Damage production in carbide single crystals irradiated with MeV heavy ions,” *Nucl. Instrum. Methods Phys. Res. Sect. B Beam Interact. Mater. At.*, vol. 307, pp. 294–298, July 2013, doi: 10.1016/j.nimb.2012.11.091.

[120] W. S. Williams, “Transition-metal carbides,” *Prog. Solid State Chem.*, vol. 6, pp. 57–118, Jan. 1971, doi: 10.1016/0079-6786(71)90028-8.

[121] H. Nakamatsu, T. Mukoyama, and H. Adachi, “Ionic and covalent bonds in CeO2 crystal,” *Chem. Phys. Lett.*, vol. 247, no. 1–2, pp. 168–172, Dec. 1995, doi: 10.1016/0009-2614(95)01185-7.

[122] A. Feinle, M. S. Elsaesser, and N. Hüsing, “Sol–gel synthesis of monolithic materials with hierarchical porosity,” *Chem. Soc. Rev.*, vol. 45, no. 12, pp. 3377–3399, 2016, doi: 10.1039/C5CS00710K.

[123] D. Z. Chaney *et al.*, “Grain size dependence of thermally induced oxidation in zirconium carbide,” *J. Mater. Sci.*, vol. 58, no. 6, pp. 2439–2455, Feb. 2023, doi: 10.1007/s10853-023-08145-8.

[124] W. Wesch, J. Rensberg, T. Bierschenk, B. Afra, P. Kluth, and E. Wendler, “Determination of track radii and relation to the electronic energy density deposited in swift heavy ion irradiated LiNbO3,” *Nucl. Instrum. Methods Phys. Res. Sect. B Beam Interact. Mater. At.*, vol. 485, pp. 50–56, Dec. 2020, doi: 10.1016/j.nimb.2020.10.015.

[125] K. Yasuda, J.-M. Costantini, and G. Baldinozzi, “Radiation-Induced Effects on Material Properties of Ceramics: Mechanical and Dimensional Properties,” in *Comprehensive Nuclear Materials*, Elsevier, 2020, pp. 153–185. doi: 10.1016/B978-0-12-803581-8.12052-1.

[126] L. Van Brutzel and J. P. Crocombette, “Classical molecular dynamics study of primary damage created by collision cascade in a ZrC matrix,” *Nucl. Instrum. Methods Phys. Res. Sect. B Beam Interact. Mater. At.*, vol. 255, no. 1, pp. 141–145, Feb. 2007, doi: 10.1016/j.nimb.2006.11.048.

[127] L. L. Snead, Y. Katoh, and S. Kondo, “Effects of fast neutron irradiation on zirconium carbide,” *J. Nucl. Mater.*, vol. 399, no. 2–3, pp. 200–207, Apr. 2010, doi: 10.1016/j.jnucmat.2010.01.020.

[128] S. Agarwal *et al.*, “Neutron irradiation-induced microstructure damage in ultra-high temperature ceramic TiC,” *Acta Mater.*, vol. 186, pp. 1–10, Mar. 2020, doi: 10.1016/j.actamat.2019.12.022.

[129] R. J. Price, “Neutron irradiation-induced voids in β-silicon carbide,” *J. Nucl. Mater.*, vol. 48, no. 1, pp. 47–57, Aug. 1973, doi: 10.1016/0022-3115(73)90077-9.

[130] K. G. Field, S. A. Briggs, K. Sridharan, Y. Yamamoto, and R. H. Howard, "Dislocation loop formation in model FeCrAl alloys after neutron irradiation below 1 dpa," *J. Nucl. Mater.*, vol. 495, pp. 20–26, Nov. 2017, doi: 10.1016/j.jnucmat.2017.07.061.

[131] W. G. Johnston, T. Lauritzen, J. H. Rosolowski, and A. M. Turkalo, "Void Swelling in Fast Reactor Materials — A Metallurgical Problem," *JOM*, vol. 28, no. 6, pp. 19–24, June 1976, doi: 10.1007/BF03354287.

[132] D. Hauser *et al.*, "The pervasive presence of oxygen in ZrC," *Surf. Interfaces*, vol. 34, p. 102373, Nov. 2022, doi: 10.1016/j.surfin.2022.102373.

[133] S. K. Sarkar, A. D. Miller, and J. I. Mueller, "Solubility of Oxygen in ZrC," *J. Am. Ceram. Soc.*, vol. 55, no. 12, pp. 628–630, Dec. 1972, doi: 10.1111/j.1151-2916.1972.tb13457.x.

[134] Y. Zhang, B. Liu, and J. Wang, "Self-assembly of Carbon Vacancies in Sub-stoichiometric ZrC1−x," *Sci. Rep.*, vol. 5, no. 1, p. 18098, Nov. 2016, doi: 10.1038/srep18098.

[135] K. Trachenko, M. Pruneda, E. Artacho, and M. T. Dove, "Radiation damage effects in the perovskite Ca Ti O 3 and resistance of materials to amorphization," *Phys. Rev. B*, vol. 70, no. 13, p. 134112, Oct. 2004, doi: 10.1103/PhysRevB.70.134112.

[136] C. L. Tracy *et al.*, "Role of composition, bond covalency, and short-range order in the disordering of stannate pyrochlores by swift heavy ion irradiation," *Phys. Rev. B*, vol. 94, no. 6, p. 064102, Aug. 2016, doi: 10.1103/PhysRevB.94.064102.

[137] K. Trachenko, J. M. Pruneda, E. Artacho, and M. T. Dove, "How the nature of the chemical bond governs resistance to amorphization by radiation damage," *Phys. Rev. B*, vol. 71, no. 18, p. 184104, May 2005, doi: 10.1103/PhysRevB.71.184104.

[138] G. W. Groves and A. Kelly, "Independent slip systems in crystals," *Philos. Mag.*, vol. 8, no. 89, pp. 877–887, May 1963, doi: 10.1080/14786436308213843.

[139] R. A. Rymzhanov, N. Medvedev, J. H. O'Connell, A. Janse Van Vuuren, V. A. Skuratov, and A. E. Volkov, "Recrystallization as the governing mechanism of ion track formation," *Sci. Rep.*, vol. 9, no. 1, p. 3837, Mar. 2019, doi: 10.1038/s41598-019-40239-9.

[140] R. Florez *et al.*, "The irradiation response of ZrC ceramics under 10 MeV Au3+ ion irradiation at 800 °C," *J. Eur. Ceram. Soc.*, vol. 40, no. 5, pp. 1791–1800, May 2020, doi: 10.1016/j.jeurceramsoc.2020.01.025.

[141] M. Gendre, A. Maître, and G. Trolliard, "Synthesis of zirconium oxycarbide (ZrCxOy) powders: Influence of stoichiometry on densification kinetics during spark plasma sintering and on mechanical properties," *J. Eur. Ceram. Soc.*, vol. 31, no. 13, pp. 2377–2385, Nov. 2011, doi: 10.1016/j.jeurceramsoc.2011.05.037.

[142] J. A. Leary, R. L. Thomas, A. E. Ogard, and G. C. Wonn, "Thermal conductivity and electrical resistivity of UC, (U, Pu)C, and PuC," OSTI Technical Report OSTI #4143001, Oct. 1963.

[143] J. Tiwari and T. Feng, "Intrinsic thermal conductivity of ZrC from low to ultrahigh temperatures: A critical revisit," *Phys. Rev. Mater.*, vol. 7, no. 6, p. 065001, June 2023, doi: 10.1103/PhysRevMaterials.7.065001.

[144] L. N. Grossman, "High-Temperature Thermophysical Properties of Zirconium Carbide," *J. Am. Ceram. Soc.*, vol. 48, no. 5, pp. 236–242, May 1965, doi: 10.1111/j.1151-2916.1965.tb14728.x.

[145] Roland M. Frye, Jr., "The Current 'Nuclear Renaissance' in the United States, its underlying reasons, and its potential pitfalls," *Energy Law J.*, vol. 29, no. 2, 2008.

[146] Jon Carmack, Frank Goldner, Shannon M. Bragg-Sitton, and Lance L. Snead, "Overview of the U.S. DOE accident tolerant fuel development program," presented at the Top Fuel 2013, Charlotte, NC, US, 2013.

[147] R. Li, B. Liu, and K. Verfondern, "The study of irradiation-induced failure behavior for the TRISO-coated fuel particle in HTGR," *J. Nucl. Mater.*, vol. 516, pp. 214–227, Apr. 2019, doi: 10.1016/j.jnucmat.2019.01.029.

[148] J. T. Maki, D. A. Petti, D. L. Knudson, and G. K. Miller, "The challenges associated with high burnup, high temperature and accelerated irradiation for TRISO-coated particle fuel," *J. Nucl. Mater.*, vol. 371, no. 1–3, pp. 270–280, Sept. 2007, doi: 10.1016/j.jnucmat.2007.05.019.

[149] D. A. Petti, J. Buongiorno, J. T. Maki, R. R. Hobbins, and G. K. Miller, "Key differences in the fabrication, irradiation and high temperature accident testing of US and German TRISO-coated particle fuel, and their implications on fuel performance," *Nucl. Eng. Des.*, vol. 222, no. 2–3, pp. 281–297, June 2003, doi: 10.1016/S0029-5493(03)00033-5.

[150] W. J. Weber, D. M. Duffy, L. Thomé, and Y. Zhang, "The role of electronic energy loss in ion beam modification of materials," *Curr. Opin. Solid State Mater. Sci.*, vol. 19, no. 1, pp. 1–11, Feb. 2015, doi: 10.1016/j.cossms.2014.09.003.

[151] Oak Ridge National Laboratory (ORNL), A. Terricabras, and S. Zinkle, "Radiation Effects on High Thermal Conductivity Fuels (Final Scientific Report)," 15–8752, 1504155, 15–8752, Mar. 2019. doi: 10.2172/1504155.

[152] B. L. Eyre and M. J. Sole, "On the formation and behaviour of point defect clusters in neutron irradiated uranium carbide," *J. Nucl. Mater.*, vol. 18, no. 3, pp. 314–322, Mar. 1966, doi: 10.1016/0022-3115(66)90172-3.

[153] L. He *et al.*, “Phase and defect evolution in uranium-nitrogen-oxygen system under irradiation,” *Acta Mater.*, vol. 208, p. 116778, Apr. 2021, doi: 10.1016/j.actamat.2021.116778.

[154] A. W. Hare, S. Alfant, F. A. Rough, and D. I. Sinizer, “Further Results of Irradiation of Uranium Carbide,” *Nucl. Sci. Eng.*, vol. 10, no. 1, pp. 24–30, May 1961, doi: 10.13182/NSE61-A25925.

[155] H. Matsui, M. Horiki, and T. Kirihara, “Irradiation of Uranium Carbides in JMTR,” *J. Nucl. Sci. Technol.*, vol. 18, no. 12, pp. 922–929, Dec. 1981, doi: 10.1080/18811248.1981.9733343.

[156] Raul Palomares, “Probing Point Defects in FLuorite-Structured Actinide and Analogue Oxides,” Ph.D. Dissertation, University of Tennessee, Knoxville, Tennessee, USApa, 2018.

[157] C. L. Tracy *et al.*, “Redox response of actinide materials to highly ionizing radiation,” *Nat. Commun.*, vol. 6, no. 1, p. 6133, Jan. 2015, doi: 10.1038/ncomms7133.

[158] E. Lopez-Honorato *et al.*, “Raman spectroscopy of uranium nitride kernels,” *J. Nucl. Mater.*, vol. 595, p. 155050, July 2024, doi: 10.1016/j.jnucmat.2024.155050.

[159] A. C. Ferrari, “Raman spectroscopy of graphene and graphite: Disorder, electron–phonon coupling, doping and nonadiabatic effects,” *Solid State Commun.*, vol. 143, no. 1–2, pp. 47–57, July 2007, doi: 10.1016/j.ssc.2007.03.052.

[160] K. Rickert, T. A. Prusnick, M. M. Kimani, E. A. Moore, C. A. Merriman, and J. M. Mann, “Assessing UO2 sample quality with μ-Raman spectroscopy,” *J. Nucl. Mater.*, vol. 514, pp. 1–11, Feb. 2019, doi: 10.1016/j.jnucmat.2018.11.009.

[161] E. Lopez-Honorato *et al.*, “Raman spectroscopy of uranium nitride kernels,” *J. Nucl. Mater.*, vol. 595, p. 155050, July 2024, doi: 10.1016/j.jnucmat.2024.155050.

[162] J. M. Elorrieta, L. J. Bonales, N. Rodríguez-Villagra, V. G. Baonza, and J. Cobos, "A detailed Raman and X-ray study of UO_{2+x} oxides and related structure transitions," *Phys. Chem. Chem. Phys.*, vol. 18, no. 40, pp. 28209–28216, 2016, doi: 10.1039/C6CP03800J.

[163] M. Watanabe and M. Kato, "Oxygen potential, oxygen diffusion, and defect equilibria in UO2±x," *Front. Nucl. Eng.*, vol. 1, p. 1082324, Jan. 2023, doi: 10.3389/fnuen.2022.1082324.

[164] M. Ugajin, "Measurements of O/U Ratio and Oxygen Potential for UO_{2+x} ($0 \leq x \lesssim 0.1$)," *J. Nucl. Sci. Technol.*, vol. 20, no. 3, pp. 228–236, Mar. 1983, doi: 10.1080/18811248.1983.9733384.

[165] M. Iwasawa, Y. Chen, Y. Kaneta, T. Ohnuma, H.-Y. Geng, and M. Kinoshita, "First-Principles Calculation of Point Defects in Uranium Dioxide," *Mater. Trans.*, vol. 47, no. 11, pp. 2651–2657, 2006, doi: 10.2320/matertrans.47.2651.

VITA

Jacob Andrew Minnette was born on July 3rd, 1998, in Evansville Indiana. Following high school, JAM attended Purdue University, during this time JAM first engaged in undergraduate research work, stimulating his interest in continued graduate education. He completed his bachelor's degree in Nuclear Engineering (BSNE) in May of 2021. JAM chose to attend the University of Tennessee, Knoxville to pursue his masters (MSNE) and PhD in nuclear engineering with graduate advisor Maik K. Lang. Research work conducted in pursuit of his graduate education focused on materials science for fission power systems, specifically focused on coated particle fuel materials. Following graduation JAM plans to continue his work in the greater nuclear power industry. JAM acknowledges the support of his friends and family.